

Multi-parametric Magnetic Resonance Imaging of the Spinal Cord at 9.4T

By

Tung-Lin Wu

Dissertation

Submitted to the Faculty of the  
Graduate School of Vanderbilt University  
in partial fulfillment of the requirements  
for the degree of

DOCTOR OF PHILOSOPHY

in

Biomedical Engineering

December 15<sup>th</sup> 2018

Nashville, Tennessee

Approved:

John C. Gore, Ph.D.

Li Min Chen, M.D., Ph.D.

Adam W. Anderson, Ph.D.

Zhaohua Ding, Ph.D.

Mark D. Does, Ph.D.

## ACKNOWLEDGEMENTS

I would first like to thank my Ph.D. committee members Dr. Anderson, Dr. Chen, Dr. Ding and Dr. Does for your advices, directions, pushing me for the better and always being available whenever I needed help.

I would also like to thank my colleagues and friends whom I got to meet and work with at VUIIS. In particular, I need to thank Feng and Nancy for their continuous support and help from my very first day. I am very fortunate to be doing my graduate studies at such a collaborative and encouraging environment.

I also want to thank my family for their unconditional support not only during graduate school but throughout my entire life.

I want to conclude my acknowledgement page by thanking the most important person during my time in graduate school: my mentor, Dr. Gore. Thank you for being so patient, supportive, inspiring and pointing me to the right directions. Obviously, none of the research here would have been possible without you. Beyond the science, little things that you do such as making time to just talk and listen to me means a lot. Your sense of humor is also one of many aspects I look up to. I cannot ask for a better mentor, and I don't think words can do justice on how thankful I am.

# TABLE OF CONTENTS

	Page
<b>ACKNOWLEDGEMENTS .....</b>	<b>ii</b>
<b>LIST OF TABLES .....</b>	<b>v</b>
<b>LIST OF FIGURES .....</b>	<b>vi</b>
<b>Chapter 1: INTRODUCTION.....</b>	<b>1</b>
1.1. Basic principles of magnetic resonance imaging (MRI).....	2
1.2. Basic principles of functional MRI (fMRI).....	10
1.3. Quantitative imaging of the spinal cord.....	15
1.4. Specific aims .....	24
1.5. Appendix .....	25
1.6. References .....	31
<b>Chapter 2: VALIDATION OF SPINAL CORD FMRI WITH LFP AND SPIKE ACTIVITY IN NON-HUMAN PRIMATES .....</b>	<b>42</b>
2.1. Abstract .....	42
2.2. Introduction .....	42
2.3. Methods.....	44
2.4. Results .....	51
2.5. Discussion and conclusions.....	54
2.6. References .....	61
<b>Chapter 3: RESTING-STATE FUNCTIONAL CONNECTIVITY IN THE RAT CERVICAL SPINAL CORD AT 9.4T.....</b>	<b>65</b>
3.1. Abstract .....	65
3.2. Introduction .....	65
3.3. Methods.....	68
3.4. Results .....	73
3.5. Discussion and conclusions.....	80
3.6. References .....	90

<b>Chapter 4: LONGITUDINAL ASSESSMENT OF SPINAL CORD INJURY WITH MULTIPARAMETRIC QUANTITATIVE MRI.....</b>	<b>96</b>
4.1. Abstract .....	96
4.2. Introduction – DTI, qMT, FMRI.....	96
4.3. Methods .....	98
4.4. Results .....	104
4.5. Discussion and conclusions.....	112
4.6. References .....	118
<b>Chapter 5: SUMMARY, SIGNIFICANCES AND FUTURE STUDIES.....</b>	<b>123</b>
5.1. Summary and significances.....	123
5.2. Future studies .....	124
5.3. References .....	129

## LIST OF TABLES

Table	Page
1. Temporal signal-to-noise-ratio (tSNR) of the cervical spinal cord that covers the four segments (C4-C7) of interest across runs in the five rats in this study.....	72
2. Percent signal change of averaged time series in gray matter spinal cord horns with the application of RETROICOR in non-human primates. ....	82

## LIST OF FIGURES

Figure	Page
1. Spins in the presence of an external magnetic field. ....	3
2. Spin relaxations. ....	6
3. Relationship between k-space and image space. ....	8
4. Gradient-echo (GRE) pulse sequence diagram.....	9
5. Spin-echo (SE) pulse sequence diagram. ....	9
6. Echo-planar imaging (EPI) pulse sequence diagram.....	10
7. Gross anatomy of the spinal cord. ....	16
8. DTI in the spinal cord.....	19
9. Schematic representations of the MT effect. ....	20
10. Anatomical images of NHP brain and spinal cord. ....	23
11. Pulsed gradient spin-echo pulse sequence.....	27
12. Electrophysiological recording recording sites for the four SMs. ....	50
13. Stimulus-driven and resting-state fMRI in non-human primates at 9.4T. ....	52
14. Stimulus-driven LFP and spike activity responses.....	53
15. Responses to innocuous tactile stimulation of digits in the spinal cord. ....	54
16. Local dorsal to ventral correlation profile. ....	55
17. ROI selections for each individual monkey. ....	56
18. Comparison between resting-state fMRI and LFP connectivities. ....	58
19. LFP dorsal-dorsal coherence at various depths. ....	59
20. MTC weighted anatomical images in three different views.....	69
21. Anatomical, BOLD and tSNR maps across five slices.....	71
22. Horns of the cervical spinal cord, white matter and averaged time series.....	74
23. Examples of within-slice resting-state correlation maps in the cervical spinal cord across all five animals.....	74
24. Group analysis of functional connectivity between spinal cord gray matter horns and “control” white matter regions. ....	76
25. Reproducibility and agreement of within-slice horn-to-horn functional connectivity. ....	76
26. Group analysis of functional connectivity between spinal cord gray matter horns (left) across different spinal segments.....	77
27. Group analysis of functional connectivity between spinal cord gray matter horns (right) across different spinal segments.....	78

28. The same analyses performed in Figure 25 were repeated without the use of bandpass filtering (0.01-0.16Hz). .....	79
29. Power spectra and time series for (A) ventral and (B) dorsal gray matter regions in Figure 22 before (red) and after (blue) band-pass filtering. ....	79
30. Effects of RETROICOR on rsfMRI in the cervical spinal cord of anesthetized and mechanically ventilated non-human primates. ....	81
31. Group analysis of functional connectivity between spinal cord gray matter horns and “control” white matter regions with white matter signal regression. ....	85
32. Manual ROI selections (red) of gray matter spinal cord horns across the five rats. ....	89
33. T1 measurement of the rat spinal cord. ....	101
34. QMT acquisition and analysis for healthy lumbar spinal cord. ....	102
35. PSR and FA maps with MT curve post-SCI. ....	105
36. Longitudinal assessments of the injury. ....	105
37. Comparisons of PSR and other MRI parameters. ....	106
38. Behavioral assessments post-SCI. ....	107
39. LFB stains of the spinal cord at different time points post SCI. ....	107
40. MTC weighted anatomical images in three different views and axial functional BOLD images. ....	108
41. Horns of the lumbar spinal cord, and averaged time series. ....	109
42. Examples of within-slice resting-state correlation maps. ....	109
43. MTC weighted anatomical images and axial BOLD images after injury. ....	110
44. Group analysis of functional connectivity between spinal cord gray matter horns. ....	111
45. Matrix of nonparametric Mann-Whitney tests between each boxplot in Figure 44. ....	113
46. Averaged fALFF for the four horns of the high-pass filtered 0.01Hz raw spinal cord data. ....	115

## Chapter 1: INTRODUCTION

The goal of this dissertation is to use magnetic resonance imaging (MRI) to measure inter-regional correlations of MRI signals in a resting state within the spinal cords of animals, validate their neuronal anatomical bases, and characterize the changes in composition, structure and function of the cord that occur after injury. Novel metrics of functional connectivity within the cord have been derived from acquisitions of resting-state BOLD images, along with quantitative, multi-parametric imaging assessments of tissue composition, and used to monitor longitudinal changes after spinal cord injuries in well-established animal models.

To date, the functional organization of the spinal cord remains relatively underexplored despite its importance serving as a conduit for motor outputs from the brain, peripheral inputs to the brain and as a center for coordinating certain reflexes. The measurement of functional connectivity within the spine based on detecting resting-state fluctuations in MRI blood oxygenation-level dependent (BOLD) signals potentially provides a new tool for assessing spinal cord functional architecture, but only recently have such signals been reliably detected and reported in humans (Barry et al., 2014) and non-human primates (NHPs) (Chen et al., 2015). Little is known about whether the spinal cord is expected to demonstrate functional connectivity similar to the brain, nor where these signal variations originate, nor if they are detectable in rodents, which are more commonly used as models of injury.

The research in this thesis detects and evaluates these signals in primate and rodent models, and performs correlated studies to understand their basis and evaluate their significance. Moreover, in order to further demonstrate their functional relevance, an injury model is studied to examine how resting-state functional connectivity is related to the integrity of the spine. In parallel, this thesis examines what changes in tissue composition and microstructure are also modulated by such disruptions, and whether novel multi-parametric MRI methods can detect relevant changes in tissues at a molecular level. Thus, the aims of this dissertation are to validate connectivity measures and implement multi-parametric MRI techniques that permit monitoring of the spinal cord in animals in both normal and injury conditions at 9.4T.

## **1.1. Basic principles of magnetic resonance imaging (MRI)**

MRI, which makes use of the phenomena of nuclear magnetic resonance (NMR), has played a vital role in the medical field for the past several decades. Its roots stem back to more than half a century ago when the first reports of NMR in condensed matter originated from independent researchers Felix Bloch (Bloch, 1953) and Edward Purcell (Purcell et al., 1946). Thirty years later, Paul Lauterbur won the Nobel Prize for making use of linear magnetic gradients and generating the first MR image (Lauterbur, 1973). However, it was only until the 1980s when MR scanners began to translate into medical centers from academia. Since then, MRI has been commonly used for not only radiological diagnosis, but also for comprehending various biological processes non-invasively in the human body. In this chapter section, the basics of MRI from the fundamental physics to the formation of an image are summarized.

### **1.1.1. MRI physics: spins, relaxation and the Bloch equations**

As described in many physics and MRI textbooks (Huettel; Song; McCarthy, 2004; Levitt, 2000; Nishimura, 2010), atoms with odd numbers of protons and/or neutrons are capable of producing NMR signals and are labelled as spins. Given the abundance of the water molecules in the human body (Altman and Dittmer, 1973), protons have become the primary nucleus of interest associated with MRI and will be the molecule of interest for later discussions throughout this thesis. Similar to a charged spinning sphere, these nuclear spins possess two key intrinsic properties: angular momentum and magnetic moment. Conceptually, angular momentum arises from the rotating mass while magnetic moment is the magnetic field generated from the nucleus.

Without the presence of an external magnetic field ( $B_0$ ) these spins are orientated randomly where magnetic moments of individual spins cancel out; simply put, there is no net magnetic effect. In the presence of an external magnetic field, however, these spins begin to precess at a characteristic frequency, known as the Larmor frequency ( $\omega$ ), about an axis parallel to  $B_0$ . The Larmor frequency, an important feature of spins exploited for MRI, is nucleus and field strength dependent and is governed by the equation:

$$\omega = \gamma B_0 \quad (1)$$

where  $\gamma$  is the gyromagnetic ratio constant and is a function of nuclear charge and mass;  $\gamma$  is approximately 42.58 MHz/T for protons. These precessing protons are further organized into two discretized energy states, given their quantum properties, with magnetic moments either pointing parallel or anti-parallel with  $B_0$  (also sometimes referred to as ‘spin-up’ and ‘spin-down’ respectively). Protons in a parallel state possess lower energy than those anti-parallel. Thus at equilibrium, there is a higher proportion of spins that populate the parallel state. The population difference between the two energy states thus results in the formation of a net magnetization parallel to  $B_0$ . Note, net magnetization ( $M_0$ ) of an ensemble of spins in the transverse plane cancels out due to random phasing of the individual spins at equilibrium (Figure 1).

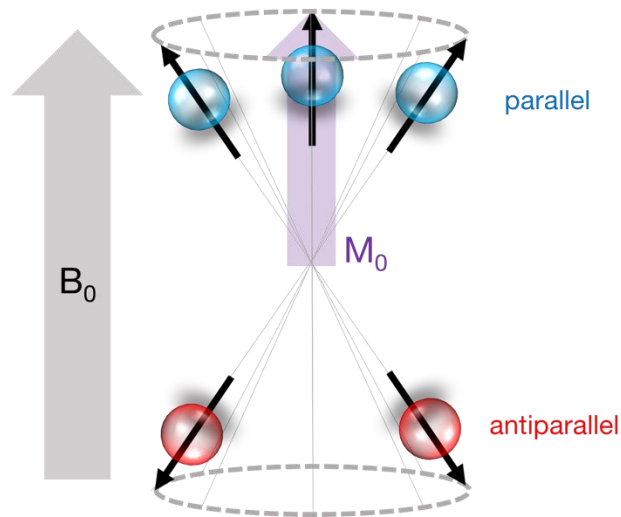


**Figure 1: Spins in the presence of an external magnetic field.** Magnetic moments (black solid arrows) of rotating spins align either parallel (blue protons) or anti-parallel (red protons) to the external magnetic field ( $B_0$ ). Because protons that possess less energy in the parallel state and are more stable, a higher proportion of spins are in the parallel state which results forms a the net magnetization,  $M_0$  parallel to  $B_0$ .

$M_0$  represents NMR signal that is available for detection which can be increased through changes in the system such as decreasing temperature or increasing field strength. The dynamics of the magnetic moment under  $B_0$  influence can also be elegantly described using:

$$\frac{d\boldsymbol{\mu}}{dt} = \gamma(\boldsymbol{\mu} \times \mathbf{B}_0) \quad (2)$$

Derivation of Equation 2 stems from the torque equation (full derivation in Section 1.5.1, Appendix A) and serves as the basis for the Bloch Equations (Bloch, 1953).

With protons precessing continuously about  $B_0$  (i.e.  $M_0$  situated in the longitudinal axis), NMR signals cannot be measured. Instead, a perturbation to the system must occur in order to detect and measure the precession of the net magnetization. Typically, an electromagnetic excitation or radiofrequency (RF) pulse is input into the system which causes torque to be exerted on the spin system. It is important to note that this excitation pulse is applied at the Larmor frequency in order for the net magnetization to be perturbed in the presence of the relatively large  $B_0$  field. As the RF pulse is applied into the spin system, the net magnetization is spirally tipped at the Larmor frequency towards the x-y plane. For a rectangular RF pulse, the flip angle ( $\theta$ ) through which the net magnetization is ‘tipped’ is proportional to the applied RF field ( $B_1$ ) and duration of the pulse (T):

$$\theta = \gamma B_1 T \quad (3)$$

With the net magnetization situated on the transverse plane, a receiver coil can then be placed to capture the continuous precession of the net magnetization as it sweeps across it. According to Faraday’s law, the receiver is capable of detecting the change in flux, which in turn creates an electromotive force for MR signal generation.

After the excitation pulse is removed, the net magnetization continues to precess and eventually returns to equilibrium or the longitudinal axis usually within seconds (Bloch, 1951; Goldman, 2001). This decay of signals is determined by two time constants and relaxation processes: spin-lattice (longitudinal) relaxation and spin-spin (transverse) relaxation. Longitudinal relaxation ( $T_1$ ) occurs when the spins return from the anti-parallel state to the lower energy parallel state system by losing energy to the environment or the spin lattice. As the number of spins populate back to the lower energy state, the net magnetization also concurrently returns to the longitudinal direction parallel to the  $B_0$  field before excitation:

$$\frac{dM_z}{dt} = -\frac{M_z - M_0}{T_1} \quad (4)$$

$$M_z(t) = M_0 + [M_z(0) - M_0] e^{-t/T_1} \quad (5)$$

Transverse relaxation occurs through both intrinsic ( $T_2$ ) and extrinsic ( $T_2'$ ) mechanisms. The intrinsic mechanism involves the loss of coherence between spins due to their interactions and effects on each other; hence the name, spin-spin relaxation. As more spins become out of synchronization, or out of phase, with each other, this causes a loss of net magnetization in the x-y plane that is irreversible. In the rotating frame of reference, this is described mathematically using:

$$\frac{dM_{x,y}}{dt} = -\frac{M_{x,y}}{T_2} \quad (6)$$

$$M_{x,y} = M_{x,y}(0)e^{-t/T_2} \quad (7)$$

Another source of transverse relaxation may arise from extrinsic factors such as spatial variations in the  $B_0$  field. Interestingly, this external perturbation is exploited and serves as the basis of fMRI. The combined effects of intrinsic and extrinsic mechanisms on the transverse magnetization is referred to as  $T_2^*$ , and is thus always shorter than  $T_2$ :

$$\frac{1}{T_2^*} = \frac{1}{T_2} + \frac{1}{T_2'} \quad (8)$$

With relaxation and excitation mechanisms added into our picture of spin systems, Equation 2 that describes dynamics of the net magnetization can thus be updated:

$$\frac{d\mathbf{M}}{dt} = \gamma\mathbf{M} \times \mathbf{B} + \frac{1}{T_1}(\mathbf{M}_0 - \mathbf{M}_z) - \frac{1}{T_2}(\mathbf{M}_x + \mathbf{M}_y) \quad (9)$$

with  $\mathbf{B}$  describing the magnetic field encountered by the nuclei.

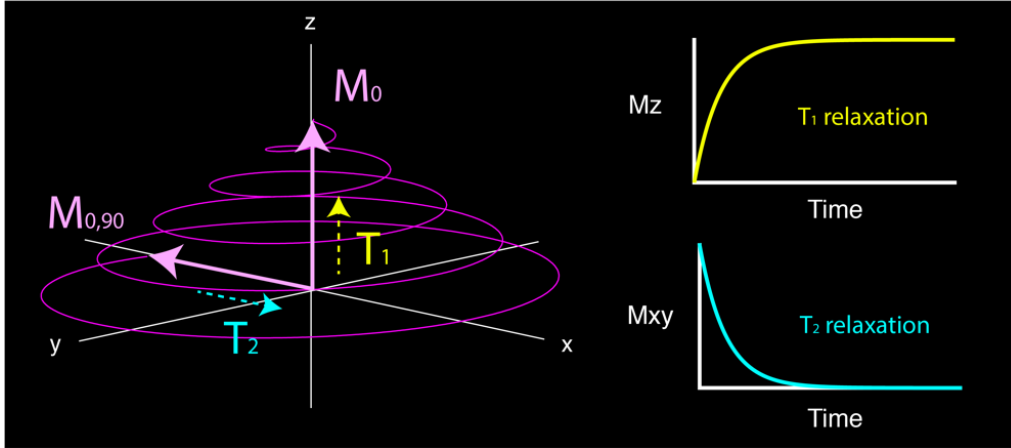


**Figure 2: Spin relaxations.** Longitudinal ( $T_1$ , yellow) and transverse relaxations ( $T_2$ , blue) of the spin net magnetization ( $M_0$ , pink) after a 90-degree excitation pulse ( $M_{0,90}$ , pink).  $T_2$  decay, spin-spin relaxation, is characterized by the equation  $M_{x,y}(t) = M_0 e^{-t/T_2}$  while  $T_1$  recovery, spin-lattice relaxation, follows  $M_z(t) = M_0(1 - e^{-t/T_1})$ . Dark pink lines represent the trajectory which  $M_{0,90}$  recovers back to the initial  $M_0$ , which is aligned with  $B_0$ .

### 1.1.2. Image formation and acquisition

While the understanding of NMR physics allows signals from spins to be detected, the introduction of magnetic gradients by Lauterbur opened the door to image formation by MRI (Lauterbur, 1973). Specifically, the use of magnetic gradients causes spins at different locations to experience different magnetic fields and thus precess at various frequencies. By measuring the magnetization as a function of different frequencies, the spatial distribution of spins can subsequently be teased out to create an image.

As described in (Bernstein et al., 2004; Huettel; Song; McCarthy, 2004; Levitt, 2000; Nishimura, 2010), gradients in three directions are played out in order for a 3D image to be reconstructed. The direction of  $B_0$  is commonly denoted as the z-direction. One way to image a 3D volume conventionally involves the stacking of multiple 2D images or slices. Thus, the first step involves the application of a linear gradient in the z-direction, commonly known as the slice selection gradient. As a result, spins precess at different frequencies along different positions along the z-axis. An excitation RF pulse will also be applied simultaneously to match the frequency bands of interest to tip only the spins precessing in the specific bands. Overall, there are two factors that determine the thickness and location of the slice select: 1) center frequency and frequency bandwidth of the excitation pulse and 2) strength of the z-gradient. After exciting spins in a

particular slice, the MR signal equation can be simplified and is specified in Equation 10, where spatial information is indicated as  $x$  and  $y$  while  $t$  indicates time:

$$S(t) = \int_x \int_y M(x, y) e^{-i\gamma \int_0^t (G_x(\tau)x + G_y(\tau)y) d\tau} dx dy \quad (10)$$

After exciting spins that are precessing at a specific frequency band, dimensionality of creating a 3D image reduces to 2D problem. Specifically, this involves 2D spatial encoding where a preset sequential encoding gradient is applied (commonly known as the y-gradient) followed by a frequency encoding gradient that is turned on during readout. This allows adequate sampling of k-space, a formalism describing MRI acquisition, which can be described mathematically in terms of x- and y- gradients as:

$$k_x(t) = \frac{\gamma}{2\pi} \int_0^t G_x(\tau) d\tau \quad (11)$$

$$k_y(t) = \frac{\gamma}{2\pi} \int_0^t G_y(\tau) d\tau \quad (12)$$

The signal equation can thus be described in terms of  $k_x$  and  $k_y$ ,

$$S(t) = \int_x \int_y M(x, y) e^{-i2\pi k_x(t)x} e^{-i2\pi k_y(t)y} dx dy \quad (13)$$

Importantly, this equation conveys that k-space and image space are 2D Fourier transforms of each other. In other words, with sampling of k-space completed, a 2D inverse Fourier transform can be performed to convert k-space data to an image. Because the basic unit of k-space data is spatial frequency while image space is in distance, several relationships exist between the two spaces in terms of field of view (FOV) and spatial resolution of MR images as shown in Figure 3.

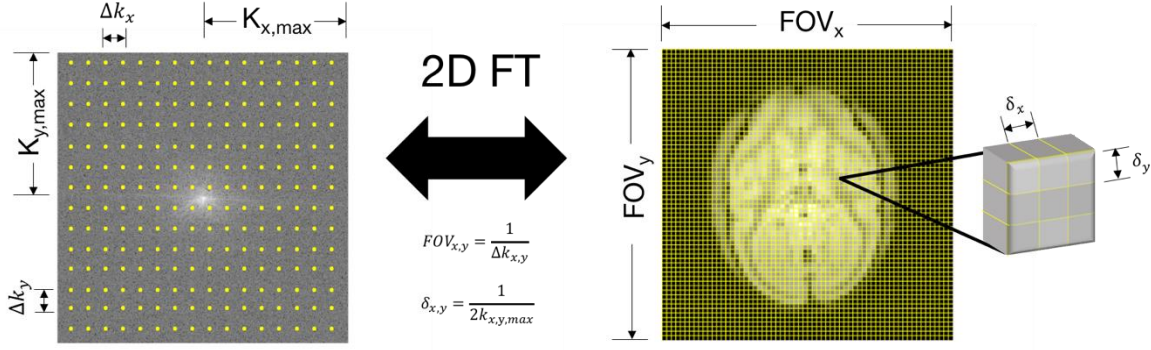


**Figure 3: Relationship between k-space and image space.** Anatomical NHP brain image acquired at 9.4T (right) and its respective k-space (left). Field of view (FOV) of the brain in the x and y directions are equal to the k-space sampling rates ( $\Delta k$ ) in the x and y directions respectively. On the other hand, resolutions of the anatomical image ( $\delta$ ) are related to the extent of k-space sampling ( $K_{max}$ ). Elegantly, the two domains are related by 2D Fourier transforms of each other.

### 1.1.3. Pulse sequences

Using the concepts of image formation previously described, a pulse sequence describes how a series of excitation pulses and magnetic gradients are played out across time for k-space to be sampled. MRI is attractive not only for its non-invasive and non-radiative nature, but also for the intrinsic contrast that can be exploited to describe properties of the medium of interest. Contrast is mainly governed by the pulse sequences applied and the specific parameters associated with them, such as repetition time (TR) and echo time (TE). For a common sequence in which 90-degree RF pulses are applied at regular interval TR and data are acquired with delay TE, the measurable transverse magnetization is:

$$M_{xy}(t) = M_0 \left( 1 - e^{-\frac{TR}{T_1}} \right) e^{-TE/T_2} \quad (14)$$

One of the most commonly used pulse sequence is the gradient-echo (GRE) pulse sequence as shown in Figure 4. The GRE is played out by first dephasing spins with a readout gradient and subsequently rephasing them with a readout gradient sequence in the opposite polarity. In other words, peak signal occurs when the area of the two gradients (prephasing and rephasing gradients) are equal, also denoted as TE. The k-space trajectory of GRE is also Cartesian where k-space is

acquired line-by-line. Fast-GRE sequence has also been used for fMRI studies where it can be optimized for fast imaging using a small TR and flip angle.

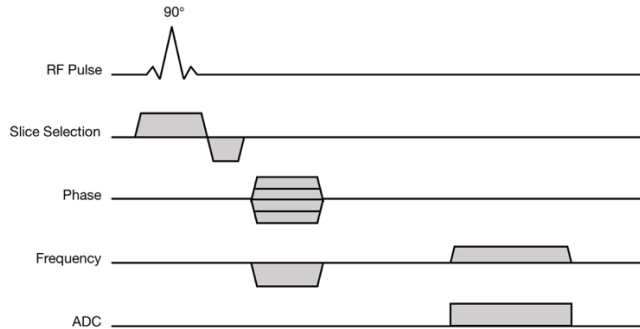


**Figure 4: Gradient-echo (GRE) pulse sequence diagram.** An initial 90-degree excitation pulse is followed by prephasing and rephasing gradients. In the absence of a 180-degree refocusing pulse, GRE does not correct for  $B_0$  inhomogeneity and is thus more sensitive to  $T_2^*$  decay. Instead, rephasing of the spins occurs by applying a reversed frequency gradient.

Another commonly used pulse sequence is the spin-echo (SE) pulse sequence (Hahn, 1950). It consists of a 90-degree excitation followed by a 180-degree refocusing pulse, producing images with  $T_2$  contrast without the effects of static field inhomogeneities. The SE sequence is advantageous over the GRE sequence as it mitigates artifacts that arise from magnetic susceptibility and field inhomogeneities.

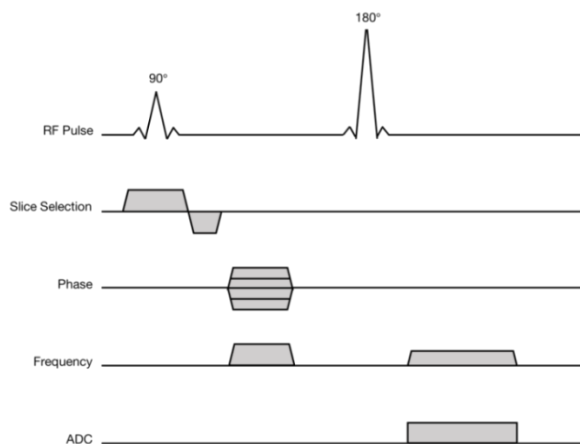


**Figure 5: Spin-echo (SE) pulse sequence diagram.** An initial 90-degree excitation pulse is followed by a refocusing pulse commonly at a flip angle of 180 degrees, which allows the transverse magnetization to be refocused. As described, the SE pulse sequence is more immune to field inhomogeneities and susceptibility effects than GRE sequences.

Lastly, another commonly used pulse sequence, especially for fast-imaging, is the echo-planar imaging (EPI) sequence. This sequence developed by Mansfield et al. involves the use of bipolar readout gradients that create an echo train (Mansfield, 1977). Phase encoding gradients or ‘blips’ are also applied along with the readout gradients that allow a complete range of k-space to be collected from a single RF excitation. The EPI sequence has greatly opened up many MR applications that require images to be formed at an ultra-fast speed such as functional, diffusion and cardiac imaging.

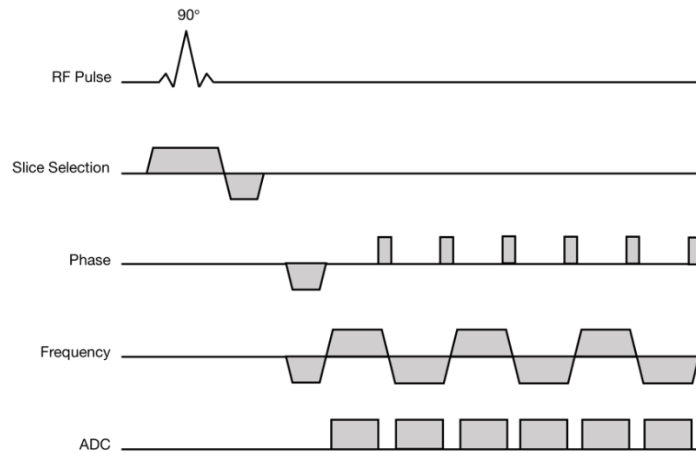


**Figure 6: Echo-planar imaging (EPI) pulse sequence diagram.** Sampling of k-space in an EPI sequence involves a series of bipolar readout gradients along with ‘blips’ in the phase encode direction. This creates a train of gradient echoes. EPI continues to be one of the fastest imaging sequences used today.

## 1.2. Basic principles of functional MRI (fMRI)

fMRI measures blood oxygenation level dependent (BOLD) effects and is a well-established non-invasive technique for identifying neural activation patterns in the brain. Indeed, the magnitude of BOLD hemodynamic effects has been directly related to the level of underlying electrical activity under both stimulus-evoked and resting-state conditions (Fox and Raichle, 2007; Logothetis et al., 2001). In this chapter section, basic principles of fMRI are introduced as well as its relationship with neuronal activity. Advantages of functional imaging at high field and pre-processing analysis steps are also outlined.

### **1.2.1. Blood oxygenation level-dependent contrast**

BOLD contrast serves as the fundamental basis of fMRI (Ogawa et al., 1992, 1990b; Ogawa and Lee, 1990). It is generally accepted that an increase in local neural activity stimulates an increase in blood flow in order to meet the metabolic and oxygen demands; this concept is commonly known as functional hyperemia. In fact, the supply of blood flow and oxygen to these regions exceeds the demands and oxygen consumption rate, and thus excess oxygenated blood supplied to the region flushes out deoxygenated blood (Fox et al., 1988; Fox and Raichle, 1986, 1984). The displacement of de-oxygenated blood with oxygenated blood is reflected with an increase of intensity in  $T_2^*$ - and  $T_2$ -weighted MR signals. This is because de-oxygenated hemoglobin has been found to be paramagnetic so its presence creates an inhomogeneous magnetic field which causes a faster decay of the signal (Pauling and Coryell, 1936). Moreover, a delay of seconds appears to exist between neuron activation and corresponding vasodilation necessary for increased blood flow (Robson et al., 1998). This temporal dynamic is captured in the hemodynamic response and reflected as increases in BOLD signal often several seconds after stimulus onset. A series of images acquired in an fMRI study is subsequently analyzed statistically to tease out small changes in MR signal associated with neuronal activity. Detailed information on the principles of fMRI is further summarized and can be found in (Gore, 2003).

### **1.2.2. High field fMRI**

For fMRI, high fields are highly desirable due to an increased sensitivity and specificity. It is generally accepted that signal-to-noise ratio (SNR) increases linearly with field strength; signal increases quadratically with field strength but thermal noise also increases linearly (Hoult et al., 1986). Conceptually, the energy gap between high and low energy states widens, which in turn causes more spins to align parallel to  $B_0$  producing a greater net magnetization. The increase in raw SNR at high fields can in turn be exploited to improve spatial and temporal resolutions.

On top of the increased SNR, fMRI at high field strength also increases BOLD specificity and contributions from smaller blood vessels. Specifically, it has been found that neuronal activities are more associated with microvasculature effects than large blood vessels, which are less uniformly distributed and can be away from the activation site (Lai et al., 1993; Menon et al., 1993). Microvasculature contributions have been found to be more dominant at high fields with a quadratic dependence instead of a linear relationship for larger vessels (Ugurbil et al., 2001). In

other words, signals from microvasculature are more dominant at high field.

The conventional use of a GRE sequence in fMRI captures both intravascular (spins within the vessel) and extravascular signal sources (spins in the surrounding tissue). On the other hand, SE sequences reduce extravascular signals that originate from large vessels while signals intravascular from both large and small vessels remain detectable. This is because diffusion distances around blood cells are large compared to the local magnet fields they generate. Fortunately, at high fields, the  $T_2$  of venous blood is very short and thus intravascular signals are attenuated making  $T_2$  based BOLD sensitive mainly to changes in the water of extravascular small vessels. Notably at 9.4 T, the field strength used in this thesis,  $T_2$  of blood water is approximately 5 ms (Lee et al., 1999) and thus pulse sequences with relatively long TE suppress intravascular contributions to the BOLD signals. In summary, neuronal activities are more coupled to microvasculature contributions primarily in the capillary beds than in larger vessels, which is accentuated at higher field strengths.

### **1.2.3. Resting-state functional connectivity**

Early fMRI experiments were largely designed to localize different functions in the brain through presentations of either block-designed or event-related stimuli to subjects. It was not until 1995 that Biswal et al introduced the study of resting-state functional connectivity by identifying synchronous spontaneous BOLD fluctuations between different regions of the brain (Bharat Biswal et al., 1995). In that study, resting-state functional connectivity were inferred by computing Pearson's correlations to a seed voxel placed in the left motor cortex. Interestingly, the resting-state correlation patterns demonstrated very similar patterns to when the subject performed bilateral finger tapping results including strong correlation patterns to the contralateral cortex. This pioneering work sparked subsequent investigations in the next two decades that have led to breakthroughs in detecting multiple resting-state networks (Biswal et al., 1997; Cordes et al., 2002; Fox and Raichle, 2007; Greicius et al., 2003; Lowe et al., 2000; van den Heuvel and Hulshoff Pol, 2010).

Low frequency resting-state fluctuations below 0.1 Hz have typically been the signal of interest and have greatly contributed to our understanding of networks at rest. Indeed, the resting-state technique provides a powerful approach to understanding and delineating neural circuits for assessing which neural systems work together to achieve specific functions. To date, the

underlying neuronal basis of these slow fluctuations in BOLD signals remains unclear. Several research groups have raised concerns that physiological processes such as cardiac and respiratory oscillations may be the primary effects of correlated resting signals, while others have also suggested that these co-activations of resting-state signals may actually reflect spontaneous neuronal activation. Due to the relatively low temporal resolution of fMRI of typically 2 to 3 seconds, high frequency physiological oscillations can alias back into the low frequency range of interest which would artificially drive correlations between separate regions of the brain (Birn et al., 2008; Chang et al., 2009; Van Buuren et al., 2009). On the other hand, proponents of the latter explanation have found that highly correlated regions overlap with neuroanatomy and function (Bharat Biswal et al., 1995; Damoiseaux et al., 2006; De Luca et al., 2005; Lowe et al., 2000). Moreover, power analyses have shown spontaneous BOLD fluctuations to occur predominantly below 0.1 Hz while physiological patterns display a different frequency pattern (Cordes et al., 2001, 2000). Electrophysiology studies that measure direct neural activity have also found strong correlations with resting-state BOLD signals (Nir et al., 2008a; Shi et al., 2017; Shmuel et al., 2002; Shmuel and Leopold, 2008). Nevertheless, growing evidences are suggesting resting-state fMRI reflects ongoing neural activity between brain regions which presents itself as an attractive biomarker for different pathological conditions (M. H. Lee et al., 2013).

#### **1.2.4. Pre-processing of resting-state fMRI data**

BOLD effects contribute only a small percentage of the variance in MRI signals. Indeed, non-neuronal factors contribute to their variability which include, for example, thermal noise, scanner drifts, motion artifacts, and physiological noises. The contribution of these factors to the signal depend on the instrumentation as well as neuronal physiological states of the subject in the magnet. In order to minimize these factors that mask the BOLD signal, raw fMRI data undergo a series of pre-processing steps. The pre-processing pipeline typically involves slice-timing correction, motion correction, physiological noise denoising, nuisance signal regression and temporal filtering. In the next paragraph, a brief explanation of each pre-processing step is presented.

One of the first steps to fMRI pre-processing involves slice-timing correction (Calhoun et al., 2000). This step temporally interpolates fMRI time series and corrects for differences to when each slice was acquired; within each TR, multiple slices are acquired in a specified order.

Subsequently, motion of the subject during acquisition, which is notorious for contributing to confounding factors that can significantly affect data quality (Haller and Bartsch, 2009; van Dijk et al., 2012), are corrected for. Motion during fMRI acquisition can lead to a wide range of issues such as data loss at the edges and mixing of signals from two types of tissues. Fortunately, physical restraints implemented can mitigate its effects along with retrospective motion correction algorithms (Friston et al., 1995; Jenkinson et al., 2002). A majority of the existing motion correction algorithms make use of rigid-body transformations that are described by six degrees of freedom – three rotations and three translations. Images from a time series are co-registered to a reference image by optimization of a specific cost function. Nuisance signals that characterize noise fluctuations are also extracted from reference region time series and included as regressors in the design matrix of a general linear model of the signal. Variances explained by these regions are then subtracted from the BOLD signal and this approach has been commonly applied for both resting-state and task-based fMRI studies. If respiratory and cardiac traces are recorded, physiological denoising is also performed, typically with an image-based retrospective correction technique (RETROICOR) (Glover et al., 2000). Lastly, temporal filtering is applied to extract specific bands of frequencies to reduce signal fluctuation contributions of noise from other frequency bands. Overall, optimized fMRI pre-processing pipelines may vary among different studies depending not only on the quality of the dataset but also on which specific regions are being imaged.

### **1.2.5. Validation of fMRI with electrophysiology**

fMRI is an indirect measure of underlying neural activity, and the validation of BOLD measures with invasive gold-standard measures is critical for accurate interpretations. As described in various textbooks (Fröhlich and Fröhlich, 2016; Huettel; Song; McCarthy, 2004; Standring, 2016), changes in membrane potentials reflect integrative neural activity, while action potentials or self-propagating depolarization waves represent the transmission of neural information. In order to capture these electrical properties and changes, an electrode can be placed next to a neuron. Depending on the size of the electrodes, action potentials can be captured either individually (single-unit activity) or from a collective group of neurons (multi-unit activity). Post-synaptic potentials are also recorded with these electrodes but they appear as low frequency signals (<300Hz) known as local field potentials (LFPs) (Katzner et al., 2009; Xing et al., 2009). In other

words, LFPs reflect voltages created by summing dendrite potentials (excitatory and inhibitory) from a population of neurons within a distance from the tip of the electrode (Huettel; Song; McCarthy, 2004). Furthermore, frequency compositions of the LFP activity that supposedly reflect different neural processing pathways have also been examined, and are of particular interest to the neuroscience community (Einevoll et al., 2013; Magri et al., 2012).

In examining the relationship of these electrical recordings with BOLD signals, studies have found coupling between fMRI with both LFPs and spiking activity. Notably, Logothetis et al. found from simultaneous electrophysiology and MRI recordings in NHPs that LFPs correspond most closely with fMRI signal changes (Logothetis et al., 2001). In our laboratory, point spread functions of BOLD and LFP were compared in the primary somatosensory cortex of NHPs responses and we found comparable intervoxel spatial correlation profiles between the two modalities (Shi et al., 2017). On the other hand, neuronal spiking has also been found to be associated with BOLD signals (Shmuel et al., 2002; Shmuel and Leopold, 2008). In summary, the relationship between BOLD signals and neural activity appears to be complex and warrants more examination, especially for BOLD signals in a resting state.

### **1.3. Quantitative imaging of the spinal cord**

The spinal cord plays an extremely important role in our nervous system. It is the major communication relay between our brain and the peripheral nervous system. On top of that, it is also capable of integrating incoming information and producing rapid responses through various reflex mechanisms. Despite serving as the backbone of these critical roles, the spinal cord remains relatively unexplored in the field of MRI when compared to its counterpart, the brain. This may be due to the spinal cord's small physical size and its relatively poor SNR when imaged at conventional field strengths. In this chapter section, neuroanatomy of the spinal cord is first outlined followed by an introduction of quantitative MR methods (DTI, qMT and fMRI) that have been applied to the spinal cord.

#### **1.3.1. Neuroanatomy of the spinal cord**

The spinal cord is an elongated bundle of nerve fibers enclosed in the vertebral column. Because it does not grow as fast as the vertebral column, it occupies only the superior two-thirds

of it. Within the vertebral column shell, the spinal cord is further surrounded and protected by connective tissue membranes which include the dura, arachnoid and pia maters (Standring, 2016). Extending from the rostral to caudal direction, the spinal cord gives rise to 31 spinal nerves and is classified into cervical (C), thoracic (T), lumbar (L) and sacral regions. Notably at the cervical and lumbar levels, a region of enlargement is present where large nerves supplying the upper limbs and pelvic/lower limbs are located respectively. Given the increased neuronal input and output at the enlargements, the intrinsic functional circuits in these regions have become a target of interest in literature and in this thesis as well.

By taking a cross sectional view of the spinal cord, a gray matter butterfly structure surrounded by white matter is revealed (Figure 7). Interestingly, this arrangement is opposite from that of the brain. Gray matter in the spinal cord contains mainly neuronal cell bodies and glia and serves as the site of synaptic integration. Laminae of the spinal cord have also been identified by Bror Rexed in the 1950s based on structure and function (Rexed, 1952), and are roughly divided into three distinct regions: dorsal horns, intermediate regions, and ventral horns. The dorsal horns receive afferent nerve fibers while ventral horns contain efferent fibers connected to skeletal muscles. An additional lateral horn containing neurons of the sympathetic system has also been reported in the thoracic and lumbar regions (Standring, 2016).

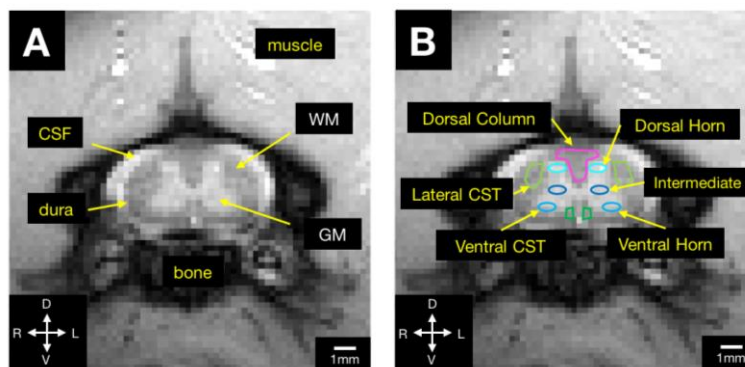


**Figure 7: Gross anatomy of the spinal cord.** Magnetization transfer contrast images of the NHP spinal cord overlaid with anatomical labels in the cross sectional view. (A) Spinal cord soft tissues – white matter (WM) and gray matter (GM) – are indicated with white while other components in the spinal cord’s vicinity are labeled with yellow. The GM butterfly is visible with reasonable contrast with WM. The cerebrospinal fluid (CSF) is observed as a band of high intensity signals adhered to the spinal cord while the vertebrae bone column space contributes to minimal MR signals. (B) Specific WM and GM microstructures labeled in the spinal cord. GM horns that make up the butterfly structure – dorsal horns, intermediate regions and ventral horns – are traced with different shades of blue. Ascending WM tracts of dorsal column are outlined in pink while lateral and ventral spinal corticospinal tracts (CST) are traced with light and dark green respectively.

Unlike gray matter, white matter in the spinal cord is primarily made up of myelinated axons that carry information up and down the cord. White matter in the spinal cord forms bundles that are arranged in columns (dorsal, lateral and ventral), which are further divided into tracts (ascending and descending). Ascending tracts carry sensory information up the spinal cord typically through three different types of neurons: first-order neurons that detect the initial stimulus and transmit it to the spinal cord, followed by second order neurons that relay the information to the thalamus, and lastly third order neurons that carry the signal to the appropriate cortex. Notable ascending tracts include the cuneate/gracile fasciculus and spinothalamic tracts which carry vibrational tactile and pain information respectively. In contrast, descending tracts conduct motor impulses down the cord where signals originate from the upper motor neuron in the cortex, and then travel either to the lower motor neurons in the brainstem or via the spinal cord that leaves through a spinal nerve to a muscle.

### **1.3.2. Functional importance of the spinal cord**

Spinal cord injuries cause devastating consequences for patients due to severe impairments of motor and/or sensory functions. Indeed, the spinal cord plays a critical role in conducting electrical signals between the brain and different parts of the body through ascending and descending tracts. Besides serving as an information highway, local spinal pathways have been known to produce involuntary responses, also commonly known as the reflex arcs, to specific stimuli. The majority of reflexes are mediated locally and involves a relatively simple pathway in the spinal cord. Located within the spinal cord, a more complex circuit that consists of a group of interneurons, called the complex pattern generator (CPG), has also been identified to be responsible for rhythmic locomotor movements (Brown, 1914; Dietz, 2003; Guertin, 2012; Marder and Bucher, 2001). The CPG has been found to produce self-sustained patterns of behaviors in the absence of peripheral inputs (Dietz, 2003; Grillner et al., 1995). Specifically, the interneurons that make up the CPG have been found to be located in L1/L2 segments of rodents (Hadi et al., 2000; Magnuson et al., 1999), the region we targeted for our spinal cord injury model in this thesis.

### **1.3.3. Animal models**

The majority of what we know about the CPG comes from animal studies. Early experiments from Brown demonstrated that cats with transected spinal cords and removed dorsal roots still demonstrated the ability to exhibit contractions in the ankle flexors and extensors (Brown, 1912, 1911). Such information cannot be obtained from human studies and highlights the importance of animal models. Animals can afford a range of experimental manipulations that are ethically not made possible in human subjects (Hutchison and Everling, 2012). In the spinal cord, valuable information can be obtained from spinal lesions induced in animals, and when imaged at high field, sub-millimeter spatial resolution allows not only for reliable monitoring but also quantification of the longitudinal recovery process (Chen et al., 2015; Wang et al., 2014). NHPs provide an excellent model thanks to their high degree of similarity with humans in terms of neural circuits and functional architecture (Hutchison and Everling, 2012). Thus, a crucial linkage between human and animal data can be made via studies of monkeys in this thesis. Although NHPs provide an excellent model for human studies, their usages can also be difficult at times compared to rodents due to limitations such as handling procedures, and costs. Moreover, rodents present less inter-subject variability and allow more reliable contusion lesions to be induced for longitudinal studies. Due to these reasons, a rodent model is also incorporated into this thesis for multi-parametric modelling of spinal cord injury recovery.

### **1.3.4. DTI in the spinal cord**

Diffusion tensor imaging (DTI) makes use of measurements of water motion in both the brain and spinal cord to infer structure. Similar to when a drop of ink enters a glass of water, diffusion describes the random free thermal motion of molecules governed by Einstein's equation (Einstein, 1905). In biological tissues, however, the presence of cell membranes, axonal tracts and myelin in the central nervous system act as physical barriers, which hinders diffusion and imposes directionality in anisotropic media. For example, water diffuses more easily along fibers due to fewer obstacles encountered than in the transverse direction (Figure 8). Magnetic field gradients can be applied to acquire MR images sensitive to the rate and direction of movements of water molecules (Stejskal and Tanner, 1965; Torrey, 1956). These diffusion sensitive images allow for the deduction of fiber organization and provide information about the microstructural composition of tissues (Horsfield and Jones, 2002). The most common approach to characterizing diffusion in

each voxel has been with a 3D ellipsoid (Basser et al., 1994) derived from the diffusion tensor which provides indices sensitive to pathological changes, such as fractional anisotropy (FA), mean (ADC), radial and axial diffusivities. Derivations of the ellipse model and the typical diffusion pulse sequence can be found in Appendix B in Section 1.5.2.

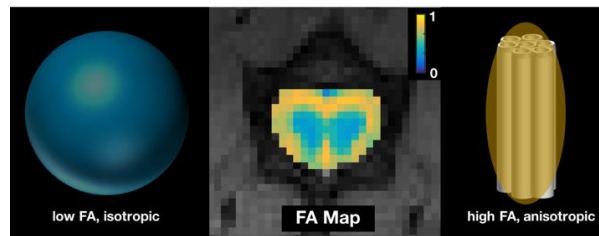


**Figure 8: DTI in the spinal cord.** FA map (center) of a transverse slice of the rat cervical spinal cord. High and low FA values are located in white (yellow) and gray (blue) matter respectively. Isotropic diffusion (left) represented as a sphere where diffusion is the same in all directions. Anisotropic diffusion (right) represented as an elongated ellipsoid to characterize diffusion is different in various directions. In the context of the spinal cord, diffusion is anisotropic and parallel to fibers running in the rostral-caudal direction in white matter.

DTI methods are well-established in the brain, and the same principles also apply to the spinal cord. Indeed, in both healthy animal and human spinal studies, DTI has been shown to reliably differentiate between highly anisotropic white matter and isotropic gray matter. Taking a step further, DTI measures have also been used as indicators for pathological conditions such as multiple sclerosis and various injury models in the spinal cord (Horsfield and Jones, 2002). While specific methods vary in terms of acquisition plane and quantification methods, results have shown that DTI metrics in the spinal cord are sensitive to changes that are not possible with conventional MRI. In this thesis, DTI is used as a quantitative MRI method to provide longitudinal tracking of white matter fibers in a spinal cord injury model.

### 1.3.5. QMT in the spinal cord

The basis of magnetization transfer (MT) contrast lies in the detection of protons that are associated with large macromolecules in tissues. Due to the fast  $T_2$  decay of macromolecular protons, conventional pulse sequences are unable to detect them directly. However, these macromolecular protons communicate through either dipole-dipole interactions or direct chemical

exchange with protons of bulk water (Henkelman et al., 2001). By exploiting the exchange between the two pools of protons, macromolecular protons can in fact be indirectly detected. Specifically, an RF irradiation is applied at an offset frequency to selectively saturate macromolecular protons. This saturation is subsequently transferred to the free water protons through the MT effect, resulting in attenuation of the MR signal. Figure 9 presents a two pool model used to characterize the pool-size ratio PSR in this thesis (see Appendix C, Section 1.5.3). Importantly, this MT effect has been shown to correlate and reflect white matter myelin density (Henkelman et al., 2001; Kucharczyk et al., 1994; Schmierer et al., 2004a).

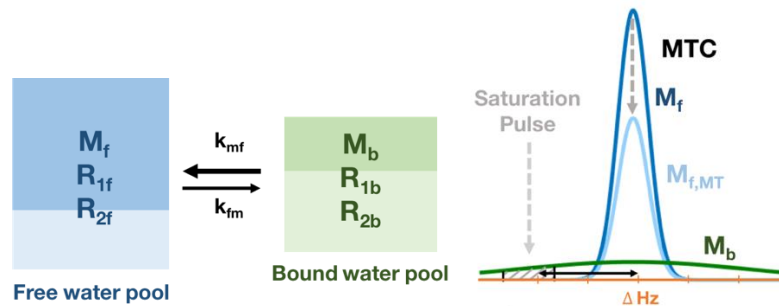


**Figure 9: Schematic representations of the MT effect.** (Left) A two-pool model used to depict exchange between free water (f) and bound/macromolecular water (b). Lightly shaded regions in each pool represent saturated spins with  $M$ ,  $R_1$  and  $R_2$  denoting magnetization, longitudinal and transverse relaxation rates respectively. MT exchanges between the two pools are represented as  $k_{mf}$  and  $k_{fm}$ . (Right) Spectral representation of the MT effect. Bound or macromolecular protons have a much broader lineshape than free protons due to their fast  $T_2$  decay. By using an off-resonance RF pulse (shaded gray arrow), bound spins are saturated. Due to the interactions with the free proton pool, saturation is further transferred to the free water pool. This causes an attenuation (black arrow) in the bulk water magnetization  $M_{f,MT}$  and thus generating signals with MT contrast in the signal.

In order to characterize the MT effect, pseudo-quantitative magnetization transfer ratio (MTR) (Wolff and Balaban, 1989a) and quantitative MT (qMT) (Gochberg and Gore, 2003; Henkelman et al., 1993a; Sled and Pike, 2000) methods have been developed. MTR has been the more popular approach to assessing changes in macromolecular composition under different pathological conditions (Catalaa et al., 2000; McDaniel et al., 2007; Odrobina et al., 2005; Quesson et al., 1997; Schmierer et al., 2004a) and in the spinal cord (Ng et al., 2009; Wang et al., 2014). However, MTR measurements are also sensitive to non-MT effects such as different field strengths,  $B_0$  and  $B_1$  inhomogeneities and tissue relaxation times (Berry et al., 1999; Henkelman et al., 1993a; Stanisz et al., 2005). On the other hand, qMT methods, which extract numerical parameters from

a model, mitigate these effects and provide additional measurements that are reflective of molecular interactions in the two pools of protons. One common approach involves acquisition of a series of images wherein macromolecular protons undergo different saturation powers at multiple frequency offsets.

To date, there have only been a handful of *in vivo* spinal qMT reports due to several challenges that arise. In the human spine, qMT was first applied to assess myelin integrity in patients with a genetic disorder (Smith et al., 2009) and in multiple sclerosis patients (Smith et al., 2017, 2014). A recent effort has also proposed an optimized imaging protocol for robust qMT measurement in the cervical spinal cord (Battiston et al., 2018). In rodents, Harkins et al. used a combination of qMT, multi-exponential analysis of transverse relaxation and quantitative histology to characterize intra-myelin edema in the cervical spinal cord (Harkins et al., 2013). Moreover, qMT has also been used to evaluate recovery after introduction of a dorsal column lesion in NHPs (Wang et al., 2016a). An important property of tissues with MT present is the pool size ratio (PSR) which is the ratio of the number of immobilized macromolecule protons to the “free” water pool. In this thesis, we used the Henkelman-Ramani model to derive PSR measurements in order to monitor tissue changes after a spinal contusion injury in rats.

### **1.3.6. fMRI in the spinal cord**

With the basic principles of fMRI discussed in Chapter 1.2, this section outlines its applications in the spinal cord for both stimulus-evoked and resting-state fMRI. Because the spinal cord is shelled by the vertebral column and is relatively inaccessible, the only other possible methods for assessing spinal function are through either invasive electrode recordings or responses and reflexes to different peripheral stimuli from subjects. Neither of these options are reliable or ethical in humans and thus, the translation of fMRI to the spine becomes especially significant.

The first published fMRI study in the spinal cord reported local activations in the ipsilateral gray matter of the cervical spinal cord to a hand-closing task (Yoshizawa et al., 1996). Subsequent spinal fMRI studies also observed consistent features in healthy volunteers (Madi et al., 2001; Stroman et al., 1999). Building upon these early reports, various groups began to investigate the distribution of stimulus activation with different stimuli at different levels of the human spinal cord (Stroman, 2005). Clinically, patients with spinal cord injury and multiple sclerosis were found to demonstrate different activation patterns than those of healthy subjects (Kornelsen and Mackey,

2007; Stroman, 2005). On top of these results from human spinal studies that have suggested a high correspondence between fMRI and neuronal functions, direct evidences have been revealed by animal models. For example, fMRI responses to noxious electrical stimulation in rats were validated with immunohistology (Lawrence et al., 2004) and NHP spinal cords acquired at high field revealed mesoscale local functional organizations following noxious heat and tactile stimuli (Yang et al., 2015).

Building upon these findings, the ability to perform rsfMRI in the spinal cord presents an attractive biomarker for evaluating the functional integrity of the spine. However, this concept has been largely unexplored with only a handful of publications to date. Two of the keys to successful detection of rsfMRI in the spinal cord are devising an appropriate sequence and protocol for image acquisition, and an optimized set of pre-processing procedures for teasing out low-frequency BOLD signal fluctuations. Generally, two methods have been used to analyze rsfMRI in the spinal cord: data-driven and ROI-based methods. Notably, Kong et al. found distinct dorsal and ventral networks that mirrored spinal cord neuroanatomy using independent component analysis (Kong et al., 2014). With an ROI based approach, Barry et al. also found consistent functional connectivity in bilateral motor and sensory networks (Barry et al., 2015, 2014). More recent reports have also investigated resting-state networks across the different segments of the cervical spine, and quantitatively evaluated the contributions of motion and physiological noises (Liu et al., 2016; Shreyas Harita and Stroman, 2017). Importantly, spinal rsfMRI has also been applied to evaluate changes in multiple sclerosis patients (Conrad et al., 2018) and NHPs with a dorsal column lesion (Chen et al., 2015). While these findings may suggest spinal rsfMRI as a robust technique for clinical applications, assessment of its reproducibility and direct validation are still needed for accurate interpretations. Thus, in this thesis, previously established spinal rsfMRI observations were validated with invasive electrophysiology in NHPs (Chapter 2) and also translated to a rodent model (Chapter 3).

### **1.3.7. Challenges in imaging of the spinal cord**

One of the challenges to imaging the spinal cord is its small physical size. Unlike the brain, the spinal cord is only approximately 6 mm in diameter at the cervical enlargement in NHPs (Figure 10). In order to accurately depict anatomical details and minimize partial volume effects, in-plane resolution of <1 mm is needed, which may require trading-off SNR or compromising

shorter scan times. On top of its small dimensions, a layer of muscle is also present between the spinal cord and the back of the animal; approximately 8.5 mm for NHPs and 5 mm for rats. If a surface coil is used, detection of signals from deeper tissues requires coils with relatively large diameters. In turn, this would not only increase noise level captured (Ford et al., 1994) with additional motion artifacts introduced with the coil covering areas away from the ROI.

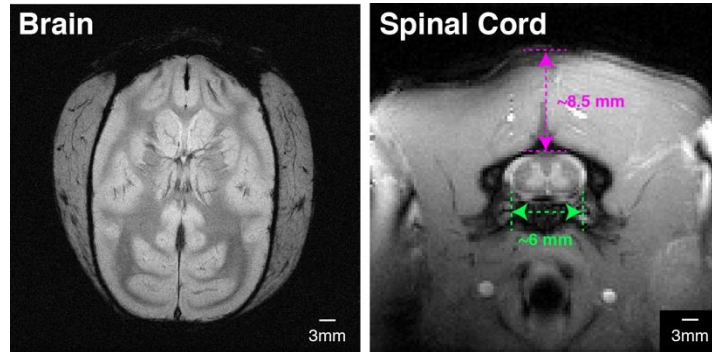


**Figure 10: Anatomical images of NHP brain and spinal cord.** (Left)  $T_2^*$  weighted transverse image of the NHP brain. (Right) MTC weighted anatomical image of the cervical spinal cord. Diameter of the cervical enlargement is typically 6 mm (green) while depth from the surface of the neck to the spinal cord is roughly 8.5 mm. The small physical size of the spinal cord relative to the brain is one of the reasons that make spinal MRI challenging.

Another major challenge to imaging the spinal cord is field inhomogeneity. Because of the spinal cord's vicinity to the vertebrae bone, cartilages and air-filled lungs, image distortions and signal losses become issues due to the presence of considerable magnetic susceptibility differences. At lower cervical and upper thoracic regions of the spinal cord, field variations caused by lungs are further exacerbated. In order to mitigate these issues, optimized shimming within the spinal cord is one solution. While this method is able to improve field homogeneity, in practice it is unable to correct for local variations such as the alternation of vertebrae and vertebral disks along the spinal cord (Cohen-Adad and Wheeler-Kingshott, 2014). Another approach to alleviating these issues is by acquiring axial slices with orientations aligned with the intervertebral discs (Stroman and Ryner, 2001), as opposed to sagittal or coronal orientations. Although the axial orientation compromises the acquisition field of view, more reliable results in fMRI have been demonstrated. For example, functional activations observed in the sagittal acquisition have been less consistent with neuroanatomy and varying amplitude responses (Stroman, 2005). In human studies, multi-

shot gradient echo scans have been used to replace EPI acquisitions to reduce distortions (Barry et al., 2014).

Lastly, the detrimental effects of physiological noise on MR signals in the spinal cord cannot be overlooked. The spinal cord is surrounded by a layer of CSF, which flows in the rostral-caudal direction every time the heart beats. This pulsating CSF flow also causes the spinal cord to move within the spinal canal, although its displacements have been shown to diminish with increasing distance from the head (Figley and Stroman, 2007). The movement of the spinal cord is further aggravated with periodic motion from the heart and lungs. Respiratory movements can cause  $B_0$  changes as well as EPI images to shift from the movement itself. One way to compensate for these issues is to introduce respiration or cardiac gating, although this lengthens scans and varies the acquisition time per volume. Post-processing methods that require recoding of physiological signals, such as RETROICOR, has also been widely implemented to correct for their contributions to the BOLD signal (Glover et al., 2000). In animal studies, synchronization between data acquisition time and respiration can also be performed, which is a strategy employed in all studies in this thesis. Lastly, securely positioning the animals in the supine position can also significantly reduce motion related-artifacts during MRI acquisitions.

## **1.4. Specific aims**

With these considerations and background in mind, this thesis addresses three specific aims.

### **1.4.1. Aim 1**

*To validate the connectivity measures from resting-state fMRI signals in spinal cord by comparisons with quantitative electrophysiology in NHPs.* Resting-state and stimulus-driven (tactile and heat) fMRI data, and electrophysiological measurements are acquired in NHPs to compare these different metrics of neural activity. Specifically, the goal of this aim is to determine quantitatively the degree of correlation between electrophysiological measures and rsfMRI connectivity measures.

### **1.4.2. Aim 2**

*To demonstrate and quantify functional connectivity within the rat spinal cord.* Current imaging

protocols have proven successful in revealing resting-state functional networks in monkey and human studies, but whether they are detectable in rodents remains unknown. The goal of this aim is to a) determine the quality of BOLD images of the rat cervical spinal cord at 9.4T, b) detect intrinsic functional connectivity patterns using an ROI-based approach, and c) quantitatively evaluate functional connectivity between horns of the spinal cord in normal animals.

### **1.4.3. Aim 3**

*To apply structural and functional MRI methods to study changes in spinal cord before and after spinal cord injury.* Multi-parametric MRI images are acquired in groups of animals subjected to injuries of the spine. Specifically, a contusion injury model in rats is investigated. The goal of this aim is to a) determine how the functional integrity of injured spinal cord gray matter changes with injury; b) track structural (DTI) and molecular composition (qMT) longitudinal changes and c) relate MR data to histological and behavioral measures.

## **1.5. Appendix**

### **1.5.1. Appendix A: torque and magnetic moment**

In the presence of an external magnetic field ( $B_0$ ), a moving charge experiences a rotational force known as torque ( $\tau$ ) which can be expressed as the vector product between the magnetic moment ( $\mu$ ) and magnetic field. Similar to torque on a current loop, the amount of torque experienced depends on the angle ( $\theta$ ) between the moving charge direction and the main magnetic field, and is maximal when they are perpendicular to each other.

$$\tau = (\mu B_0)(\sin(\theta)) \quad (15)$$

Equation 15 can also be expressed in vector form,

$$\boldsymbol{\tau} = \boldsymbol{\mu} \times \mathbf{B}_0 \quad (16)$$

Because torque is also defined as the rate of change in angular momentum with time, we can then represent Equation 16 as:

$$\boldsymbol{\tau} = \frac{d\mathbf{J}}{dt} \quad (17)$$

Substitute Equation 16 into Equation 17,

$$\frac{d\mathbf{J}}{dt} = \boldsymbol{\mu} \times \mathbf{B}_0 \quad (18)$$

Additionally, the current flow and direction of rotation point to the same direction which implies that the magnetic moment and angular momentum are related by a scalar factor. This scalar factor is the gyromagnetic ratio,  $\boldsymbol{\mu} = \gamma\mathbf{J}$ , and can be substituted into Equation 18 to derive Equation 2 on page 3,

$$\frac{d\boldsymbol{\mu}}{dt} = \gamma(\boldsymbol{\mu} \times \mathbf{B}_0) \quad (19)$$

This derivation above can be found in various physics and MRI textbooks (Huettel; Song; McCarthy, 2004; Levitt, 2000; Nishimura, 2010), and is simply summarized here.

### 1.5.2. Appendix B: diffusion tensor model

The most commonly used diffusion-encoding scheme is known as the pulsed gradient spin-echo (PGSE) sequence (Stejskal and Tanner, 1965), where two diffusion gradient pulses are attached to the standard SE pulse sequence (Figure 11). After the initial 90-degree excitation pulse, the first diffusion gradient is applied at a particular direction to generate a phase variation with position. The 180-degree refocusing pulse then reverses the spin phases before the second diffusion gradient pulse is applied to rewind phases that were initially imposed. In the presence of diffusion,  $D$ , molecules alter their spatial positions and perfect refocusing would not be achieved, resulting in signal attenuation. This signal drop or phase difference is used to infer the degree of water motion, which depends on the distance moved in the direction of the gradient applied.

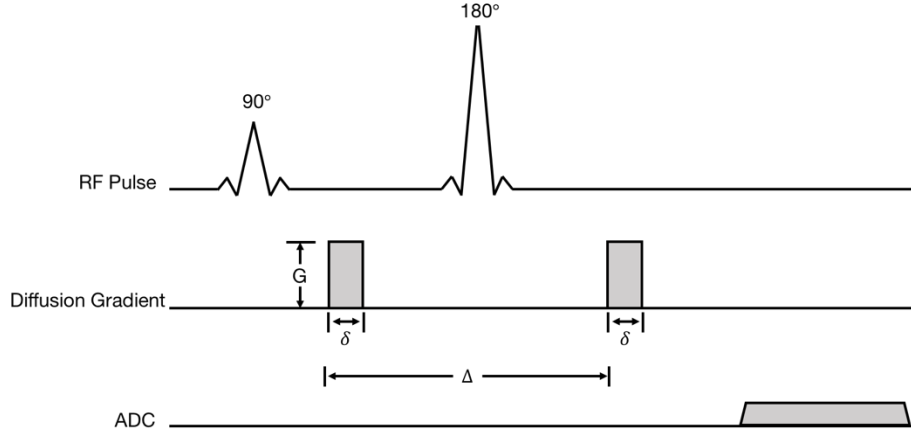


**Figure 11: Pulsed gradient spin-echo pulse sequence.** Protons are initially excited by a 90-degree excitation pulse and subsequently refocused by a 180-degree pulse. Diffusion gradients are placed before and after the 180-degree pulse with diffusion time ( $\Delta$ ), encoding time ( $\delta$ ) and gradient amplitude ( $G$ ). If spins were not stationary, a complete refocusing perfect refocusing would not be achieved. The signal attenuation that results are used to derive information about diffusion properties

The degree of diffusion sensitivity is characterized by a factor known as the b value, which is a function of diffusion time ( $\Delta$ ), encoding time ( $\delta$ ) and gradient amplitude ( $G$ ):

$$b = \gamma^2 G^2 \delta^2 \left( \Delta - \frac{\delta}{3} \right) \quad (20)$$

Larger b values signify a greater sensitivity towards diffusion, and this can be achieved by, for example, increasing the gradient amplitude and duration, and widening the time for molecules to diffuse. The diffusion weighted MR signal can also be described using b and D as:

$$S = S_0 e^{-bD} \quad (21)$$

where  $S$  and  $S_0$  denote signals with and without the application of diffusion weighted gradients respectively. Equation 21, however, is overly simplistic when describing anisotropy in white matter tracts. Instead, with diffusion encoded data collected from six or more directions, the diffusion tensor can be calculated. The diffusion tensor is represented by a 3 x 3 matrix with each number corresponding to diffusion coefficients measured in the x, y and z axis as well as between each of the axes. Mathematically, the updated diffusion weighted signal equation is described

using:

$$S = S_0 e^{-(\sum_{i=x,y,z} \sum_{j=x,y,z} b_{i,j} D_{i,j})} \quad (22)$$

$$b_{ij} = \gamma^2 \delta^2 \left( \Delta - \frac{\delta}{3} \right) G_i G_j = K G_i G_j \quad (23)$$

This can also be expressed in matrix form and subsequently solved by finding the least-squares solution:

$$Y = \frac{1}{b} \begin{pmatrix} -\ln\left(\frac{S_1}{S_0}\right) \\ \vdots \\ -\ln\left(\frac{S_N}{S_0}\right) \end{pmatrix} \quad (25)$$

$$H = \begin{pmatrix} G_{x1}^2 & G_{y1}^2 & G_{z1}^2 & 2G_{x1}G_{y1} & 2G_{x1}G_{z1} & 2G_{y1}G_{z1} \\ \vdots & \vdots & \vdots & \vdots & \vdots & \vdots \\ G_{xN}^2 & G_{yN}^2 & G_{zN}^2 & 2G_{xN}G_{yN} & 2G_{xN}G_{zN} & 2G_{yN}G_{zN} \end{pmatrix} \quad (26)$$

$$d = (D_{xx} \quad D_{yy} \quad D_{zz} \quad D_{xy} \quad D_{yz} \quad D_{yz})^T \quad (27)$$

$$Y = H d \quad (28)$$

$$d = (H^T H)^{-1} H^T Y \quad (29)$$

With the diffusion tensor computed, three principal eigenvectors can be derived by diagonalizing the matrix. They represent the main axes of the diffusion tensor along with three eigenvalues that indicate the magnitudes of the diffusion in their corresponding directions. The largest eigenvector is important for fiber tracking as it informs us of the axonal fiber orientations with its magnitude ( $\lambda_1$ ) termed longitudinal diffusivity. The two remaining eigenvectors orthogonal to the primary eigenvector correspond to diffusion transverse to axonal bundles with mean of their magnitudes  $\frac{(\lambda_2 + \lambda_3)}{2}$  termed radial diffusivity. Additionally, other commonly used metrics to describe diffusion in a voxel are ADC and FA:

$$ADC = \frac{\lambda_1 + \lambda_2 + \lambda_3}{3} \quad (30)$$

$$FA = \frac{\sqrt{(\lambda_1 - \lambda_2)^2 + (\lambda_2 - \lambda_3)^2 + (\lambda_3 - \lambda_1)^2}}{\sqrt{2}\sqrt{\lambda_1 + \lambda_2 + \lambda_3}} \quad (31)$$

### 1.5.3. Appendix C: qMT Henkelman-Ramani's model

Similar to our previous publication (Wang et al., 2015), the Henkelman-Ramani model (Cercignani and Barker, 2008; Ramani et al., 2002) was used to derive qMT parameters in the rat spinal cord:

$$S(\omega_{CWPE}, \Delta f) = \frac{M_0 \left( R_{1b} \left[ \frac{RM_{0b}}{R_{1a}} \right] + R_{RFB}(\omega_{1CWPE}, \Delta f, T_{2b}) + R_{1b} + \frac{RM_{0b}}{F} \right)}{\left[ \frac{RM_{0b}}{R_{1a}} \right] (R_{1b} + R_{RFB}(\omega_{1CWPE}, \Delta f, T_{2b})) + \left( 1 + \left[ \frac{\omega_{CWPE}}{2\pi\Delta f} \right]^2 \left[ \frac{1}{T_{2a}R_{1a}} \right] \right) (R_{RFB}(\omega_{1CWPE}, \Delta f, T_{2b}) + R_{1b} + \frac{RM_{0b}}{F})} \quad (32)$$

$S$  denotes the MT signal detected expressed as a function of irradiation amplitudes of continuous wave power equivalent ( $\omega_{CWPE}$ ) at multiple frequency offsets ( $\Delta f$ ).  $\omega_{CWPE}$  is proportional to the square of the flip angles ( $\theta_{sat}$ ) of the MT saturation pulse used, which were set at  $820^\circ$  and  $220^\circ$  in qMT studies in this thesis. Subscripts  $a$  and  $b$  represent protons from the free water and macromolecular pools respectively. The relative size of the macromolecular pool is represented by  $F$ , or more commonly known PSR.  $M_{0a}$  and  $M_{0b}$  represent fully relaxed magnetizations in the two pools while  $M_0$  is the magnetization signal without MT.  $R_{RFB}$  is the rate of saturation of the macromolecular pool, and is dependent on  $\omega_{CWPE}$ ,  $\Delta f$ , and transverse relaxation  $T_{2b}$ . Additionally,  $R_{1a}$  and  $R_{1b}$  are the longitudinal relaxation rates for protons in their respective proton pools. Lastly, two constraints were applied to the model: 1)  $R_{1b}$  was set as constant at  $1s^{-1}$  (Cercignani and Barker, 2008; Henkelman et al., 1993a; Ramani et al., 2002; Wang et al., 2015) and 2) observed relaxation rate ( $R_{1obs}$ ), which is linked to  $R_a$ , was obtained independently and included in the model.

$$R_{1a} = R_{1obs} - \frac{RM_{0b}(R_{1b} - R_{1obs})}{R_{1b} - R_{1obs} + \frac{RM_{0b}}{F}} \quad (33)$$

By fitting MRI data to the model, five parameters were estimated for each pixel:  $M_0$ ,  $F$ ,  $RM_{0b}$ ,  $T_{2A}$  and  $T_{2b}$ . Performance of the model fitting was estimated by evaluating the square 2-norm of the residuals at each  $\Delta f$ .

## 1.6. References

- Altman, P.L., Dittmer, D.S., 1973. Biology data book, Biological handbooks.
- Barry, R.L., Rogers, B.P., Smith, S.A., Gore, J.C., 2015. Reproducibility of resting state spinal cord networks at 7 Tesla 23, 3708. doi:10.1016/j.neuroimage.2016.02.058
- Barry, R.L., Smith, S.A., Dula, A.N., Gore, J.C., 2014. Resting state functional connectivity in the human spinal cord. *Elife* 2014, 1–15. doi:10.7554/eLife.02812
- Basser, P.J., Mattiello, J., LeBihan, D., 1994. MR diffusion tensor spectroscopy and imaging. *Biophys. J.* 66, 259–267. doi:10.1016/S0006-3495(94)80775-1
- Battiston, M., Grussu, F., Ianus, A., Schneider, T., Prados, F., Fairney, J., Ourselin, S., Alexander, D.C., Cercignani, M., Gandini Wheeler-Kingshott, C.A.M., Samson, R.S., 2018. An optimized framework for quantitative magnetization transfer imaging of the cervical spinal cord in vivo. *Magn. Reson. Med.* 79, 2576–2588. doi:10.1002/mrm.26909
- Bernstein, M.A., King, K.F., Zhou, X.J., 2004. Handbook of MRI Pulse Sequences, Handbook of MRI Pulse Sequences. doi:10.1016/B978-0-12-092861-3.X5000-6
- Berry, I., Barker, G.J., Barkhof, F., Campi, A., Dousset, V., Franconi, J.M., Gass, A., Schreiber, W., Miller, D.H., Tofts, P.S., 1999. A multicenter measurement of magnetization transfer ratio in normal white matter. *J. Magn. Reson. Imaging* 9, 441–446. doi:10.1002/(SICI)1522-2586(199903)9:3<441::AID-JMRI12>3.0.CO;2-R
- Birn, R.M., Smith, M.A., Jones, T.B., Bandettini, P.A., 2008. The respiration response function: The temporal dynamics of fMRI signal fluctuations related to changes in respiration. *Neuroimage* 40, 644–654. doi:10.1016/j.neuroimage.2007.11.059
- Biswal, B., Zerrin Yetkin, F., Haughton, V.M., Hyde, J.S., 1995. Functional connectivity in the motor cortex of resting human brain using echo planar mri. *Magn. Reson. Med.* 34, 537–541. doi:10.1002/mrm.1910340409
- Biswal, B.B., Kylen, J. Van, Hyde, J.S., 1997. Simultaneous assessment of flow and BOLD signals in resting-state functional Simultaneous Assessment of Flow and BOLD Signals in Resting-State Functional Connectivity Maps. *NMR Biomed.* 10, 165–170. doi:10.1002/(SICI)1099-1492(199706/08)10
- Bloch, F., 1953. The principle of nuclear induction. *Science* (80-. ). 118, 425–430. doi:10.1126/science.118.3068.425

- Bloch, F., 1951. Nuclear induction. *Physica* 17, 272–281. doi:10.1016/0031-8914(51)90068-7
- Brown, T.G., 1914. On the nature of the fundamental activity of the nervous centres; together with an analysis of the conditioning of rhythmic activity in progression, and a theory of the evolution of function in the nervous system. *J. Physiol.* 48, 18–46. doi:10.1113/jphysiol.1914.sp001646
- Brown, T.G., 1912. The Factors in Rhythmic Activity of the Nervous System. *R. Soc. Publ.* 85, 278–289. doi:Doi 10.1098/Rspb.1912.0051
- Brown, T.G., 1911. The Intrinsic Factors in the Act of Progression in the Mammal. *Proc. R. Soc. B Biol. Sci.* 84, 308–319. doi:10.1098/rspb.1911.0077
- Calhoun, V., Golay, X., Pearlson, G., 2000. Improved fMRI slice timing correction: interpolation errors and wrap around effects. *Proceedings, ISMRM, 9th Annu. Meet. Denver* 810.
- Catalaa, I., Grossman, R.I., Kolson, D.L., Udupa, J.K., Nyul, L.G., Wei, L., Zhang, X., Polansky, M., Mannon, L.J., McGowan, J.C., 2000. Multiple Sclerosis: Magnetization Transfer Histogram Analysis of Segmented Normal-appearing White Matter. *Radiology* 216, 351–355. doi:10.1148/radiology.216.2.r00au16351
- Cercignani, M., Barker, G.J., 2008. A comparison between equations describing in vivo MT: The effects of noise and sequence parameters. *J. Magn. Reson.* 191, 171–183. doi:10.1016/j.jmr.2007.12.012
- Chang, C., Cunningham, J.P., Glover, G.H., 2009. Influence of heart rate on the BOLD signal: The cardiac response function. *Neuroimage* 44, 857–869. doi:10.1016/j.neuroimage.2008.09.029
- Chen, L.M., Mishra, A., Yang, P.-F., Wang, F., Gore, J.C., 2015. Injury alters intrinsic functional connectivity within the primate spinal cord. *Proc. Natl. Acad. Sci. U. S. A.* 112, 5991–6. doi:10.1073/pnas.1424106112
- Cohen-Adad, J., Wheeler-Kingshott, C., 2014. Quantitative MRI of the Spinal Cord, Quantitative MRI of the Spinal Cord. doi:10.1016/C2011-0-07594-4
- Conrad, B.N., Barry, R.L., Rogers, B.P., Maki, S., Mishra, A., Thukral, S., Sriram, S., Bhatia, A., Pawate, S., Gore, J.C., Smith, S.A., 2018. Multiple sclerosis lesions affect intrinsic functional connectivity of the spinal cord. *Brain*. doi:10.1093/brain/awy083
- Cordes, D., Haughton, V., Carew, J.D., Arfanakis, K., Maravilla, K., 2002. Hierarchical clustering to measure connectivity in fMRI resting-state data. *Magn. Reson. Imaging* 20, 305–317. doi:10.1016/S0730-725X(02)00503-9

- Cordes, D., Haughton, V.M., Arfanakis, K., Carew, J.D., Turski, P.A., Moritz, C.H., Quigley, M.A., Meyerand, M.E., 2001. Frequencies contributing to functional connectivity in the cerebral cortex in “resting-state” data. *Am. J. Neuroradiol.* 22, 1326–1333.
- Cordes, D., Haughton, V.M., Arfanakis, K., Wendt, G.J., Turski, P.A., Moritz, C.H., Quigley, M.A., Meyerand, M.E., 2000. Mapping functionally related regions of brain with functional connectivity MR imaging. *Am. J. Neuroradiol.* 21, 1636–1644. doi:10.1016/j.amepre.2011.10.016
- Damoiseaux, J.S., Rombouts, S.A.R.B., Barkhof, F., Scheltens, P., Stam, C.J., Smith, S.M., Beckmann, C.F., 2006. Consistent resting-state networks across healthy subjects. *Proc. Natl. Acad. Sci.* 103, 13848–13853. doi:10.1073/pnas.0601417103
- De Luca, M., Smith, S., De Stefano, N., Federico, A., Matthews, P.M., 2005. Blood oxygenation level dependent contrast resting state networks are relevant to functional activity in the neocortical sensorimotor system. *Exp. Brain Res.* 167, 587–594. doi:10.1007/s00221-005-0059-1
- Dietz, V., 2003. Spinal cord pattern generators for locomotion. *Clin. Neurophysiol.* doi:10.1016/S1388-2457(03)00120-2
- Einevoll, G.T., Kayser, C., Logothetis, N.K., Panzeri, S., 2013. Modelling and analysis of local field potentials for studying the function of cortical circuits. *Nat. Rev. Neurosci.* doi:10.1038/nrn3599
- Einstein, A., 1905. On the Motion of Small Particles Suspended in Liquids at Rest Required by the Molecular-Kinetic Theory of Heat. *Ann. Phys.* 17, 549–560. doi:10.1002/andp.19053220806
- Figley, C.R., Stroman, P.W., 2007. Investigation of human cervical and upper thoracic spinal cord motion: Implications for imaging spinal cord structure and function. *Magn. Reson. Med.* 58, 185–189. doi:10.1002/mrm.21260
- Ford, J.C., Hackney, D.B., Joseph, P.M., Phelan, M., Alsop, D.C., Tabor, S.L., Hand, C.M., Markowitz, R.S., Black, P., 1994. A method for in vivo high resolution MRI of rat spinal cord injury. *Magn. Reson. Med.* 31. doi:10.1002/mrm.1910310216
- Fox, M.D., Raichle, M.E., 2007. Spontaneous fluctuations in brain activity observed with functional magnetic resonance imaging. *Nat Rev Neurosci* 8, 700–711. doi:nrn2201 [pii]\n10.1038/nrn2201
- Fox, P.T., Raichle, M.E., 1986. Focal physiological uncoupling of cerebral blood flow and oxidative metabolism during somatosensory stimulation in human subjects. *Proc. Natl. Acad. Sci. U. S. A.* 83, 1140–4. doi:10.1073/pnas.83.4.1140

- Fox, P.T., Raichle, M.E., 1984. Stimulus rate dependence of regional cerebral blood flow in human striate cortex, demonstrated by positron emission tomography. *J. Neurophysiol.* 51, 1109–1120. doi:10.1152/jn.1984.51.5.1109
- Fox, P.T., Raichle, M.E., Mintun, M.A., Dence, C., 1988. Nonoxidative glucose consumption during focal physiologic neural activity. *Science* (80-. ). 241, 462–464. doi:10.1126/science.3260686
- Friston, K.J., Ashburner, J., Frith, C.D., Poline, J. - B, Heather, J.D., Frackowiak, R.S.J., 1995. Spatial registration and normalization of images. *Hum. Brain Mapp.* 3, 165–189. doi:10.1002/hbm.460030303
- Fröhlich, F., Fröhlich, F., 2016. Chapter 17 – Low-Frequency Oscillations, in: *Network Neuroscience*. pp. 231–242. doi:10.1016/B978-0-12-801560-5.00017-3
- Glover, G.H., Li, T.Q., Ress, D., 2000. Image-based method for retrospective correction of physiological motion effects in fMRI: RETROICOR. *Magn. Reson. Med.* 44, 162–167. doi:10.1002/1522-2594(200007)44:1<162::AID-MRM23>3.0.CO;2-E
- Gochberg, D.F., Gore, J.C., 2003. Quantitative imaging of magnetization transfer using an inversion recovery sequence. *Magn. Reson. Med.* 49, 501–505. doi:10.1002/mrm.10386
- Goldman, M., 2001. Advances in magnetic resonance: Formal theory of spin-lattice relaxation. *J. Magn. Reson.* doi:10.1006/jmre.2000.2239
- Gore, J.C.J.C., 2003. Principles and practice of functional MRI of the human brain. *J. Clin. Invest.* 112, 4–9. doi:10.1172/JCI200319010.
- Greicius, M.D., Krasnow, B., Reiss, A.L., Menon, V., 2003. Functional connectivity in the resting brain: a network analysis of the default mode hypothesis. *Proc. Natl. Acad. Sci. U. S. A.* 100, 253–8. doi:10.1073/pnas.0135058100
- Grillner, S., Deliagina, T., El Manira, A., Hill, R.H., Orlovsky, G.N., Wallén, P., Ekeberg, Ö., Lansner, A., 1995. Neural networks that co-ordinate locomotion and body orientation in lamprey. *Trends Neurosci.* doi:10.1016/0166-2236(95)80008-P
- Guertin, P. a, 2012. Central pattern generator for locomotion: anatomical, physiological, and pathophysiological considerations. *Front. Neurol.* 3, 183. doi:10.3389/fneur.2012.00183
- Hadi, B., Zhang, Y.P., Burke, D. a, Shields, C.B., Magnuson, D.S., 2000. Lasting paraplegia caused by loss of lumbar spinal cord interneurons in rats: no direct correlation with motor neuron loss. *J.*

- Neurosurg. 93, 266–75. doi:10.3171/spi.2000.93.2.0266
- Hahn, E.L., 1950. Spin Echoes. *Phys. Rev.* 80, 580–594. doi:10.1103/PhysRev.80.580
- Haller, S., Bartsch, A.J., 2009. Pitfalls in fMRI. *Eur. Radiol.* doi:10.1007/s00330-009-1456-9
- Harkins, K.D., Valentine, W.M., Gochberg, D.F., Does, M.D., 2013. In-vivo multi-exponential T2, magnetization transfer and quantitative histology in a rat model of intramyelinic edema. *NeuroImage Clin.* 2, 810–817. doi:10.1016/j.nicl.2013.06.007
- Henkelman, R.M., Huang, X., Xiang, Q.-S., Stanisz, G., Swanson, S., Bronskill, M., 1993. Quantitative interpretation of magnetization transfer. *Magn. Reson. Med.* 29, 759–766. doi:10.1002/mrm.1910290607
- Henkelman, R.M., Stanisz, G.J., Graham, S.J., 2001. Magnetization transfer in MRI: A review. *NMR Biomed.* doi:10.1002/nbm.683
- Horsfield, M.A., Jones, D.K., 2002. Applications of diffusion-weighted and diffusion tensor MRI to white matter diseases - A review. *NMR Biomed.* doi:10.1002/nbm.787
- Hoult, D.I., Chen, C. - N, Sank, V.J., 1986. The field dependence of NMR imaging. II. Arguments concerning an optimal field strength. *Magn. Reson. Med.* 3, 730–746. doi:10.1002/mrm.1910030509
- Huettel; Song; McCarthy, 2004. *Functional Magnetic Resonance Imaging*, Book.
- Hutchison, R.M., Everling, S., 2012. Monkey in the middle: why non-human primates are needed to bridge the gap in resting-state investigations. *Front. Neuroanat.* 6, 29. doi:10.3389/fnana.2012.00029
- Jenkinson, M., Bannister, P., Brady, M., Smith, S., 2002. Improved optimization for the robust and accurate linear registration and motion correction of brain images. *Neuroimage* 17, 825–841. doi:10.1016/S1053-8119(02)91132-8
- Katzner, S., Nauhaus, I., Benucci, A., Bonin, V., Ringach, D.L., Carandini, M., 2009. Local Origin of Field Potentials in Visual Cortex. *Neuron* 61, 35–41. doi:10.1016/j.neuron.2008.11.016
- Kong, Y., Eippert, F., Beckmann, C.F., Andersson, J., Finsterbusch, J., Buchel, C., Tracey, I., Brooks, J.C., 2014. Intrinsically organized resting state networks in the human spinal cord. *Proc Natl Acad Sci U S A* 111, 18067–18072. doi:10.1073/pnas.1414293111
- Kornelsen, J., Mackey, S., 2007. Potential clinical applications for spinal functional MRI. *Curr. Pain*

Headache Rep. doi:10.1007/s11916-007-0186-4

Kucharczyk, W., Macdonald, P.M., Stanisiz, G.J., Henkelman, R.M., 1994. Relaxivity and magnetization transfer of white matter lipids at MR imaging: importance of cerebroside and pH. *Radiology* 192, 521–529. doi:10.1148/radiology.192.2.8029426

Lai, S., Hopkins, A.L., Haacke, E.M., Li, D., Wasserman, B.A., Buckley, P., Friedman, L., Meltzer, H., Hedera, P., Friedland, R., 1993. Identification of vascular structures as a major source of signal contrast in high resolution 2D and 3D functional activation imaging of the motor cortex at 1.5T preliminary results. *Magn. Reson. Med.* 30, 387–392. doi:10.1002/mrm.1910300318

Lauterbur, P.C., 1973. Image formation by induced local interactions: examples employing nuclear magnetic .... *Nature*.

Lawrence, J., Stroman, P.W., Bascaramurty, S., Jordan, L.M., Malisza, K.L., 2004. Correlation of functional activation in the rat spinal cord with neuronal activation detected by immunohistochemistry. *Neuroimage* 22, 1802–1807. doi:10.1016/j.neuroimage.2004.04.001

Lee, M.H., Smyser, C.D., Shimony, J.S., 2013. Resting-State fMRI: A Review of Methods and Clinical Applications. *Am. J. Neuroradiol.* 34, 1866–1872. doi:10.3174/ajnr.A3263

Lee, S.P., Silva, A.C., Ugurbil, K., Kim, S.G., 1999. Diffusion-weighted spin-echo fMRI at 9.4 T: Microvascular/tissue contribution to BOLD signal changes. *Magn. Reson. Med.* 42, 919–928. doi:10.1002/(SICI)1522-2594(199911)42:5<919::AID-MRM12>3.0.CO;2-8

Levitt, M., 2000. *Spin Dynamics: Basics of Nuclear Magnetic Resonance*, John Wiley & Sons Ltd. doi:10.1002/cmra.20130

Liu, X., Zhou, F., Li, X., Qian, W., Cui, J., Zhou, I.Y., Luk, K.D.K., Wu, E.X., Hu, Y., 2016. Organization of the intrinsic functional network in the cervical spinal cord: A resting state functional MRI study. *Neuroscience* 336, 30–38. doi:10.1016/j.neuroscience.2016.08.042

Logothetis, N.K., Pauls, J., Augath, M., Trinath, T., Oeltermann, A., 2001. Neurophysiological investigation of the basis of the fMRI signal. *Nature* 412, 150–7. doi:10.1038/35084005

Lowe, M.J., Dzemidzic, M., Lurito, J.T., Mathews, V.P., Phillips, M.D., 2000. Correlations in low-frequency BOLD fluctuations reflect cortico-cortical connections. *Neuroimage* 12, 582–587. doi:10.1006/nimg.2000.0654

Madi, S., Flanders, a E., Vinitski, S., Herbison, G.J., Nissanov, J., 2001. Functional MR imaging of the

- human cervical spinal cord. *AJNR. Am. J. Neuroradiol.* 22, 1768–1774.
- Magnuson, D.S.K., Trinder, T.C., Zhang, Y.P., Burke, D., Morassutti, D.J., Shields, C.B., 1999. Comparing deficits following excitotoxic and contusion injuries in the thoracic and lumbar spinal cord of the adult rat. *Exp. Neurol.* 156, 191–204. doi:10.1006/exnr.1999.7016
- Magri, C., Schridde, U., Murayama, Y., Panzeri, S., Logothetis, N.K., 2012. The Amplitude and Timing of the BOLD Signal Reflects the Relationship between Local Field Potential Power at Different Frequencies. *J. Neurosci.* 32, 1395–1407. doi:10.1523/JNEUROSCI.3985-11.2012
- Mansfield, P., 1977. Multi-planar image formation using NMR spin echoes. *J. Phys. C Solid State Phys.* 10, L55–L58. doi:10.1088/0022-3719/10/3/004
- Marder, E., Bucher, D., 2001. Central pattern generators and the control of rhythmic movements. *Curr. Biol.* doi:10.1016/S0960-9822(01)00581-4
- McDaniel, J.D., Ulmer, J.L., Prost, R.W., Franczak, M.B., Jaradeh, S., Hamilton, C. a, Mark, L.P., 2007. Magnetization transfer imaging of skeletal muscle in autosomal recessive limb girdle muscular dystrophy. *J. Comput. Assist. Tomogr.* 23, 609–14.
- Menon, R.S., Ogawa, S., Tank, D.W., Uğurbil, K., 1993. 4 Tesla gradient recalled echo characteristics of photic stimulation - induced signal changes in the human primary visual cortex. *Magn. Reson. Med.* 30, 380–386. doi:10.1002/mrm.1910300317
- Ng, M.C., Hua, J., Hu, Y., Luk, K.D., Lam, E.Y., 2009. Magnetization transfer (MT) asymmetry around the water resonance in human cervical spinal cord. *J. Magn. Reson. Imaging* 29, 523–528. doi:10.1002/jmri.21610
- Nir, Y., Mukamel, R., Dinstein, I., Privman, E., Harel, M., Fisch, L., Gelbard-Sagiv, H., Kipervasser, S., Andelman, F., Neufeld, M.Y., Kramer, U., Arieli, A., Fried, I., Malach, R., 2008. Interhemispheric correlations of slow spontaneous neuronal fluctuations revealed in human sensory cortex. *Nat. Neurosci.* 11, 1100–1108. doi:10.1038/nn.2177
- Nishimura, D., 2010. *Principles of Magnetic Resonance Imaging.* Stanford University.
- Odrobina, E.E., Lam, T.Y.J., Pun, T., Midha, R., Stanisz, G.J., 2005. MR properties of excised neural tissue following experimentally induced demyelination. *NMR Biomed.* 18, 277–284. doi:10.1002/nbm.951
- Ogawa, S., Lee, T., 1990. Brain magnetic resonance imaging with contrast dependent on blood

- oxygenation. *Proc. ...* 87, 9868–72. doi:10.1073/pnas.87.24.9868
- Ogawa, S., Lee, T.M., Nayak, A.S., Glynn, P., 1990. Oxygenation-sensitive contrast in magnetic resonance image of rodent brain at high magnetic fields. *Magn. Reson. Med.* 14, 68–78. doi:10.1002/mrm.1910140108
- Ogawa, S., Tank, D.W., Menon, R., Ellermann, J.M., Kim, S.G., Merkle, H., Ugurbil, K., 1992. Intrinsic signal changes accompanying sensory stimulation: functional brain mapping with magnetic resonance imaging. *Proc Natl Acad Sci U S A* 89, 5951–5955. doi:10.1073/pnas.89.13.5951
- Pauling, L., Coryell, C.D., 1936. THE MAGNETIC PROPERTIES AND STRUCTURE OF THE HEMOCHROMOGENS AND RELATED SUBSTANCES. *Proc. Natl. Acad. Sci.* 22, 159–163.
- Purcell, E., Torrey, H., Pound, R., 1946. Resonance Absorption by Nuclear Magnetic Moments in a Solid. *Phys. Rev.* 69, 37–38. doi:10.1103/PhysRev.69.37
- Quesson, B., Bouzier, A.-K., Thiaudiere, E., Delalande, C., Merle, M., Canioni, P., 1997. Magnetization transfer fast imaging of implanted glioma in the rat brain at 4.7T - Interpretation using a binary spin-bath model. *J. Magn. Reson. Imaging* 7, 1076–1083.
- Ramani, A., Dalton, C., Miller, D.H., Tofts, P.S., Barker, G.J., 2002. Precise estimate of fundamental in-vivo MT parameters in human brain in clinically feasible times. *Magn. Reson. Imaging* 20, 721–731. doi:10.1016/S0730-725X(02)00598-2
- Rexed, B., 1952. The cytoarchitectonic organization of the spinal cord in the cat. *J. Comp. Neurol.* 96, 415–495. doi:10.1002/cne.900960303
- Robson, M.D., Dorosz, J.L., Gore, J.C., 1998. Measurements of the temporal fMRI response of the human auditory cortex to trains of tones. *Neuroimage* 7, 185–198. doi:10.1006/nimg.1998.0322
- Schmierer, K., Scaravilli, F., Altmann, D.R., Barker, G.J., Miller, D.H., 2004. Magnetization transfer ratio and myelin in postmortem multiple sclerosis brain. *Ann. Neurol.* 56, 407–415. doi:10.1002/ana.20202
- Shi, Z., Wu, R., Yang, P.-F., Wang, F., Wu, T.-L., Mishra, A., Chen, L.M., Gore, J.C., 2017. High spatial correspondence at a columnar level between activation and resting state fMRI signals and local field potentials. *Proc. Natl. Acad. Sci.* 201620520. doi:10.1073/pnas.1620520114
- Shmuel, A., Leopold, D.A., 2008. Neuronal correlates of spontaneous fluctuations in fMRI signals in monkey visual cortex: Implications for functional connectivity at rest. *Hum. Brain Mapp.* 29, 751–

761. doi:10.1002/hbm.20580

- Shmuel, A., Yacoub, E., Pfeuffer, J., Van de Moortele, P.F., Adriany, G., Hu, X., Ugurbil, K., 2002. Sustained negative BOLD, blood flow and oxygen consumption response and its coupling to the positive response in the human brain. *Neuron* 36, 1195–1210. doi:10.1016/S0896-6273(02)01061-9
- Shreyas Harita, Stroman, P.W., 2017. Confirmation of resting-state BOLD fluctuations in the human brainstem and spinal cord after identification and removal of physiological noise. *Magn. Reson. Med.* doi:10.1002/mrm.26606
- Sled, J.G., Pike, G.B., 2000. Quantitative Interpretation of Magnetization Transfer in Spoiled Gradient Echo MRI Sequences. *J. Magn. Reson.* 145, 24–36. doi:10.1006/jmre.2000.2059
- Smith, A.K., By, S., Lyttle, B.D., Dortch, R.D., Box, B.A., Mckeithan, L.J., Thukral, S., Bagnato, F., Pawate, S., Smith, S.A., 2017. Evaluating single-point quantitative magnetization transfer in the cervical spinal cord: Application to multiple sclerosis. *NeuroImage Clin.* 16, 58–65. doi:10.1016/j.nicl.2017.07.010
- Smith, A.K., Dortch, R.D., Dethrage, L.M., Smith, S.A., 2014. Rapid, high-resolution quantitative magnetization transfer MRI of the human spinal cord. *Neuroimage* 95, 106–116. doi:10.1016/j.neuroimage.2014.03.005
- Smith, S. a, Golay, X., Fatemi, A., Mahmood, A., Raymond, G. V, Moser, H.W., van Zijl, P.C.M., Stanisz, G.J., 2009. Quantitative magnetization transfer characteristics of the human cervical spinal cord in vivo: application to adrenomyeloneuropathy. *Magn. Reson. Med.* 61, 22–7. doi:10.1002/mrm.21827
- Standring, S., 2016. *Gray's Anatomy*, Elsevier. doi:10.1308/003588406X116873
- Stanisz, G.J., Odrobina, E.E., Pun, J., Escaravage, M., Graham, S.J., Bronskill, M.J., Henkelman, R.M., 2005. T1, T2 relaxation and magnetization transfer in tissue at 3T. *Magn. Reson. Med.* 54, 507–512. doi:10.1002/mrm.20605
- Stejskal, E.O., Tanner, J.E., 1965. Spin diffusion measurements: Spin echoes in the presence of a time-dependent field gradient. *J. Chem. Phys.* 42, 288–292. doi:10.1063/1.1695690
- Stroman, P.W., 2005. Magnetic Resonance Imaging of Neuronal Function in the Spinal Cord: Spinal fMRI. *Clin. Med. Res.* 3, 146–156. doi:10.3121/cmr.3.3.146
- Stroman, P.W., Nance, P.W., Ryner, L.N., 1999. BOLD MRI of the human cervical spinal cord at 3 tesla.

- Magn. Reson. Med. 42, 571–576.
- Stroman, P.W., Ryner, L.N., 2001. Functional MRI of motor and sensory activation in the human spinal cord. *Magn. Reson. Imaging* 19, 27–32. doi:10.1016/S0730-725X(01)00226-0
- Torrey, H.C., 1956. Bloch equations with diffusion terms. *Phys. Rev.* 104, 563–565. doi:10.1103/PhysRev.104.563
- Ugurbil, K., Kim, D., Duong, T., Hu, X., Ogawa, S., 2001. Magnetic resonance imaging of brain function and neurochemistry. *Proc. IEEE*.
- Van Buuren, M., Gladwin, T.E., Zandbelt, B.B., Van Den Heuvel, M., Ramsey, N.F., Kahn, R.S., Vink, M., 2009. Cardiorespiratory effects on default-mode network activity as measured with fMRI. *Hum. Brain Mapp.* 30, 3031–3042. doi:10.1002/hbm.20729
- van den Heuvel, M.P., Hulshoff Pol, H.E., 2010. Exploring the brain network: A review on resting-state fMRI functional connectivity. *Eur. Neuropsychopharmacol.* doi:10.1016/j.euroneuro.2010.03.008
- van Dijk, K.R.A., Sabuncu, M.R., Buckner, R.L., 2012. The influence of head motion on intrinsic functional connectivity MRI. *Neuroimage* 59, 431–438. doi:10.1016/j.neuroimage.2011.07.044
- Wang, F., Li, K., Mishra, A., Gochberg, D., Chen, L.M., Gore, J.C., 2016. Longitudinal assessment of spinal cord injuries in nonhuman primates with quantitative magnetization transfer. *Magn. Reson. Med.* 75, 1685–1696. doi:10.1002/mrm.25725
- Wang, F., Li, K., Mishra, A., Gochberg, D., Min Chen, L., Gore, J.C., 2015. Longitudinal assessment of spinal cord injuries in nonhuman primates with quantitative magnetization transfer. *Magn. Reson. Med.* 1696, 1685–1696. doi:10.1002/mrm.25725
- Wang, F., Qi, H.-X., Zu, Z., Mishra, A., Tang, C., Gore, J.C., Chen, L.M., 2014. Multiparametric MRI reveals dynamic changes in molecular signatures of injured spinal cord in monkeys. *Magn. Reson. Med.* 0, 1–13. doi:10.1002/mrm.25488
- Wolff, S.D., Balaban, R.S., 1989. Magnetization transfer contrast (MTC) and tissue water proton relaxation in vivo. *Magn. Reson. Med.* 10, 135–144. doi:10.1002/mrm.1910100113
- Xing, D., Yeh, C.-I., Shapley, R.M., 2009. Spatial Spread of the Local Field Potential and its Laminar Variation in Visual Cortex. *J. Neurosci.* 29, 11540–11549. doi:10.1523/JNEUROSCI.2573-09.2009
- Yang, P.-F., Wang, F., Chen, L.M., 2015. Differential fMRI Activation Patterns to Noxious Heat and Tactile Stimuli in the Primate Spinal Cord. *J. Neurosci.* 35, 10493–10502.

doi:10.1523/JNEUROSCI.0583-15.2015

Yoshizawa, T., Nose, T., Moore, G.J., Sillerud, L.O., 1996. Functional magnetic resonance imaging of motor activation in the human cervical spinal cord. *Neuroimage* 4, 174–182.

doi:10.1006/nimg.1996.0068

Zhao, F., Williams, M., Meng, X., Welsh, D.C., Grachev, I.D., Hargreaves, R., Williams, D.S., 2009. Pain fMRI in rat cervical spinal cord: An echo planar imaging evaluation of sensitivity of BOLD and blood volume-weighted fMRI. *Neuroimage* 44, 349–362.

doi:10.1016/j.neuroimage.2008.09.001

## **Chapter 2: VALIDATION OF SPINAL CORD fMRI WITH LFP AND SPIKE ACTIVITY IN NON-HUMAN PRIMATES**

### **2.1. Abstract**

Resting-state functional magnetic resonance imaging (rsfMRI) assessments of functional connectivity (FC) based on correlations between BOLD signals have provided a powerful approach to delineating functional circuits and intrinsic architecture in the brain. We have recently identified rsfMRI correlations between gray matter horns in the spinal cord of animals and humans. However, whether rsfMRI is capable of characterizing the intrinsic functional architecture of spinal cord gray matter and its relationship with underlying neural activity remains unknown. The current study aims to characterize the local correlation profile of rsfMRI signals along the dorsal, intermediate and ventral axis and validate the interpretation of rsfMRI correlations as indicators of functional connectivity within neural circuits by directly comparing fMRI measures with corresponding recordings of spiking activity and LFPs. We studied two spinal segments using four linear microelectrode-arrays whose penetration sites were later verified with histology. We found (1) both BOLD and electrophysiological signals elicited by tactile stimulation of a single distal pad occurred predominantly in the ipsilateral dorsal horn and in digit-appropriate segments; (2) the local rsFC of the dorsal horn seed exhibited a U-shaped profile along the dorsal-intermediate-ventral axis; (3) dorsal-dorsal rsFC is significantly greater than that of dorsal-to-intermediate-gray-matter in both modalities; and (4) rsFC is strongest within its own segment. Overall, results demonstrated that there is an intrinsic functional architecture within gray matter of a single spinal segment, and rsfMRI signals acquired at high field directly reflect underlying spontaneous neuronal activity at rest and spinal regions engaged in the same function exhibit strong rsFC. As in the brain, rsfMRI is a powerful tool to delineate spinal cord functional organization and architecture.

### **2.2. Introduction**

The identification of patterns of highly correlated low frequency fMRI signals in the brain in a resting state has provided a powerful approach to delineating functional architecture and neural circuits noninvasively (Bharat Biswal et al., 1995; Deco et al., 2011; Fox and Raichle, 2007;

Greicius et al., 2003; Guye et al., 2008). Altered resting-state functional connectivity under different pathological conditions suggests that these correlations may be reflective of intrinsic neural processes and are fundamental to the maintenance of normal brain functions (Michael D Fox and Greicius, 2010). Over the past two decades, there have been thousands of reports of rsfMRI studies of the brain but only recently has there been an emergence of similar studies in gray matter of the spinal cord (Barry et al., 2016, 2014; Chen et al., 2015; Eippert et al., 2017; Liu et al., 2016; San Emeterio Nateras et al., 2016; Shreyas Harita and Stroman, 2017; Wei et al., 2010; Wu et al., 2017). This could be attributed to difficulties that arise in imaging the spinal cord – a small physical size, pronounced physiological noise, and increased effects from susceptibility gradients (Eippert et al., 2016a). Recent technical advances have allowed robust detection of strong resting state functional connectivity (rsFC) between spinal horns in animal models as well as human subjects (Barry et al., 2016, 2014; Chen et al., 2015; Conrad et al., 2018; Eippert et al., 2017; Kong et al., 2014; San Emeterio Nateras et al., 2016; Wu et al., 2017). These observations led us to hypothesize that, like the brain, spinal cord gray matter likely forms its own intrinsic functional architecture that serves as a fundamental framework for executing and maintaining sensory, motor and autonomic functions. Moreover, given the complex neurovascular coupling of BOLD fMRI signals, validation of their relevance by comparisons to direct measurements of neural activity is still critical to allow more precise interpretations of BOLD fMRI findings within the spinal cord.

Previous studies have demonstrated a direct link between neural activity and BOLD signals in regions of the brain (Leopold and Maier, 2012; Logothetis, 2003; Logothetis et al., 2001; Mukamel, 2005; Shi et al., 2017; Wilson et al., 2016) in stimulation and/or task conditions. However, direct comparisons of spontaneous electrophysiological activity and rsfMRI signals remain relatively unexplored in the brain (Huttunen et al., 2008; Scholvinck et al., 2010; Shi et al., 2017; Wilson et al., 2016), and even less is known at the spinal cord. In the rat spinal cord, previous studies have described stimulus- or movement-induced electrophysiological activities (Inácio et al., 2016; Song and Martin, 2016), yet no study has directly compared and related rsfMRI signal to spontaneous neural activity within the spinal gray matter. The current study aims to address three remaining key questions: what is the intrinsic functional organization feature of spinal gray matter, what is the relationship between changes in stimulus-evoked fMRI signal and neuron population activity (local field potentials (LFPs) and multi-unit activity (MUA)), and whether correlated

rsfMRI signal fluctuations (indicator of resting state functional connectivity) are reflective of underlying synchronous variations in spontaneous neuronal electrophysiological activity within spinal gray matter from the same regions.

In this study, we combined measurements of LFPs and MUA in non-human primates (NHPs) to validate findings from stimulus-driven and resting-state fMRI signal changes. Strong agreement was found in the spatial patterns of neural activities and correlations between the two modalities: tactile stimulation evoked activations at ipsilateral horns in both fMRI and electrical recordings, while resting-state correlations between regions showed parallel relationships. This study identifies an intrinsic functional architecture of dorsal-intermediate-ventral areas and sheds light on the interpretation of rsfMRI studies of the spinal cord, and provides a foundation for assessing and monitoring functional circuitry alterations under spinal cord pathologies using rsfMRI.

## **2.3. Methods**

### **2.3.1. Animal Preparation**

Twelve adult male squirrel monkeys (*Saimiri boliviensis*) were included in this study. Four animals (SM-Ara, SM-Leg, SM-Gua, and SM-Bus) underwent laminectomy and subsequent electrophysiological recordings (Figure 12). For both MRI and electrophysiological experiments, animals were first sedated with ketamine hydrochloride (10 mg/kg)/atropine sulfate (0.05 mg/kg, i.m.) and maintained with isoflurane anesthesia (0.5–1.2%) delivered in a 70:30 N<sub>2</sub>O/O<sub>2</sub> mixture. After intubation, animals were mechanically ventilated, monitored and infused intravenously with 2.5% dextrose in saline solution (2-3 ml/hr/kg) in order to prevent dehydration. Animals' vital signals include peripheral oxygen saturation and heart rate, EKG, end-tidal CO<sub>2</sub>, and respiratory pattern, which were continuously monitored. With a circulating water blanket, temperatures of the animals were also kept between 37.5 and 38.5°C. Animals were subsequently placed in a custom-designed MR cradle and onto a stereotaxic frame for MRI and electrophysiological experiments respectively. Extra care and effort were put into ensuring the animal's neck was secured and straight while ear bars were also used to minimize further motions. While the isoflurane level fluctuates over a range depending on each animal's physiological condition, anesthesia level was

generally maintained at 0.7-0.8% isoflurane level during functional data acquisition. All animal procedures were in compliance and approved by the Institutional Animal Care and Use Committee at Vanderbilt University.

### **2.3.2. MRI Data Acquisition and Analysis**

MRI acquisitions were obtained on a 9.4T Varian magnet with a saddle-shaped transmit-receive surface coil positioned over the neck. High resolution anatomic axial images were obtained using magnetization transfer contrast (TR/TE=220/3.24ms,  $0.25 \times 0.25 \times 3 \text{mm}^3$ ) while BOLD images were acquired using a fast gradient echo sequence (TR/TE=46.9/6.50ms,  $0.5 \times 0.5 \times 3 \text{mm}^3$ , ~3s/volume). Resting-state (300 volumes) and stimulus-driven (8Hz innocuous tactile, 30s on/off, 7 epochs) acquisitions were both obtained. Previously acquired spinal fMRI datasets with a higher temporal resolution (TR=24.0ms, ~1.5s/volume) on healthy monkeys were included in group analyses (Chen et al., 2015; Yang et al., 2015). Data pre-processing and ROI analysis procedures of spinal data were standard, similar to our previous publications (Chen et al., 2015; Yang et al., 2015). Specifically, fMRI images were first pre-processed with 2D rigid body motion correction based on maximization of mutual information with three motion parameters estimated (two translations and one rotation) slice-by-slice. BOLD images were then up-sampled to  $0.25 \times 0.25 \times 3 \text{mm}^3$ , resolution of anatomical volume, with linear interpolation. Manual alignment was then performed between fMRI images and corresponding magnetization transfer contrast (MTC) structural images. This step was performed for each slice and for all the runs in each animal. For each slice, “nuisance” signals derived from muscle and cerebrospinal fluid voxels using principal component analysis. The first three to five signal components that accounted for at least 70% of the cumulative signal variance along with motion correction parameters were used as signal regressors in the general linear model to mitigate their contributions to the BOLD time series. fMRI time series were then bandpass filtered (pass-band between 0.01 and 0.1Hz) using a Chebyshev Type II filter; frequencies above 0.1Hz and below 0.01Hz were filtered out. Runs with gray matter temporal signal-to-noise ratio (tSNR) less than 50 were removed from the study. In order to eliminate possible partial volume effects due to smoothing introduced by linear interpolation from functional to anatomical resolution, a cluster threshold of 2 was applied to prevent any spurious single voxel correlations. Spinal cord masks, excluding voxels outside GM and WM, were also applied. Finally, ROIs were carefully defined before ROI-based analysis.

### **2.3.3. Electrophysiological Mapping and Recording**

For each animal, fMRI activation maps were used as guidance for microelectrode penetrations placed in the exposed spinal cord. Specifically, single epoxy-coated tungsten microelectrodes ( $\sim 1\text{M}\Omega$  impedance) with standard exposed sharp tip ( $< 3\mu\text{m}$ ) were used for mapping the spinal cord. Penetration depths of each microelectrode were recorded and performed at  $300\mu\text{m}$  increments. At each interval, hand digits of the animals were tapped lightly while receptive field of neurons were characterized. Magnitudes of responses were also recorded on a six-level scale (no, very weak, good, very good or excellent response) based on listening to an audio amplifier of spike activity and the viewing of action potentials traces. Segments of the spinal cord were then identified based on known receptive field properties as well as somatotopic organization of digits. Based on the digit maps, four linear microelectrode-arrays (Microprobes Blackrock, 16 channels,  $150\mu\text{m}$  separation between contacts) covering various depths were carefully inserted into the targeted recording sites (Figure 12A-B). LFP broadband voltage signals and spiking activity timestamps of voltages exceeding a threshold were recorded using a Multi-channel Cerebus Neural Signal Processor system (Black Rock, Millard county, Utah) and against a local reference. For stimulation of each digit, 2-3 trials were obtained using the same 30-second-on-/off-paradigm as MRI with 10 epochs, while resting-state signals were recorded for a duration of 15 minutes.

### **2.3.4. Stimulus-driven LFP and MUA Data Analysis**

LFP signals sampled at 500Hz were notch-filtered at 60Hz and 120Hz before a band-pass filter (pass-band between 1 and 150Hz) was applied. Stimulus-driven LFP data were then separated into stimulus-on and stimulus-off periods, which were identified as 20 seconds before and after onset times respectively. Welch power spectra were subsequently computed (Hamming window apodization, window length=10s, overlap=50ms). The percent power changes between stimulus -on and -off at the first five harmonics of 8Hz were calculated before normalization to the upper-bound (standard error of mean) of the greatest signal. LFP and spike activity events were analyzed for all four and two monkeys (SM-Ara and SM-Bus) respectively. Spike activity data recorded from two monkeys were excluded in the group analysis because our initial electrophysiology experiments were optimized for collecting LFP responses. For example, thresholds set for spike event recordings were too high and were not ideal, resulting in minimal

spike events being recorded in the initial experiments. Spike rate histograms (bin size=1s) and peri-event rasters (bin size=0.005s) were computed using NeuroExplorer software. At the group level, time series at channels with the greatest LFP responses were averaged across animals, runs and epochs, and the root-mean-square (r.m.s.) value was computed in successive 0.25s windows, while averaged spike rate histograms (bin size=1s) were also calculated similarly. These plots were converted to percentage signal changes relative to their respective pre-stimulus baseline signals and subsequently overlaid on the extracted fMRI BOLD activation time course.

### **2.3.5. Stimulus Presentation Protocol**

In order to ensure a stable contact between the probe and the animals' fingers, small pegs were glued to the fingernails of the hand which were firmly imbedded into plasticine. This setup leaves the glabrous surfaces of each digit exposed for innocuous vibrotactile stimulation by a 2-mm-diameter rounded plastic probe that is attached to a piezoelectric device driven by a Grass S48 square wave stimulator. During no-stimulation windows, the probe was in light contact with each digit. For fMRI experiments, tactile indentations (0.34mm vertical displacement) of the probe were presented 30 seconds on/off (one epoch) at 8Hz with a pulse duration of 20ms. Seven epochs in total were typically presented within one imaging fMRI run. The same tactile stimulus protocol was used for electrophysiological recordings with ten epochs. Multiple runs (2-3 runs) are collected for each digit stimulation with stimulus-on and -off timestamps recorded.

### **2.3.6. Resting-state LFP Data Analysis**

Resting-state LFPs were further de-noised by notch-filtering the first five harmonics of the respiration frequency. Dorsal seeds at each shank of the electrode that were responsive to tactile stimulation were identified as channels with the greatest LFP responses. Recordings from electrodes 2 and 4 of SM-Bus were also excluded due to prevalent contamination from respiratory and cardiac motion. Intermediate gray matter, which serves as a reference tissue, was subsequently identified as the channel closest to 1mm away from the dorsal seed on the same shank. This measurement was made based on corresponding high resolution MRI axial images. Resting-state coherences were then computed between dorsal horns within and across segments and used to indicate the functional connectivity between neuron populations recorded. Dorsal to intermediate gray matter coherences were also measured within each segment. Similarly, functional

connectivity with the contralateral side of the spinal cord was computed using coherences away from the dorsal seeds on each shank. Because penetration depths of each monkey are slightly different, boxplots corresponding to distances away from the dorsal horn that contained runs from only one monkey are not considered for group analysis.

### **2.3.7. ROI-selection of Intermediate GM**

ROI voxels of the intermediate GM control regions were selected based on both anatomical features and functional patterns relative to the ipsilateral dorsal horn. Specifically, small ROIs (2-5 voxels wide x 1 voxel deep) were drawn from dorsal to ventral horn on one side of the spinal cord (see Figure 16A). The dorsal horn (red voxels) was subsequently selected as the seed before mean correlations between resting-state time series were computed for all the ROIs as a function of depth (green). The correlations demonstrated a U-shaped pattern in which correlation strengths decreased monotonically from a high value to a low value as we approached the intermediate region, and then increased as the ventral region was approached (Figure 16B). We then functionally and anatomically defined the most appropriate intermediate GM seeds as the voxels in the layer with the greatest correlation difference from the dorsal seed (typically 4-5 voxels deeper). Given the unclear anatomic boundaries of the intermediate GM region, we believe this allows a more precise identification of a control intermediate region. Our results here also show that the method of defining intermediate-GM region through anatomical features alone in our fMRI acquisition may have encompassed a region contaminated by functional features of the dorsal or ventral horn and thereby missed the most appropriate location of our targeted control region. For runs without the observed profile, the intermediate GM region was defined using results from the same session. Otherwise, they were identified anatomically as voxels at the same depth as the central canal of the spinal cord. This was repeated for all runs for both left and right sides of the spinal cord. This pattern was supported at the group level with aligned correlation profiles at the defined intermediate-GM ROI shown in Figure 16C.

### **2.3.8. ROI-based and statistical analyses**

An ROI-based correlation analysis was used to assess functional connectivity between different ROIs. This method was selected, as were in our previous spinal studies (Barry et al., 2015, 2014; Chen et al., 2015; Wu et al., 2017), because ROIs drawn could be based on hypotheses

derived from stimulus-driven data as well as previous fMRI studies in humans and animals. Dorsal ROIs were manually selected (2-3 voxels) using aligned high-resolution MTC images with high contrast-to-noise-ratio between white and gray matter butterfly. This was done for both the left and right side of the spinal cord for each monkey. Pearson's correlation coefficients were subsequently computed between different ROI pairs of interest. Our quantitative horn-horn connectivity measurements were similar to what was described in our previous publications (Barry et al., 2015, 2014; Chen et al., 2015; Wu et al., 2017). Briefly, mean time series of  $m$  individual voxel time series of a horn were correlated with  $n$  time series of another horn. Subsequently, the average of this correlation vector was selected as the metric of functional connectivity between the pair of horns. This was performed for different pairs of ROIs of interest within (middle slice, slice 3 of Figure 13) and across slices (slices 2, 3 and 4 of Figure 13). Statistical tests of significance were performed between boxplots of correlation values using non-parametric two-sided Mann Whitney Wilcoxon test. Bonferroni-Holm correction was performed and  $p < 0.05$  was considered to be statistically significant.

### **2.3.9. Histology**

At the conclusion of terminal invasive electrophysiological recording sessions, animals were given a lethal dose of anesthetic (sodium pentobarbital) before being perfused transcardially with phosphate buffered 0.9% saline, then 2-4% paraformaldehyde in phosphate buffer and lastly 10% sucrose in phosphate buffer. For one of the monkeys (SM-Gua), an electrolytic lesion was made by passing a current (10  $\mu$ A) via an electrode in one of the recording sites in the spinal cord (Figure 12C). This lesion was made to further confirm our sampling region of the spinal cord. The spinal cord was subsequently extracted before sections of the spinal cord were stained for cytochrome oxidase to locate electrode penetration.

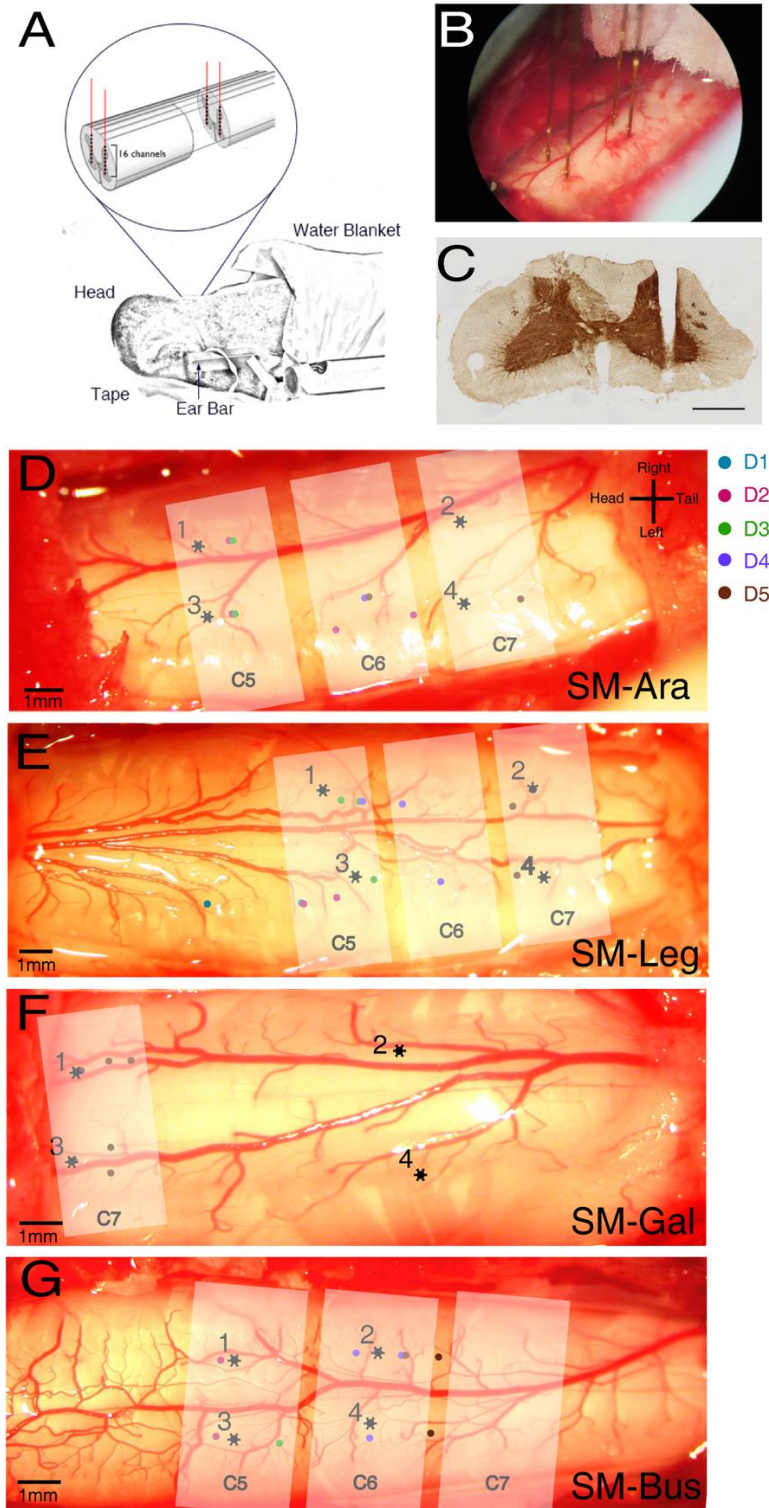


**Figure 12: Electrophysiological recording sites for the four SMs.** (A) Schematic diagram of the spinal cord inserted with four electrodes, each with 16 channels that are  $150\mu\text{m}$  apart. (B) Sample photograph of the four inserted electrodes in SM-Ara. (C) Cytochrome oxidase stain used to verify electrode penetrations of the spinal cord by identifying the electrolytic lesion. Exposed spinal cord with mapped digit regions (color dots) and recording sites (black asterisks) for (D) SM-Ara, (E) SM-Lego, (F) SM-Gua and (G) SM-Bus. Shaded white regions are estimated segments of the spinal cord.

## 2.4. Results

### 2.4.1. Comparable tactile stimulus evoked responses between fMRI and electrophysiology (LFP and spike activity)

To understand the relationship between spinal fMRI signal and neural electrophysiological activity during the processing of innocuous tactile inputs, we recorded and compared the temporal variations of fMRI and electrophysiological signals during the presentation of 8Hz vibration stimulation of a single distal pad. Figure 13E illustrates the quality of our sub-millimeter fMRI acquisitions and Figure 13G shows an example of averaged fMRI tactile activation map from one monkey obtained at 9.4T. Figure 13F shows that 8-Hz innocuous tactile stimulation of a single digit elicited strongest BOLD signal changes on the ipsilateral dorsal horn, with a peak value of  $0.76 \pm 0.06\%$ . Figure 14 shows representative stimulus-driven LFP and multi-unit spike activity recorded from the ipsilateral horn that receives inputs from the stimulated digits which demonstrate strong responses to stimulation. LFP voltage changes followed the stimulus paradigm (yellow shades in Figures 14B, E) and frequency peaks are apparent at harmonics of 8Hz in the power spectra (Figures 14C, F). This observation was consistent among all four monkeys that underwent electrophysiology. Group normalized LFP power changes showed digit-selective response to the tactile stimulus (compare four different color curves in Figure 14A, D). Similarly, in line with the LFP observation, spike rate histograms as well as peri-event raster plots of spike density in the ipsilateral horn also showed the largest responses to the single digit stimulated (Figure 14H, K). Group normalized spike rates obtained from four different recording sites (left D3, right D3, left D5, and right D5) are presented in Figures 14G, J. Figure 15 presents group averaged BOLD signal time courses and neural signal (LFP and MUA) responses to tactile stimulation overlaid on the same plot. Overall, significant and correlated changes in all three measures were observed in the ipsilateral dorsal horn of the homeotropically appropriate cervical segment, a finding that is congruent with fMRI results here and in previously reported studies (Stroman, 2005; Yang et al., 2015).

### 2.4.2. Local spatial resting state correlation profile of the dorsal horn.

Previous studies in NHP spinal cords revealed strong functional connectivity between dorsal-dorsal or dorsal-ventral horns. By taking the advantage of high signal-to-noise ratio (SNR)

and resolution rsfMRI data, we next plotted local correlation profiles of the dorsal horn seed along the dorsal-intermediate-ventral axis. Small ROIs were drawn from the dorsal towards the ventral horn on one side of the spinal cord (Figure 16A). In over half the observations (58% of the runs), we found correlations demonstrated a U-shaped pattern in which correlation strengths decreased monotonically from a high value to a low value at the level of the intermediate gray matter, and then increased as the ventral region was approached (Figure 16B, C and Figure 17). This suggests the existence of three distinct sub-divisions (dorsal, intermediate and ventral), and allowed the intermediate GM seed ROIs to be more confidently defined functionally and anatomically for subsequent comparisons with electrophysiology (see details in *Materials and Methods*). This local correlation profile was supported at the group level after aligning the defined intermediate GM ROI shown in Figure 16C. The tSNR of the voxel examined also did not show systematic changes as a function of distance from the seed (Figure 16D), suggesting the correlation profile trend cannot be driven by varying noise levels across three zones.

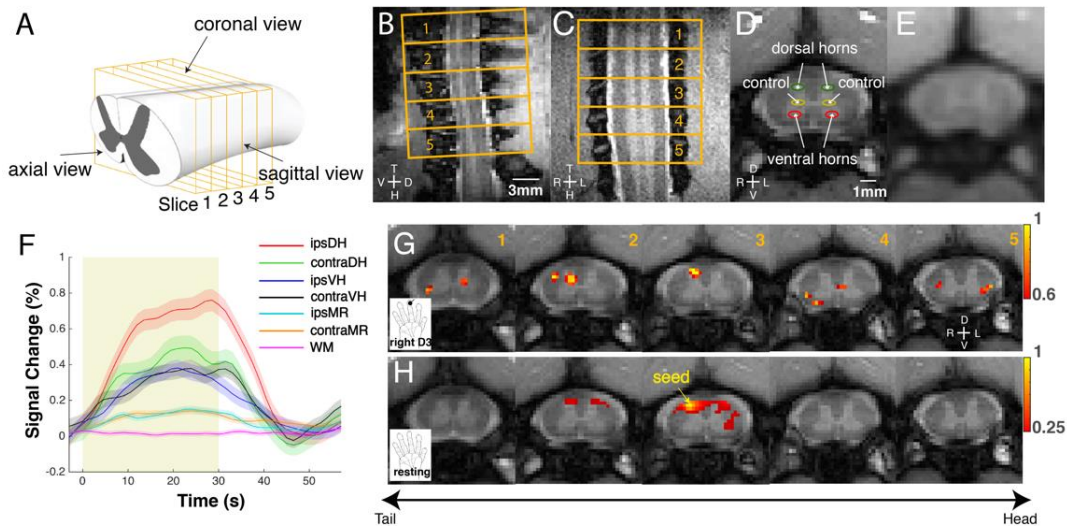


**Figure 13: Stimulus-driven and resting-state fMRI in non-human primates at 9.4T.** (A) Schematic diagram (modified from (Hollis et al., 2016)) of imaging planes of the spinal cord. (B) Sagittal and (C) coronal views of the spinal cord in magnetization transfer contrast (MTC) images. (D) MTC and (E) BOLD sensitive axial images. Red and green circles indicate dorsal and ventral horns respectively. Yellow circles present intermediate gray matter of the spinal cord used as controls for later quantifications. (F) Group averaged ( $N=7$  monkeys) BOLD signal changes in the four horns – dorsal horn (DH) and ventral horn (VH) – of the spinal cord and middle/intermediate gray matter regions (MR) that are ipsilateral (ipsi) and contralateral (contra) to the stimulus, as well as white matter (WM) control region. (G) Multi-run activation map to D3 tactile stimulation thresholded at 0.6 of normalized percentage signal, with a peak value of 1. (H) Multi-run resting-state connectivity patterns (thresholded at  $r > 0.25$ ) of seed from one representative monkey. D, dorsal; V, ventral; H, head; T, tail.

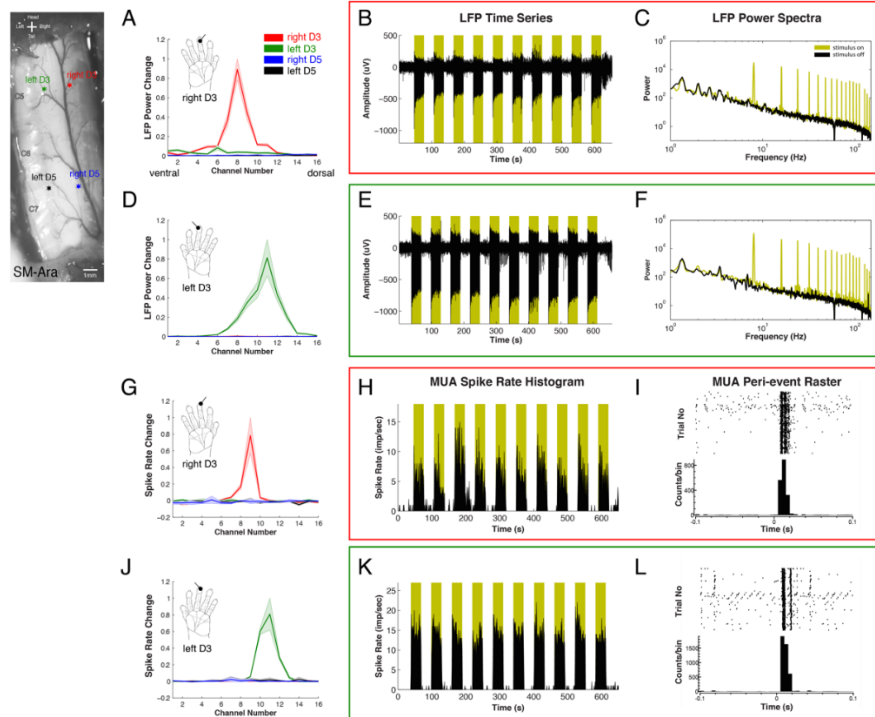


**Figure 14: Stimulus-driven LFP and spike activity responses.** (A,D) Normalized averaged ( $n=3$  runs) LFP power changes computed from Welch's power spectra, and (G, J) normalized spike rate ( $n=3$  runs) changes between 30s stimulus-on and -off in all four electrodes under right-D3 and left-D3 innocuous 8Hz tactile stimulus conditions respectively. Shaded error bars represent standard-error of mean. (B,E) LFP time series from the channel that presents the greatest power change and its respective (C,F) Welch's power spectra. Dark yellow shaded regions and plots represent stimulus-on periods. (H,K) Spike rate histograms at the channels corresponding to largest changes and their corresponding (I,L) raster plots (top row) and peri-event histograms (bottom row). Spike activity was processed for only two of the four monkeys: squirrel monkeys (SM)-Ara and SM-Bus.

### 2.4.3. Validation of resting-state fMRI functional connectivity of the spinal horns

Inter-horn resting-state connectivity patterns observed in rsfMRI were compared to LFP connectivity pattern (broadband coherences). Specifically, connectivity measures between different pairs of ROIs were compared: dorsal-dorsal (within-slice), dorsal-intermediate gray matter and dorsal-dorsal (across-slice) (Figure 18A). At the group level ( $N=12$  and 4 monkeys for fMRI and LFP respectively), within-slice dorsal-dorsal functional connectivity was observed to be stronger (mean BOLD  $r=0.49$  and LFP coherence= $0.19$ ) than that in dorsal-intermediate gray matter (averaged mean between left and right BOLD  $r=0.40$  and LFP coherence= $0.12$ ) for both fMRI and LFP (Figures 18B-C). Moreover, LFP dorsal-dorsal coherence was found to be statistically significant at depths (from dorsal surface) up to 1.5 mm for correlations of contralateral regions at precisely the same depth (Figure 19). While within-slice resting-state connectivity was robust between horns, across-slice correlation strengths were found to be consistently lower (mean

BOLD  $r=0.26$  and LFP coherence= $0.04$ ). Trends of connectivity measures in different ROI pairs (Figure 18B-C) were also highly similar between the two modalities ( $r=0.9982$ ,  $p<0.05$ ) while Bonferroni-Holm corrected Mann-Whitney tests between different ROI selections support this observation.

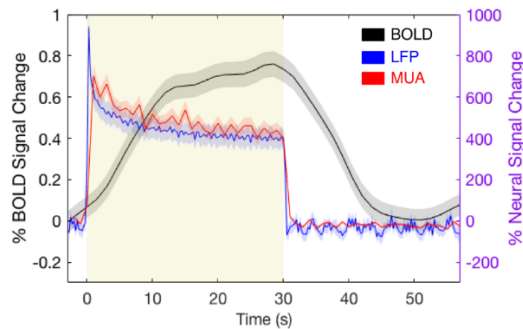


**Figure 15: Responses to innocuous tactile stimulation of digits in the spinal cord.** Overlay of averaged time courses of fMRI (black), LFP (blue) and MUA (red) responses in the ipsilateral dorsal horn. Shaded yellow region represents stimulus-on period. LFP signals are represented with computed r.m.s. (bin size= $0.25s$ , no overlap,  $N=4$  monkeys,  $n=40$  runs) while MUA are presented as spike rates (bin size= $1s$ , no overlap,  $N=2$  monkeys,  $n=24$  runs). Percentage signal changes for BOLD and neural signal were computed relative to pre-stimulus period; BOLD and electrophysiological signals are plotted against y-scale on the left (black) and right (purple) respectively. It is also important note that signals from the two modalities were not acquired simultaneously.

## 2.5. Discussion and conclusions

### 2.5.1. Agreement of electrophysiology findings with spinal rsfMRI studies

We found in this study that within-slice (representing one spinal segment) dorsal-dorsal horn resting-state functional connectivity is significantly greater than values for dorsal horn to control regions, identified here as intermediate gray matter regions of the cord, for both fMRI and LFP. Quantitative comparisons of connectivity trends between the two modalities revealed that they are highly similar. Previous spinal rsfMRI studies from other groups have also reported the existence of strongly correlated bilateral sensory networks in anesthetized rodents and NHPs (Chen et al., 2015; Wu et al., 2017), and awake humans. In humans, an early report used independent component analysis, a data-driven approach, to separate the spinal cord into dorsal and ventral networks (Kong et al., 2014). We used an ROI-based technique that showed robust BOLD correlations between dorsal-dorsal and ventral-ventral horns, with no significant group-level correlations between gray and white matter regions (Barry et al., 2014). The reproducibility

of these findings was further quantified and confirmed (Barry et al., 2016; Eippert et al., 2017) while more recent studies have explored the variable patterns of the functional network (Liu et al., 2016) and the influences of physiological noise on measurements of functional connectivity (Shreyas Harita and Stroman, 2017). In animal studies performed at 9.4T, similar conclusions were obtained: strong dorsal-dorsal and ventral-ventral connections were found compared to control white matter regions (Chen et al., 2015; Wu et al., 2017). Given the complex neurovascular coupling involved in producing BOLD contrast, the biophysical basis of these findings remains unclear in the spinal cord. Moreover, whether correlated fMRI signals between spinal ROIs reflect similar neural processes as cortical ROIs also remain largely unknown. Our results here using electrophysiological measures help fill this knowledge gap, although our findings focused only on the relationships of BOLD and LFPs in the sensory dorsal horns. Overall, our findings demonstrate rsfMRI can be a reliable surrogate biomarker for evaluating neural circuits in the spinal cord, and the strength of BOLD correlations reflects neural functional connectivity as indicated by spontaneous LFP signals.

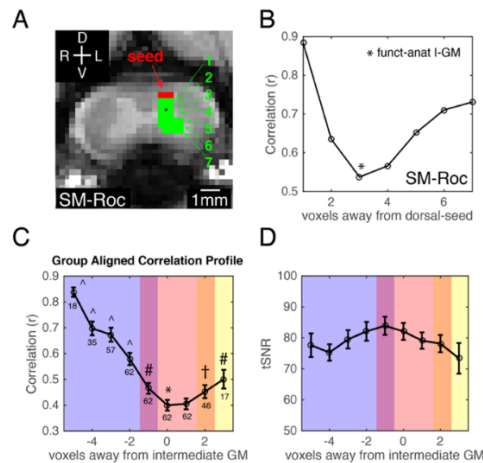


**Figure 16: Local dorsal to ventral correlation profile.** (A) ROIs defined in one representative monkey on one side of the spinal cord. Mean time series of the dorsal region (red voxels) was used as seed to compute mean Pearson's cross correlations with voxels from each layer (green voxels); layer numbers are indicated by the green numbers. (B) An example of an observed U-shaped profile from SM-Roc. Asterisk (\*) represents defined intermediate GM (I-GM) seeds based on functional and anatomical features; greatest difference of connectivity value to the dorsal horn seed. (C) Group averaged aligned correlation profile based on each run's anatomically-functionally defined seed of the intermediate GM region for both left and right sides of the spinal cord. Error bars represent standard error of mean. The number of observations for each distance are indicated below each scatter circle. Blue, red and yellow shades represent estimated dorsal, intermediate and ventral boundaries defined based on statistical comparisons relative to the defined I-GM seed; #,  $p < 0.05$ ; †,  $p < 0.1$ . Shades of overlaid colors - purple and orange - represent estimated overlap of dorsal-IGM and ventral-IGM respectively. (D) Group averaged tSNR at different layers of the spinal cord used to compute (C).

### 2.5.2. Functional connectivity across segments

Communications between spinal segments is critical for execution of spinal cord functions, but inter-segment (cross-slice) resting-state connectivity has been little studied. In humans, Kong et al. reported no correlations between resting-state signals between different segmental levels using an independent components analysis (Kong et al., 2014). More recently, Liu et al. showed significant functional connectivity across slices and vertebral levels, although most of them were located within one segment distance (Liu et al., 2016). In our previous investigations in NHPs, we also found strong functional connectivity between the same horn (e.g., dorsal-to-dorsal) on two adjacent segments, with resting-state correlation values decreasing from  $\sim r=0.85$  to  $\sim r=0.4$  and  $\sim r=0.3$  when moving one and two slices away respectively (Chen et al., 2015). A similar phenomenon was observed in rodents where connectivity decreased significantly as distances along the spine between ROIs increased (Wu et al., 2017). With direct neuronal recordings, we aimed to answer the question of whether this observation is an effect of pre-processing steps applied on a slice-by-slice basis or because correlations truly decrease with increasing distance along the cord. Our rsfMRI and electrophysiology results indicate the latter. The diminished tactile responses two segments away from the stimulated digit's receptive field further support this idea. The segmental organization of the spinal cord permits somatotopic encoding of peripheral information, and perhaps intrinsic circuits are also organized in such a fashion. As expected, LFP measurements showed greater statistical differences between across- and within-slice connectivity ( $p < 0.00005$  Bonferroni-Holm corrected Mann-Whitney Test), and parallel those from fMRI.

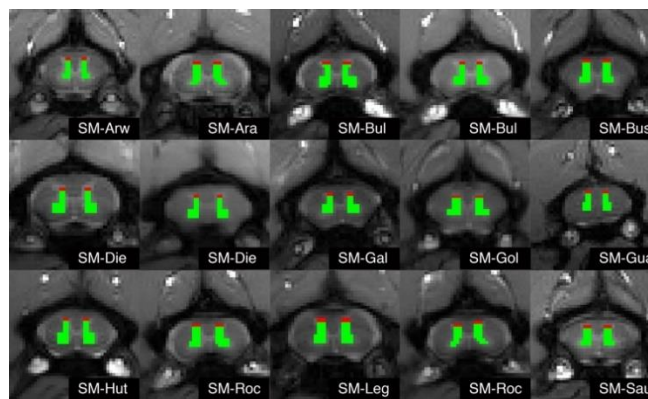


**Figure 17: ROI selections for each individual monkey.** ROIs drawn for each monkey to generate correlation values in Figure 16. A total of 15 imaging sessions were used to scan 12 animals, and hence repeated monkey labels are shown. Red and green voxels represent dorsal seed regions and different layer voxels respectively.

### **2.5.3. Stimulus-evoked activations and their functional relevance**

Logothetis et al. have shown with simultaneous recordings of BOLD and neural signals in the visual cortex that a spatially localized increase in BOLD contrast corresponds to a direct increase in neural activity. In addition, LFP responses were observed to be statistically greater and more maintained throughout a stimulus than MUA (Logothetis et al., 2001). Our stimulus-driven results unequivocally showed increased fMRI responses correspond to increased neural electrophysiological activity. Direct neural recordings consistently showed greater SNRs than fMRI. Robust LFP responses were observed in all four monkeys. Moreover, MUA and LFP responses were both maintained throughout the 30-sec stimulus duration, an observation similar to our observations in cortical area 3b of squirrel monkey (Wang et al., 2013b). One step further, our observations within the spinal cord again support the notion that regions which are engaged collectively in the same function, such as processing an external stimulus (e.g., tactile input), often demonstrate strong resting state functional connectivity between them (Chen et al., 2015; Cohen and Kohn, 2011; M D Fox and Greicius, 2010; Vincent et al., 2007; Wang et al., 2013a). For example, in the SI cortex, sub-regions representing single distal finger pads demonstrated high resting-state connectivity with synchronized unit electrophysiological activity and anatomical connections (Wang et al., 2013a). Similarly, dorsal horns of the spinal cord have been shown to be most responsive to either pain or tactile stimulations (Malisza and Stroman, 2002; Yang et al., 2015; Zhao et al., 2009a), as further verified with both fMRI and electrophysiology in this study. Using electrode positions that responded most robustly to tactile stimulation as seeds, these channels indeed demonstrated stronger connectivity patterns with each other compared to others. Overall, the notion that baseline functional connectivity is an organizational feature of the central nervous system is extended and verified in the spinal cord, with guidance of stimulus-evoked activation foci. The observation that regions working together in tasks exhibit strong functional connectivity at rest appears to be a universal organizational principle within the central nervous system.

### **2.5.4. Spinal cord of non-human primates**

While spinal electrophysiology has previously been performed in other animal models, the functional architecture and neural circuits of the central nervous system in NHPs share much greater similarities with those in humans. Previous reports have made use of NHPs to compare and

understand the underlying biophysical basis of BOLD signals, but these were restricted to different cortices of the brain (Chen et al., 2017a). In this study, we have used NHPs to perform direct validation of MRI findings in the spinal cord using multi-channel microelectrodes. That being said, some rsfMRI spinal connectivity differences between NHPs and humans in previously published reports are also present. In humans, within hemi-cord dorsal-ventral connectivity remains speculative due to weaker correlations compared to bilateral dorsal and ventral horn connectivity (Barry et al., 2016; Conrad et al., 2018; Eippert et al., 2017), although unilateral resting-state dorsal components have also been identified using independent component analysis (Kong et al., 2014). In NHPs, however, ipsilateral dorsal-ventral connectivity appears to be significant when compared to controls (Chen et al., 2015), and this could be attributed to differences in the functional organization of the spine between species if there is a greater use of coordinated bilateral behaviors in animals. Despite some differences present, the study of NHPs remains to be a crucial linkage between invasive animal data and human studies in the literature (Hutchison and Everling, 2012; Vincent et al., 2007).

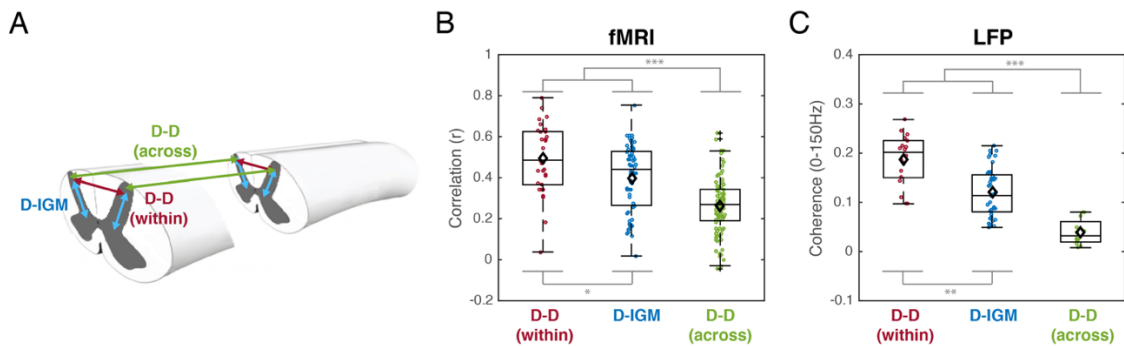


**Figure 18: Comparison between resting-state fMRI and LFP connectivities.** (A) Schematic diagram of correlation and coherences computed in the recordings of the spinal cord. (B,C) Group averaged within and across segments dorsal to dorsal (D-D) as well as dorsal to intermediate GM (D-IGM) connectivity was computed. Group boxplots of connectivity measures are displayed as Pearson's correlation for fMRI and averaged coherences for LFP. Each boxplot contains fMRI observations from 15 functional studies and electrophysiology observations from four monkeys in panels B and C respectively. Ipsilateral dorsal-to-intermediate GM from left and right hemi-cord were concatenated. The median and mean of are represented as horizontal lines and diamonds respectively in each boxplot. Scatter circles on each boxplot represent individual observations. \* $p < 0.05$ , \*\* $p < 0.0005$ , and \*\*\* $p < 0.00005$  Bonferroni-Holm corrected two-sided Mann-Whitney Test.

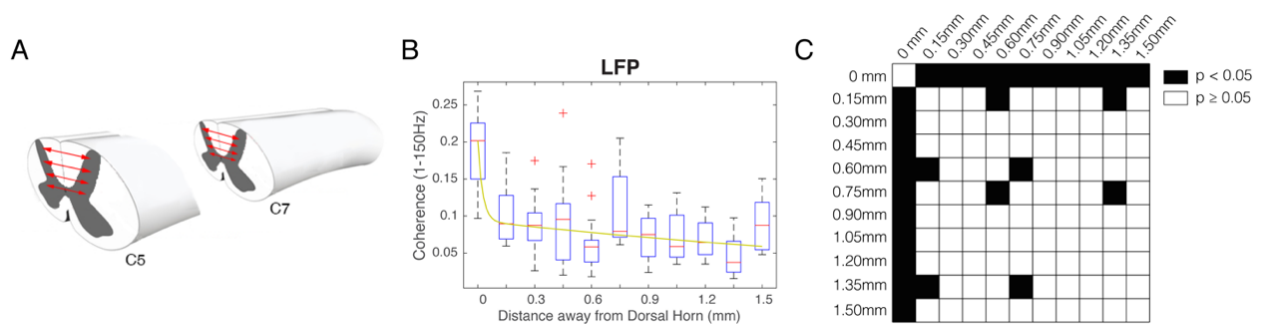


**Figure 19: LFP dorsal-dorsal coherence at various depths.** (A) Schematic diagram of coherences computed in the recordings of the spinal cord. Coherences between contralateral horns as a function of penetration depth were computed along the dorsal horn to the intermediate-gray-matter section. (B) Within-slice connectivity patterns across the spinal cord as a function of laminar depth for LFP. Because penetration depths of each monkey are slightly different, there are 18, 15, 11 and 8 observations for each boxplot between 0-0.60mm, 0.75-1.05mm, 1.20-1.35mm and 1.50mm respectively. (C) Matrix of two-sided Mann-Whitney Tests between different combinations of boxplots on the left. White voxels indicate corrected p-values greater than or equal to 0.05 while black voxels indicate p-values less than 0.05.

### 2.5.5. Challenges of imaging and electrophysiological recordings in the spinal cord and limitations

As described in previous publications (Eippert et al., 2016a), imaging the cervical spinal cord poses several challenges. Using an optimized MRI sequence along with modified image processing steps (Chen et al., 2015), we have reduced these confounding effects and developed a sensitive protocol for the detection of resting-state networks in the cervical spinal cord. Electrophysiological recordings of the spinal cord also pose their own challenges. For example, there is a tradeoff between the number of recording sites (four were chosen in our study) and the density of electrode contacts for sampling. In our study, due to the restricted sampling field-of-view, the ventral horns were not fully sampled. Customized electrode configurations are needed to optimize simultaneous recordings.

### 2.5.6. Conclusions

This is the first study, to our knowledge, to validate rsfMRI connectivity measurements in the spinal cord using invasive neuronal recordings. We found under stimulus-driven and resting-state conditions that BOLD signal changes are congruent with electrophysiological signals. These results suggest that rsfMRI signals acquired at high field are capable of reflecting underlying neuronal activity in a resting state and during processing of an external stimulus at the spinal level. The confirmation that resting-state functional connectivity measured with rsfMRI signals can be

reliably used as a biomarker of neural connectivity is especially significant in the context of the need to monitor spinal cord functional recovery along with the need of a reliable intrinsic imaging biomarker of spinal repair.

### **2.5.7. Acknowledgements**

This specific study is supported by NIH grant NS092961 and DOD grant SC160154. The author gratefully acknowledges Fuxue Xin, George Wilson III, Dr. Qing Liu and Chaohui Tang for their assistance with data collection, Dr. Chia-Chi Liao for advice on spinal cord recordings, and Dr. Robert L. Barry, Dr. Baxter Rogers and Benjamin Conrad for their advice on spinal functional data analysis.

## 2.6. References

- Barry, R.L., Rogers, B.P., Smith, S.A., Gore, J.C., 2015. Reproducibility of resting state spinal cord networks at 7 Tesla 23, 3708. doi:10.1016/j.neuroimage.2016.02.058
- Barry, R.L., Smith, S.A., Dula, A.N., Gore, J.C., 2014. Resting state functional connectivity in the human spinal cord. *Elife* 2014, 1–15. doi:10.7554/eLife.02812
- Biswal, B., Zerrin Yetkin, F., Haughton, V.M., Hyde, J.S., 1995. Functional connectivity in the motor cortex of resting human brain using echo-planar mri. *Magn. Reson. Med.* 34, 537–541. doi:10.1002/mrm.1910340409
- Chen, L.M., Mishra, A., Yang, P.-F., Wang, F., Gore, J.C., 2015. Injury alters intrinsic functional connectivity within the primate spinal cord. *Proc. Natl. Acad. Sci. U. S. A.* 112, 5991–6. doi:10.1073/pnas.1424106112
- Chen, L.M., Yang, P.-F., Wang, F., Mishra, A., Shi, Z., Wu, R., Wu, T.-L., Wilson III, G.H., Ding, Z., Gore, J.C., 2017. Biophysical and neural basis of resting state functional connectivity: Evidence from non-human primates. *Magn. Reson. Imaging* 39, 71–81. doi:10.1016/j.mri.2017.01.020
- Cohen, M.R., Kohn, A., 2011. Measuring and interpreting neuronal correlations. *Nat. Neurosci.* 14, 811–819. doi:10.1038/nn.2842
- Conrad, B.N., Barry, R.L., Rogers, B.P., Maki, S., Mishra, A., Thukral, S., Sriram, S., Bhatia, A., Pawate, S., Gore, J.C., Smith, S.A., 2018. Multiple sclerosis lesions affect intrinsic functional connectivity of the spinal cord. *Brain*. doi:10.1093/brain/awy083
- Deco, G., Jirsa, V.K., McIntosh, A.R., 2011. Emerging concepts for the dynamical organization of resting-state activity in the brain. *Nat. Rev. Neurosci.* doi:10.1038/nrn2961
- Eippert, F., Kong, Y., Jenkinson, M., Tracey, I., Brooks, J.C.W., 2016a. Denoising spinal cord fMRI data: Approaches to acquisition and analysis. *Neuroimage*. doi:10.1016/j.neuroimage.2016.09.065
- Eippert, F., Kong, Y., Winkler, A.M., Andersson, J.L., Finsterbusch, J., Buchel, C., Brooks, J.C., Tracey, I., 2016b. Investigating resting-state functional connectivity in the cervical spinal cord at 3T. *bioRxiv* 1–30. doi:10.1101/073569
- Fox, M.D., Greicius, M., 2010. Clinical applications of resting state functional connectivity. *Front Syst Neurosci* 4, 1–13. doi:10.3389/fnsys.2010.00019
- Fox, M.D., Raichle, M.E., 2007. Spontaneous fluctuations in brain activity observed with functional magnetic resonance imaging. *Nat Rev Neurosci* 8, 700–711. doi:nrn2201 [pii]\n10.1038/nrn2201
- Greicius, M.D.M., Krasnow, B., Reiss, A.L., Menon, V., ... A.R.-P. of the, 2003, undefined, Reiss, A.L., Menon, V., 2003. Functional connectivity in the resting brain: a network analysis of the default mode hypothesis. *Natl. Acad. Sci.* 100, 253/258. doi:10.1073/pnas.0135058100
- Guye, M., Bartolomei, F., Ranjeva, J.-P., 2008. Imaging structural and functional connectivity: towards a

- unified definition of human brain organization? *Curr. Opin. Neurol.* 24, 393–403.  
doi:10.1097/WCO.0b013e3283065cfb
- Hollis, E.R., Ishiko, N., Yu, T., Lu, C.-C., Haimovich, A., Tolentino, K., Richman, A., Tury, A., Wang, S.-H., Pessian, M., Jo, E., Kolodkin, A., Zou, Y., 2016. Ryk controls remapping of motor cortex during functional recovery after spinal cord injury. *Nat. Neurosci.* 19, 697–705.  
doi:10.1038/nn.4282
- Hutchison, R.M., Everling, S., 2012. Monkey in the middle: why non-human primates are needed to bridge the gap in resting-state investigations. *Front. Neuroanat.* 6. doi:10.3389/fnana.2012.00029
- Huttunen, J.K., Gröhn, O., Penttonen, M., 2008. Coupling between simultaneously recorded BOLD response and neuronal activity in the rat somatosensory cortex. *Neuroimage* 39, 775–785.  
doi:10.1016/j.neuroimage.2007.06.042
- Inácio, A.R., Nasretidinov, A., Lebedeva, J., Khazipov, R., 2016. Sensory feedback synchronizes motor and sensory neuronal networks in the neonatal rat spinal cord. *Nat. Commun.* 7.  
doi:10.1038/ncomms13060
- Kong, Y., Eippert, F., Beckmann, C.F., Andersson, J., Finsterbusch, J., Buchel, C., Tracey, I., Brooks, J.C., 2014. Intrinsically organized resting state networks in the human spinal cord. *Proc Natl Acad Sci U S A* 111, 18067–18072. doi:10.1073/pnas.1414293111
- Leopold, D.A., Maier, A., 2012. Ongoing physiological processes in the cerebral cortex. *Neuroimage.*  
doi:10.1016/j.neuroimage.2011.10.059
- Liu, X., Zhou, F., Li, X., Qian, W., Cui, J., Zhou, I.Y., Luk, K.D.K., Wu, E.X., Hu, Y., 2016. Organization of the intrinsic functional network in the cervical spinal cord: A resting state functional MRI study. *Neuroscience* 336, 30–38. doi:10.1016/j.neuroscience.2016.08.042
- Logothetis, N.K., 2003. The underpinnings of the BOLD functional magnetic resonance imaging signal. *J. Neurosci.* 23, 3963–3971. doi:23/10/3963 [pii]
- Logothetis, N.K., Pauls, J., Augath, M., Trinath, T., Oeltermann, A., 2001. Neurophysiological investigation of the basis of the fMRI signal. *Nature* 412, 150–7. doi:10.1038/35084005
- Malisza, K.L., Stroman, P.W., 2002. Functional imaging of the rat cervical spinal cord. *J. Magn. Reson. Imaging* 16, 553–558. doi:10.1002/jmri.10185
- Mukamel, R., Gelbard, H., Arieli, A., Hasson, U., Fried, I., Malach, R., 2005. Coupling between neuronal firing, field potentials, and FMRI in human auditory cortex. *Science* 309, 951–954.  
doi:10.1126/science.1110913
- San Emeterio Nateras, O., Yu, F., Muir, E.R., Bazan, C., Franklin, C.G., Li, W., Li, J., Lancaster, J.L., Duong, T.Q., 2016. Intrinsic Resting-State Functional Connectivity in the Human Spinal Cord at 3.0 T. *Radiology* 279, 262–8. doi:10.1148/radiol.2015150768

- Scholvinck, M.L., Maier, A., Ye, F.Q., Duyn, J.H., Leopold, D.A., 2010. Neural basis of global resting-state fMRI activity. *Proc. Natl. Acad. Sci.* 107, 10238–10243. doi:10.1073/pnas.0913110107
- Shi, Z., Wu, R., Yang, P.-F., Wang, F., Wu, T.-L., Mishra, A., Chen, L.M., Gore, J.C., 2017. High spatial correspondence at a columnar level between activation and resting state fMRI signals and local field potentials. *Proc. Natl. Acad. Sci.* 114, 5253–5258. doi:10.1073/pnas.1620520114
- Shreyas Harita, Stroman, P.W., 2017. Confirmation of resting-state BOLD fluctuations in the human brainstem and spinal cord after identification and removal of physiological noise. *Magn. Reson. Med.* doi:10.1002/mrm.26606
- Song, W., Martin, J.H., 2016. Spinal cord direct current stimulation differentially modulates neuronal activity in the dorsal and ventral spinal cord. *J. Neurophysiol.* jn.00584.2016. doi:10.1152/jn.00584.2016
- Stroman, P.W., 2005. Magnetic Resonance Imaging of Neuronal Function in the Spinal Cord: Spinal fMRI. *Clin. Med. Res.* 3, 146–156. doi:10.3121/cmr.3.3.146
- Vincent, J.L., Patel, G.H., Fox, M.D., Snyder, A.Z., Baker, J.T., Van Essen, D.C., Zempel, J.M., Snyder, L.H., Corbetta, M., Raichle, M.E., 2007. Intrinsic functional architecture in the anaesthetized monkey brain. *Nature* 447, 83–86. doi:10.1038/nature05758
- Wang, Z., Chen, L., Négyessy, L., Friedman, R., Mishra, A., Gore, J., Roe, A., 2013a. The Relationship of Anatomical and Functional Connectivity to Resting-State Connectivity in Primate Somatosensory Cortex. *Neuron* 78, 1116–1126. doi:10.1016/j.neuron.2013.04.023
- Wang, Z., Qi, H.X., Kaas, J.H., Roe, A.W., Chen, L.M., 2013b. Functional signature of recovering cortex: Dissociation of local field potentials and spiking activity in somatosensory cortices of spinal cord injured monkeys. *Exp. Neurol.* 249, 132–143. doi:10.1016/j.expneurol.2013.08.013
- Wei, P., Li, J., Gao, F., Ye, D., Zhong, Q., Liu, S., 2010. Resting state networks in human cervical spinal cord observed with fMRI. *Eur J Appl Physiol* 108, 265–271. doi:10.1007/s00421-009-1205-4
- Wilson, G.H., Yang, P.F., Gore, J.C., Chen, L.M., 2016. Correlated inter-regional variations in low frequency local field potentials and resting state BOLD signals within S1 cortex of monkeys. *Hum. Brain Mapp.* 37, 2755–2766. doi:10.1002/hbm.23207
- Wu, T.-L., Wang, F., Mishra, A., Wilson, G.H., Byun, N., Chen, L.M., Gore, J.C., 2017. Resting-state functional connectivity in the rat cervical spinal cord at 9.4 T. *Magn. Reson. Med.* doi:10.1002/mrm.26905
- Yang, P.-F., Wang, F., Chen, L.M., 2015. Differential fMRI Activation Patterns to Noxious Heat and Tactile Stimuli in the Primate Spinal Cord. *J. Neurosci.* 35, 10493–10502. doi:10.1523/JNEUROSCI.0583-15.2015
- Zhao, F., Williams, M., Meng, X., Welsh, D.C., Coimbra, A., Crown, E.D., Cook, J.J., Urban, M.O.,

Hargreaves, R., Williams, D.S., 2008. BOLD and blood volume-weighted fMRI of rat lumbar spinal cord during non-noxious and noxious electrical hindpaw stimulation. *Neuroimage* 40, 133–147.  
doi:10.1016/j.neuroimage.2007.11.010

Zhao, F., Williams, M., Meng, X., Welsh, D.C., Grachev, I.D., Hargreaves, R., Williams, D.S., 2009. Pain fMRI in rat cervical spinal cord: An echo planar imaging evaluation of sensitivity of BOLD and blood volume-weighted fMRI. *Neuroimage* 44, 349–362.  
doi:10.1016/j.neuroimage.2008.09.001

## **Chapter 3: RESTING-STATE FUNCTIONAL CONNECTIVITY IN THE RAT CERVICAL SPINAL CORD AT 9.4T**

### **3.1. Abstract**

Numerous studies have adopted rsfMRI methods to infer functional connectivity between cortical regions, but very few have translated them to the spinal cord despite its critical role in the central nervous system. Resting-state functional connectivity between gray matter horns of the spinal cord has previously been shown to be detectable in humans and non-human primates, but it has not previously been reported in rodents. RsfMRI of the cervical spinal cord of live anesthetized rats was performed at 9.4T. The quality of the functional images acquired was assessed, and quantitative analyses of functional connectivity in C4-C7 of the spinal cord were derived. Robust gray matter horn-to-horn connectivity patterns were found that were statistically significant when compared to adjacent control regions. Specifically, dorsal-dorsal and ventral-ventral connectivity measurements were most prominent while ipsilateral dorsal-ventral connectivity was also observed but to a lesser extent. Quantitative evaluation of reproducibility also revealed moderate robustness in the bilateral sensory and motor networks that was weaker in the dorsal-ventral connections. This study reports the first evidence of resting-state functional circuits within gray matter in the rat spinal cord and verifies their detectability using rsfMRI at 9.4T.

### **3.2. Introduction**

The use of functional magnetic resonance imaging (fMRI) for detecting neural activation has influenced our views of how the brain is organized since the early 1990s. fMRI detects blood oxygenation level dependent (BOLD) signal changes that have been demonstrated to reflect underlying neural activity (Fox and Raichle, 2007; Logothetis et al., 2001). Early reports examined only task-based studies wherein changes in BOLD signals are interpreted as hemodynamic responses to stimulation (Bandettini et al., 1992; Kwong et al., 1992; Ogawa et al., 1992, 1990). Later on, the advent of resting-state fMRI (rsfMRI) that identifies patterns of highly correlated low frequency fMRI signals without any task or stimulus has been used to infer functional connectivity between cortical regions (Biswal et al., 1995). Since then, rsfMRI has proven to be a powerful approach to delineate and describe functional circuits, and allows us to assess the manner in which

neural systems are intrinsically connected and how they work together to achieve specific functions.

Over the past few decades, numerous studies have used rsfMRI to explore the functional architecture of the brain, but only a handful of studies have translated such techniques to the spinal cord despite its importance serving as a conduit for motor outputs from the brain, peripheral inputs to the brain and as a center for coordinating certain reflexes. This relatively low number of spinal cord fMRI published studies may be attributed to difficulties in obtaining reliable data from the cord because of its small cross sectional area, the augmented influence of physiological noise and magnetic susceptibility issues that arise from surrounding vertebrae and tissues (Eippert et al., 2016a). A recent review by Eippert and colleagues provides an overview of data acquisition and processing denoising approaches that have proven useful for spinal cord fMRI (Eippert et al., 2016a). Nonetheless, several groups have overcome the challenges of spinal fMRI and have reported task-induced activations in gray matter of the human spinal cord (Kornelsen and Stroman, 2007; Stroman et al., 2012; Stroman and Ryner, 2001). Spinal cord injuries in humans have also been demonstrated to exhibit changes in activation detectable with fMRI (reviewed by Stroman et al., 2014)

While task-induced activation and injured patient studies convey valuable information, rsfMRI of the spinal cord potentially could provide a biomarker of the functional integrity of the spine that could be used for clinical diagnosis and prognosis, and the evaluation of therapies, without specific tasks or stimuli, but rsfMRI has been largely unexplored. To our knowledge, reliable rsfMRI in human spinal cord has been demonstrated by only a few other groups to date. Wei et al. applied data-driven independent component analysis (ICA) to describe rsfMRI in the human cervical spinal cord, although the dominant frequency of signal changes was reported to be near the frequency range of the respiratory cycle (Wei et al., 2010). Two recent studies found distinct dorsal and ventral networks that mirrored spinal cord neuroanatomy, suggesting such observations have a neuronal basis (Kong et al., 2014; San Emeterio Nateras et al., 2016). We previously reported robust detection of rsfMRI connectivity in human subjects at ultra-high field (7T) using a hypothesis driven region-of-interest (ROI) analysis (Barry et al., 2015, 2014). Specifically, Barry et al. found consistent functional connectivity in bilateral motor and sensory networks, while a more recent paper from Eippert et al. confirmed these findings and provided further convincing evidence that spinal cord rsfMRI may be a robust technique for clinical

applications (Eippert et al., 2016b). Using a similar ROI-based approach, Liu et al. reported that resting-state networks in the upper cervical spinal cord show strong connectivity, and also compared rsfMRI signals across different vertebral levels (Liu et al., 2016). Harita and Stroman more recently confirmed the presence of spinal cord resting-state BOLD variations and evaluated the contributions of motion and physiological noises to rsfMRI signals in both the brainstem and spinal cord (Shreyas Harita and Stroman, 2017).

In order to interpret rsfMRI BOLD signal changes in humans, multi-modal studies in animals may prove valuable, especially if the effects of controlled injuries or interventions can be related to behavior and underlying neural and cellular changes. Animals afford a range of experimental manipulations that are not possible in human subjects (Hutchison and Everling, 2012). Moreover, preclinical imaging at even higher field strengths allows for greater BOLD sensitivity and submillimeter spatial resolution, while injury models allow us to reliably monitor and quantify longitudinal recovery processes in the spinal cord. Previously, we have shown how a non-human primate (NHP) can be used to follow injury-induced disruptions in functional connectivity within and across spinal segments (Chen et al., 2015). Although NHPs provide a crucial linkage between human and animal data thanks to their high degree of similarity, their use is much more restrictive compared to rodents due to limitations such as handling procedures, costs and management. Moreover, rodents have less inter-subject variability in the brain from an anatomical and functional perspective due to the availability of inbred strains. Thus, we believe imaging of rodent models could provide a robust, cost-effective approach for studying functional organization of the spinal cord and in turn allow a more diverse set of experimental interventions to be investigated.

Significant progress has previously been made towards developing functional imaging of the rat spinal cord, with a focus on detecting stimulus evoked fMRI activation. With early studies indicating that nociceptive information are encoded in the dorsal horns through both temporal and spatial mechanisms (Price, 1988), using quantitative 2-deoxyglucose mapping, Coghill et al. showed that heat stimulation evoked increased metabolic activity somatotopically within the dorsal horn laminal layers (Coghill et al., 1991). fMRI was subsequently introduced as a tool to evaluate spinal effects caused by noxious stimulation with the injection of formalin (Porszasz et al., 1997), as well as electrical stimulation in both the cervical and lumbar spinal cord (Malisza et al., 2003; Malisza and Stroman, 2002; Zhao et al., 2009a, 2008). Taking a step further, fMRI in spinal cord

was used to detect early stages of diabetic neuropathy, where regions of the lumbar spinal cord presented weaker activation during noxious electrical stimulation when compared to control rats (Malisza et al., 2009). Moreover, Zhao et al. (Zhao et al., 2009b) found blood-volume based fMRI in the rat spinal cord to be a robust biomarker of analgesia after the injection of lidocaine. To understand the underlying mechanism of these findings, Lawrence et al. investigated the correlation between neural activation assessed by fMRI and immunohistochemistry by c-fos labeling (Lawrence et al., 2004). Overall, these earlier studies demonstrated the utility of fMRI for detecting regions of stimulus-evoked neuronal activity within the spinal cord gray matter.

To date, little is known about the extent to which the spinal cord is expected to demonstrate functional connectivity similar to the brain, nor whether resting-state signal variations correlate with other metrics of activity and connectivity, nor if they are detectable in rodents. Thus, this study reports the first evidence of resting-state networks in the rat spinal cord and verify their detectability at high field. Methods to mitigate some of the challenges of rat spinal cord imaging have been evaluated at 9.4T, which will inform future studies of functional organization of the cord in different conditions.

### **3.3. Methods**

#### **3.3.1. Animal Preparation**

Five adult male Sprague-Dawley rats ( $291 \pm 76$  grams) were used in this study. Animals were initially anesthetized with 3% isoflurane and underwent endotracheal intubation followed by mechanical ventilation delivering isoflurane in a 1:2 gas mixture of O<sub>2</sub>:N<sub>2</sub>O. During the scans, ventilation rate was set to 60 breaths/min. End-tidal CO<sub>2</sub> and respiration patterns were continuously monitored. Rectal temperature was also measured and maintained with a thermocouple heating unit at 37°C. Animals were securely placed in a customized bed in the supine position. Before fMRI acquisitions, at least an hour was allocated for physiological stabilization, during which shimming was performed and high resolution anatomical images were acquired. Animals were maintained at a stable anesthesia level (0.9-1.1%) under neuromuscular blockade (vecuronium bromide, 1 mg/kg, i.p.) during functional imaging sessions.

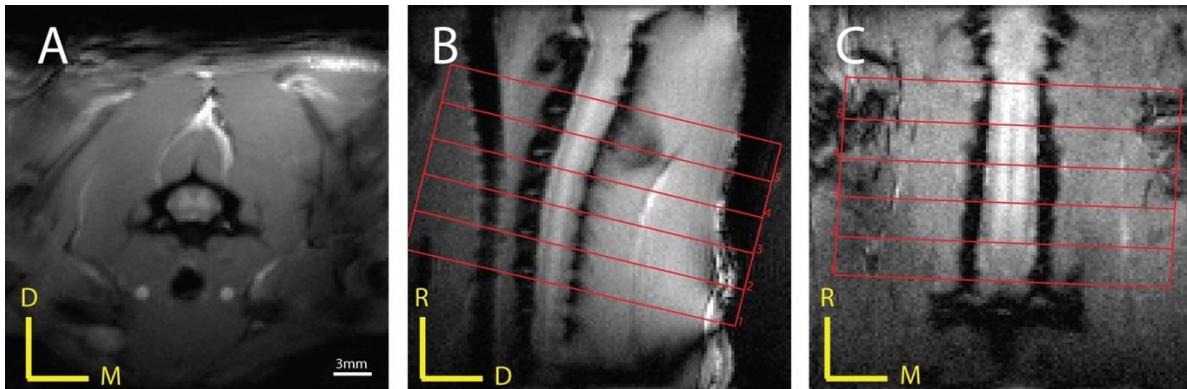


**Figure 20: MTC weighted anatomical images in three different views.** A gradient echo acquisition that incorporated a Gaussian radio frequency saturation pulse was used to obtain (A) axial, (B) coronal and (C) sagittal views of the rat cervical spinal cord with in-plane resolution of  $0.25 \times 0.25 \text{ mm}^2$  and slice thicknesses of 3 mm, 0.5 mm and 0.75 mm, respectively. Red borders and numbers on the images represent axial slice selections for BOLD images. D: dorsal; M: medial; R: rostral.

### 3.3.2. Resting-state fMRI pre-processing

A series of data analysis steps has been established for rsfMRI of the rat spine to minimize physiological noise and tease out BOLD signal fluctuations. This protocol is a modification of the set of pre-processing steps that our group developed previously for humans and NHPs (Barry et al., 2015; Chen et al., 2015):

1. Slice-by-slice rigid body motion correction based on maximization of mutual information was used to estimate three motion parameters (two translations and one rotation) for each slice.
2. BOLD images were then up-sampled to match the final resolution of the anatomical volume ( $0.25 \times 0.25 \times 3\text{mm}^3$ ) with a linear interpolation.
3. Manual alignment of each functional image to the corresponding anatomical MTC anatomical image was performed for all runs and slices in each rat. Quality of the final functional-to-anatomical alignments was visually verified.
4. For each slice, data-driven “nuisance” signals were selected via principal component analysis of the time courses in muscles and cerebrospinal fluid (CSF) voxels. Due to the small size of the spinal cord, only CSF voxels that were not subject to partial volume effects were selected. The first three to five signal components that accounted for at least 70% of the cumulative signal variance in each region, along with motion correction parameters,

were used as signal regressors in a general linear model to reduce their contributions to the fMRI signals. White matter signal was also included as a nuisance signal with separate results.

5. Functional data were filtered with a pass-band between 0.01 and 0.1 Hz using a Chebyshev Type II filter; frequencies below 0.01Hz and above 0.1Hz were filtered out.
6. Before ROI-based analysis of functional connectivity, masks of dorsal and ventral horns as well as white matter were manually defined with the aligned high-resolution axial anatomical images as a reference. Each of these masks was carefully selected to prevent the presence of any partial volumes.

### **3.3.3. In vivo MRI**

All MR images were acquired on a 9.4T Magnex magnet interfaced to a Varian/Agilent spectrometer. A 2-cm diameter transmit-receive radio frequency coil was centered at the C4-C7 region of the rat spinal cord in the iso-center of the magnet. Magnetic field homogeneity was optimized by automatic global shimming and manual fine shimming, followed by local shimming over the spinal cord. In order to locate regions for fMRI data acquisitions, magnetization transfer contrast (MTC) weighted anatomical images were acquired in axial, coronal and sagittal views (Figure 20) using a gradient echo acquisition (TR/TE=200/3 ms, matrix size=128x128, FOV=32x32 mm<sup>2</sup>, slice thickness = 3 mm (axial), 0.50 mm (coronal) and 0.75 mm (sagittal), flip angle=35°), which incorporated a Gaussian pre-saturation radio frequency pulse (RF offset=5000 Hz, flip angle=820°, pulse width=12ms).

BOLD images were acquired using a gradient-echo echo-planar imaging (GE-EPI) sequence across five axial slices (TR/TE=500ms/6.70ms, 6 shots, flip angle=35°, resolution=0.33x0.33x3 mm<sup>3</sup>, 180 volumes). Similar to the study by Zhao et al. (2009), a relatively short echo time was selected to reduce distortions and signal losses caused by field inhomogeneities while the flip angle was adjusted to be approximately equal to the Ernst angle due to the short TR relative to T1 of the spinal cord. Multiple functional runs were obtained for each rat; runs and volumes with excessive motions (> 1.7 mm) and distortions were excluded for subsequent analyses. A total of 21 separate runs from five rats were analyzed for this study.

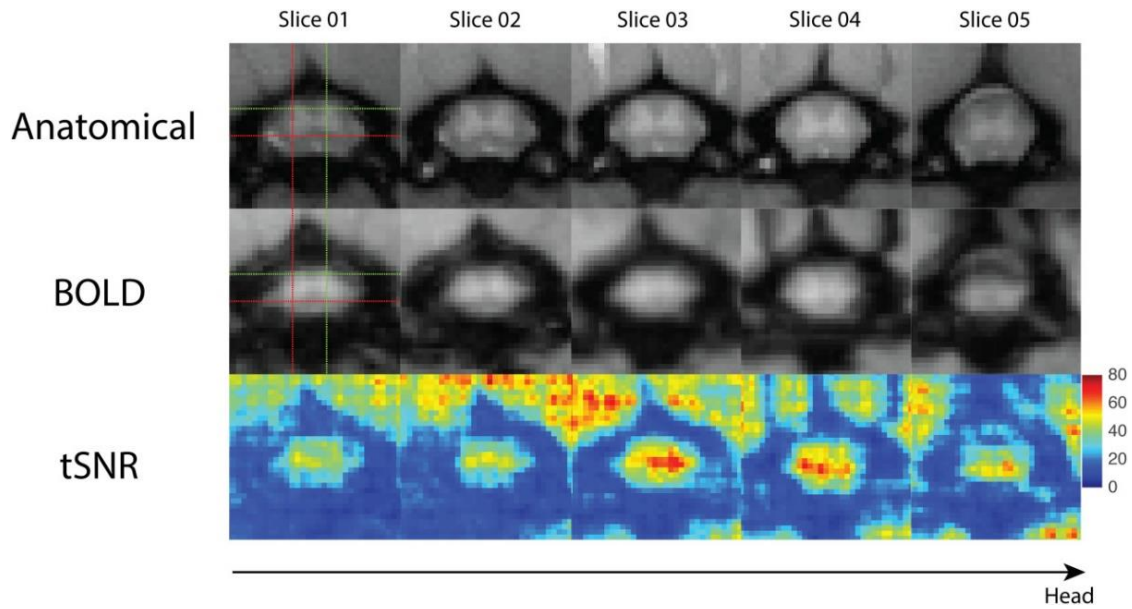


**Figure 21: Anatomical, BOLD and tSNR maps across five slices.** (A) Enlarged views of the cervical spinal cord using magnetization transfer contrast (MTC). Imaging planes of the five slices correspond to the red boxes in Figure 20. (B) Pre-processed functional BOLD images of the same five slices. Goodness of alignments between anatomical and functional images are indicated by the crosshair pointing to the same left ventral horn (red) and right dorsal horn (green). (C) TSNR maps of the functional images presented in B.

### 3.3.4. Data and Statistical Analyses

Temporal signal-to-noise (tSNR) maps were constructed by computing the mean of each time series divided by its standard deviation. tSNR was computed as a quality assessment of BOLD images. Averaged time series of the dorsal- and ventral-horn voxels from one slice were displayed and computed after converting raw signal amplitudes to percentage signal BOLD.

Voxel-based correlation maps were calculated using the Pearson's linear correlation coefficient ( $r$ ) between a seed voxel and all other voxels in the spinal cord. Spinal cord masks that exclude voxels of the CSF were applied. A statistical threshold of  $r > 0.4$ ,  $p < 2 \times 10^{-5}$  was used to depict voxels showing strong correlations within the gray matter horns and white matter. A minimum cluster threshold of 2 voxels was also applied to reduce spurious correlations. This number was determined based on the size of the horns and the actual voxel size to minimize partial volume effects potentially introduced by the linear interpolation from functional to anatomical data (step 2).

**Table#1: Temporal signal-to-noise-ratio (tSNR) of the cervical spinal cord that covers the four segments (C4-C7) of interest across runs in the five rats in this study.**

	<b>tSNR of the Spinal Cord</b>
Rat#1	29.94±4.92
Rat#2	36.10±1.69
Rat#3	17.84±1.19
Rat#4	25.01±1.59
Rat#5	35.20±2.72

An ROI-based correlation analysis was performed using a customized toolbox in *spm12* to summarize functional connectivity between horns of the spinal cord in three slices that correspond to C4/C5, C5/C6, and C6/C7. Our quantitative horn-horn connectivity metrics are similar to those described in two previous papers (Barry et al., 2015; Chen et al., 2015). Briefly,  $m$  individual voxel time series of a horn were correlated with  $n$  time series of another horn. Subsequently, the maximum of this correlation vector was selected as the metric of functional connectivity between the pair of horns. This was performed for all pairs of ROIs which include the four horns of the spinal cord and two adjacent white matter regions within each slice. Ipsilateral dorsal-ventral correlation values from left and right hemicords were concatenated for group analysis. Similarly for contralateral dorsal-ventral connectivity: left dorsal-right ventral and right dorsal-left ventral measurements were combined. Functional connectivity patterns of interslice ROIs were also evaluated using methods described in our previous publication in NHPs (Chen et al., 2015). Kong and colleagues have demonstrated the use of data driven methods to separate the spinal cord into different resting-state networks (Kong et al., 2014). Complementary to such an approach, our method allows us to select regions of the spinal cord based on hypotheses derived from stimulus-driven studies in rats (Malisza and Stroman, 2002; Zhao et al., 2009a) and NHPs (Chen et al., 2015; Yang et al., 2015). A nonparametric Mann-Whitney-Wilcoxon test was then used to evaluate the differences between different combinations of correlation coefficient pairs. It is also important to note that Bonferroni correction was applied after selecting the voxel that demonstrates the highest correlation; the correction was made to the number of ROI comparisons in group analysis and not voxel-wise at the point of determining the most significant voxel. In addition, white matter signal was also included as a nuisance signal with separate results presented.

Lastly, reproducibility and agreement of the connectivity measures were computed within each animal and within each slice. Specifically, fMRI data within each animal were split into two subsets, even and odd runs. Functional connectivity measures from each subset from the same animal were subsequently paired. This was done within each slice for the three slices in the spinal cord. To quantify the degree of reproducibility of spinal cord functional connectivity, Pearson's linear correlation coefficient was computed between the paired runs from the two subsets. Bias and agreement between the two subsets of measures were further evaluated with Bland-Altman plots. These analyses were then repeated with a wider frequency band (0.01-0.16Hz) to investigate the effects of higher frequency (0.1-0.16Hz) on the magnitude and reproducibility of resting-state connectivity measures ( $r$  values). Results from data using a wider frequency band were also computed.

### **3.4. Results**

#### **3.4.1. Quality of BOLD images at the cervical spinal cord**

fMRI images were pre-processed in order to minimize motion and physiological noise, and to tease out BOLD signal fluctuations in the spinal cord. Figure 21 presents anatomical images with corresponding BOLD axial images and tSNR maps. TSNR of all rats were computed across all runs in the middle three slices of the spinal cord in and Table#1. Figure 22 displays averaged time series of the four horns showing BOLD signal fluctuations similar to those found in humans (Barry et al., 2014). Functional images are of sufficiently high quality to provide adequate contrast between gray and white matter. In Figure 21, good alignment between anatomical and functional images is also demonstrated with the red and green crosshair pointing to the same left-ventral and right-dorsal horn respectively.

#### **3.4.2. Intrinsic functional connectivity patterns of the rat spinal cord horns**

Signal changes to electrical forepaw stimulus have previously been located between C4-C7 segments on ipsilateral dorsal regions. Building upon this finding, we examined ROI-based pair-wise correlation maps of rsfMRI signals in all four spinal horns and white matter regions within these segments of the spinal cord. For example, a seed voxel placed in the dorsal horn

results in strong correlation to the corresponding contralateral dorsal horn, and similarly for the ventral horns. The presence of functional connectivity between ipsilateral dorsal-ventral horns is also observed although not consistently across all runs and animals. Number of voxels tested in the spinal cord that exclude voxels of the CSF was on average 132.6 voxels across the middle three slices. Functional connectivity patterns between dorsal-dorsal and ventral-ventral horns were reproducible across animals in this study as shown in Figure 23.

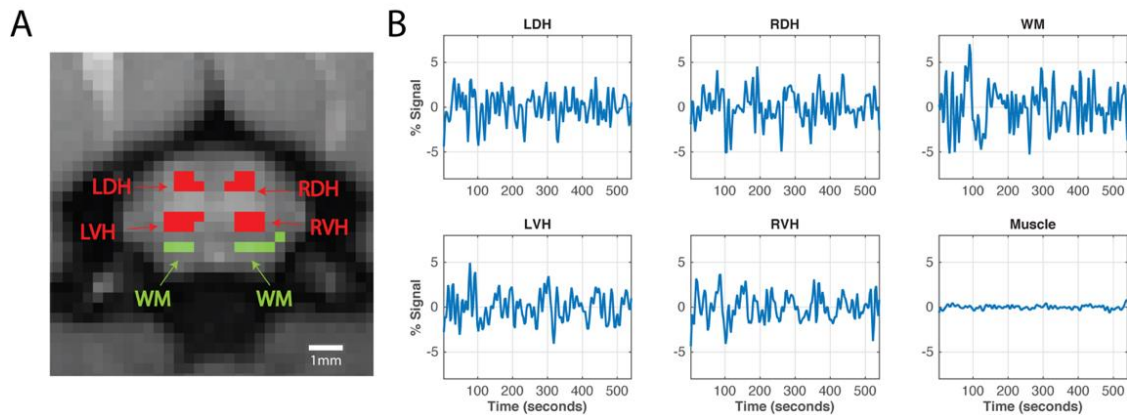


**Figure 22: Horns of the cervical spinal cord, white matter and averaged time series.** (A) Anatomical MTC image of the rat cervical spinal cord. Red regions indicate the four horns of the spinal cord – left dorsal horn (LDH), left ventral horn (LVH), right dorsal horn (RDH), and right ventral horn (RVH) – while green regions indicate white matter (WM) voxels that were subsequently used for region-of-interest (ROI) analysis. (B) Averaged BOLD time series of the LDH, RDH, LVH, RVH and WM of the spinal cord, and muscle signal that has been regressed.

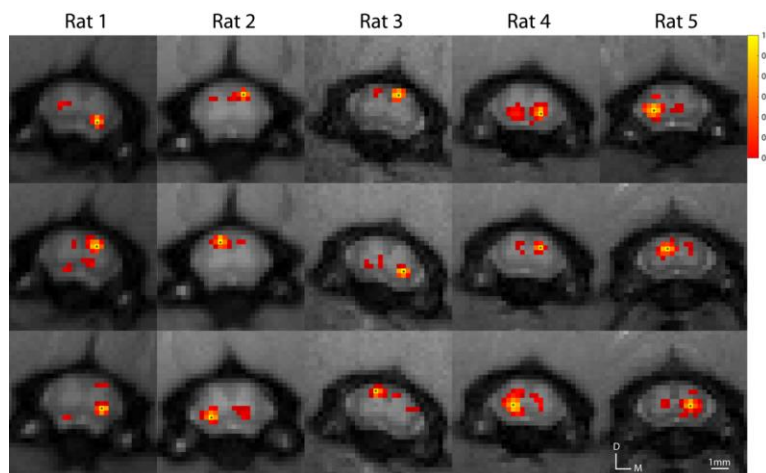


**Figure 23: Examples of within-slice resting-state correlation maps in the cervical spinal cord across all five animals.** Correlation maps were thresholded (Pearson’s correlation coefficient,  $r > 0.4$ ) and the yellow voxels with asterisks indicate seed voxels. A minimum cluster threshold of 2 voxels was also used to prevent any spurious correlations. D: dorsal; M: medial.

### 3.4.3. Differential functional connectivity among intraslice ROIs and reproducibility

The strengths of resting-state correlations between different pairs of seeds in the horns within each slice were quantified at the group level. Whisker boxplots of the group mean values and variations of correlation values are presented in Figure 24. Robust correlations are observed between left and right dorsal horns as well as between left and right ventral horns across all four spinal cord segments. For example, mean correlation values of 0.53 and 0.47 were computed for dorsal-dorsal and ventral-ventral connections respectively ( $p < 0.005$  when compared to white matter controls, Bonferroni corrected) for the C5/C6 segment, although no statistical difference was observed between them. Weaker ipsilateral dorsal and ventral horn connectivity measurements were also observed.

Reproducibility of spinal cord connectivity was quantified with correspondences between odd and even runs from each animal as shown in Figure 25. Qualitatively, data points in correlation plots for dorsal-dorsal (Figure 25A) and ventral-ventral (Figure 25B) connectivity lie predominantly on the diagonal line (slope=1) with correlation values of 0.61 ( $p = 4.59 \times 10^{-4}$ ) and 0.67 ( $p = 6.71 \times 10^{-5}$ ) respectively. In contrast, dorsal-ventral connectivity presents significantly lower correspondence between odd and even runs. Furthermore, visual inspections of the Bland-Altman plots reveal that dorsal-dorsal and ventral-ventral connectivity measurements present smaller ranges of limits, signifying better agreement between measurements, than those of dorsal-ventral connections. Overall, we found that correlation between spinal cord gray matter horns are connected strongly to each other but with varying strengths; in particular, dorsal-dorsal and ventral-ventral connections are most reproducible in terms of strength and spatial distribution along the cord.

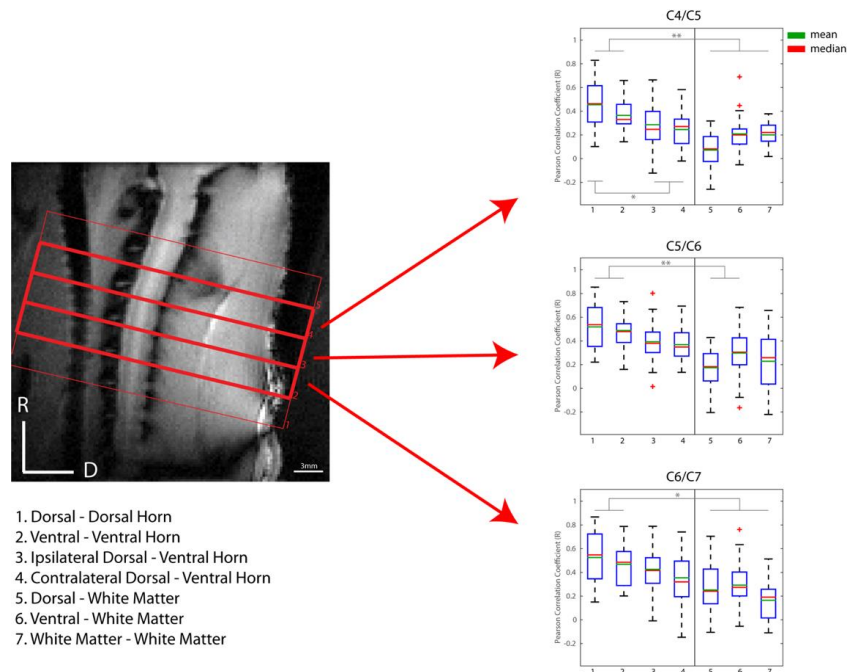


**Figure 24: Group analysis of functional connectivity between spinal cord gray matter horns and “control” white matter regions.** (Left) Sagittal MTC image of the rat cervical spinal cord. (Right) Boxplots of correlation strengths between seven ROI pairs in C4/C5 (top), C5/C6 (middle) and C6/C7 (bottom) of the spinal cord. Corresponding slices of each cervical spinal region are indicated by red arrows. \* $p < 0.05$ , \*\* $p < 0.005$  (non-parametric Mann-Whitney test, Bonferroni corrected). The red crosses represent outlier data points.

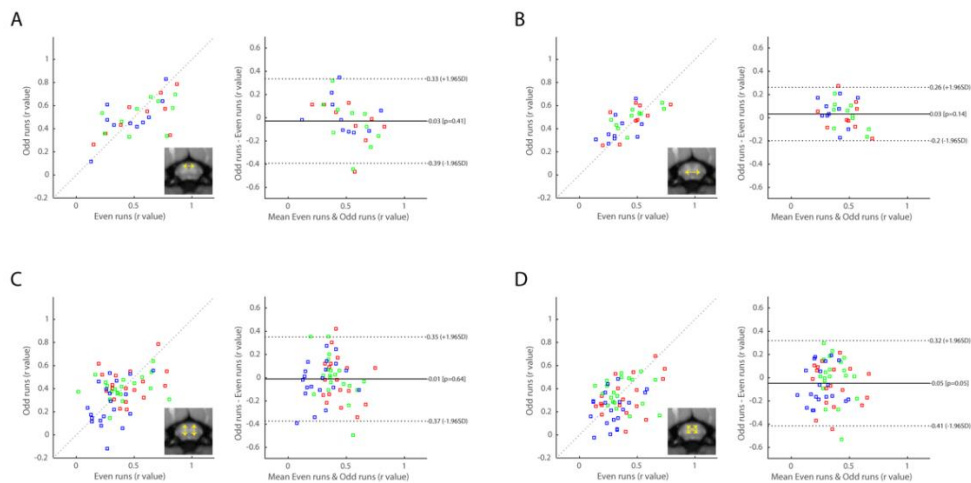


**Figure 25: Reproducibility and agreement of within-slice horn-to-horn functional connectivity.** Functional connectivity measurements were divided into two sub-groups that consist of even and odd runs for each animal. (Left of each subplot) Correlation strengths in even runs were then plotted against those in odd runs. To quantitatively measure reproducibility, the cross correlation values (Pearson’s coefficient,  $r$ ) are computed to be 0.61 ( $p = 4.59 \times 10^{-4}$ ) for (A) dorsal-dorsal connectivity, 0.67 ( $p = 6.71 \times 10^{-5}$ ) for (B) ventral-ventral connectivity, 0.25 ( $p = 0.0593$ ) for (C) ipsilateral dorsal-ventral connectivity, and 0.37 ( $p = 0.0044$ ) for (D) contralateral dorsal-ventral connectivity. (Right of each subplot) Bland-Altman plots of horn-to-horn connectivity. Solid lines represent the mean differences between the two subsets, while the dotted lines are 95% limits of agreement. Blue dots denote values from the inferior slice (C4/C5, slice04), green denotes values from the middle slice (C5/C6, slice03), and red dots denote values from the superior slice (C6/C7, slice02).

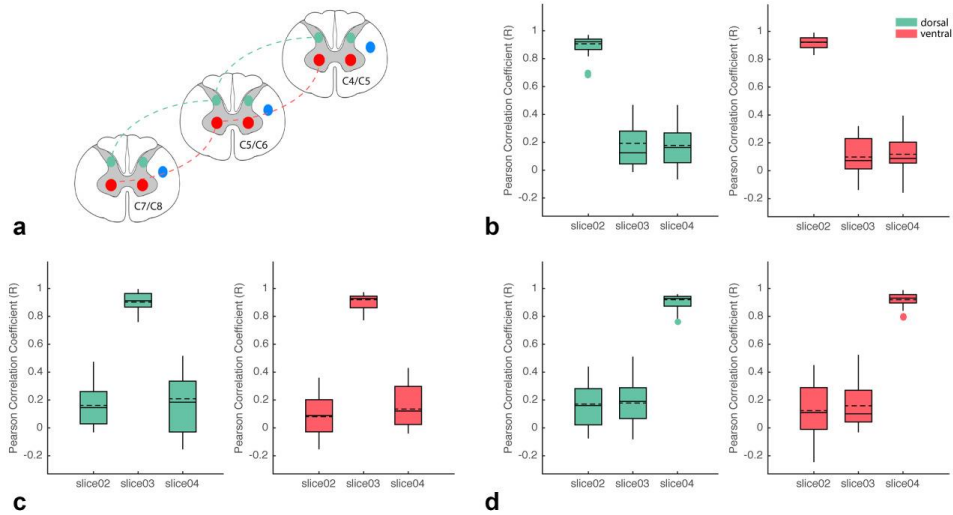


**Figure 26: Group analysis of functional connectivity between spinal cord gray matter horns (left) across different spinal segments.** Schematic diagram modified from Chen et al. (22) that illustrates pair-wise correlation analyses with respect to seed ROI in LVH (red lines) and LDH (green lines). (B) Group boxplots of correlation strengths between ROI in slice 2 and those in slices 3 and 4 for both LVH (red shaded boxplots) and LDH (green shaded boxplots). Similarly, correlation strengths were computed and displayed as group whisker boxplots with respect to seeds in slices 3 (C) and 4 (D). Solid and dashed horizontal lines inside each boxplot indicate the median and mean respectively. Shaded boxplots were generated using gramm (Morel, 2016).

### 3.4.4. Functional connectivity between inter-slice horns

To quantify how far along the spinal cord the functional connectivity extends, we measured correlation coefficients between ROIs in corresponding horns (e.g., left ventral-to-ventral or left dorsal to dorsal) in three slices that spanned C4-C7 (Figure 26). For both ventral-ventral and dorsal-dorsal connections, we observed that voxels within the seed ROI on the same slice were highly correlated ( $r \sim 0.9$ ), as expected. As the distance between ROIs was increased to one or two slices away, the correlation values dropped significantly ( $r \sim 0.2$  and  $r \sim 0.1$ ) between both dorsal and ventral horns. It is also important to note that we have only examined connections between dorsal-dorsal and ventral-ventral horns (connectivity between horns of the right hemi-cord are presented in Figure 27). Incorporating all possible combinations across segments would not only have made the analysis significantly more complex by vastly increasing the number of comparisons, but also the connectivity between dorsal and ventral horns remains speculative even within the same segment. Overall, our observations indicate that functional connectivity in the rodent spinal cords is spatially constrained across one to two cervical segments.

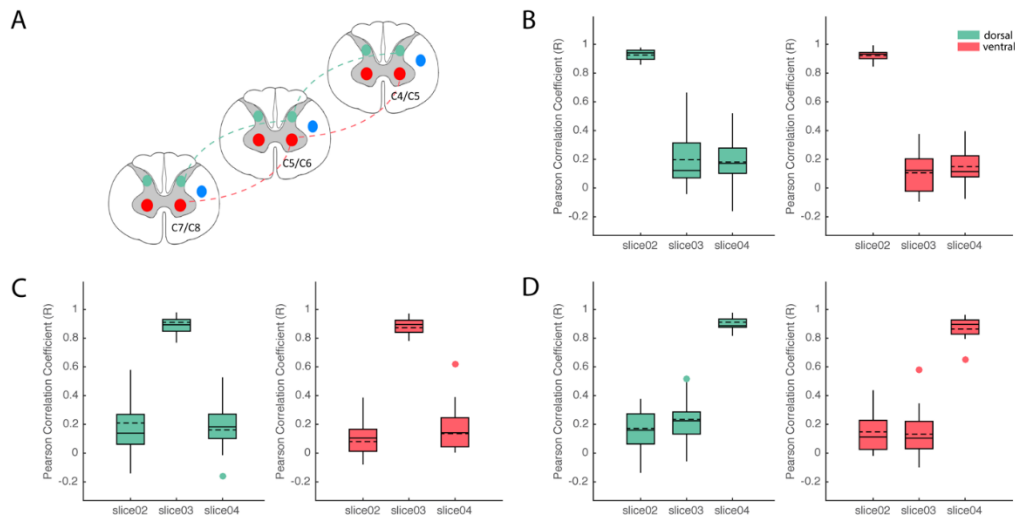


**Figure 27: Group analysis of functional connectivity between spinal cord gray matter horns (right) across different spinal segments.** The same analyses performed in Figure 26 were repeated with respect to seed ROIs in RVH and RDH.

### 3.4.5. Effect of frequency bandpass filtering in resting-state functional connectivity

In order to investigate the effects of bandpass filtering of rsfMRI signals beyond the conventional 0.1Hz cutoff (0.01-0.1Hz), functional connectivity and reproducibility analyses were repeated with a wider range of frequency (0.01-0.16Hz) as shown in Figure 28. Correlation trends between ROI pairs remained largely unaffected when compared to findings with the conventional lower frequency range shown in Figure 25, and with notably lower reproducibility and correlation values in dorsal-ventral connections than those in dorsal-dorsal and ventral-ventral networks. That being said, we observed increases in reproducibility measurements for dorsal-dorsal, ipsilateral dorsal-ventral, and contralateral dorsal-ventral connections: 0.66 ( $p=1.08 \times 10^{-4}$ ) for dorsal-dorsal connectivity, 0.30 ( $p=0.023$ ) for ipsilateral dorsal-ventral connectivity, and 0.43 ( $p=8.80 \times 10^{-4}$ ) for contralateral dorsal-ventral connectivity. While ventral-ventral reproducibility did not benefit from the removal of the bandpass filter with a slightly decreased reproducibility value (0.66,  $p=8.45 \times 10^{-5}$ ), it remained to be the most reproducible connection among the four horn-horn pairs. Time series and corresponding power spectra with and without bandpass filtering are shown in Figure 29.

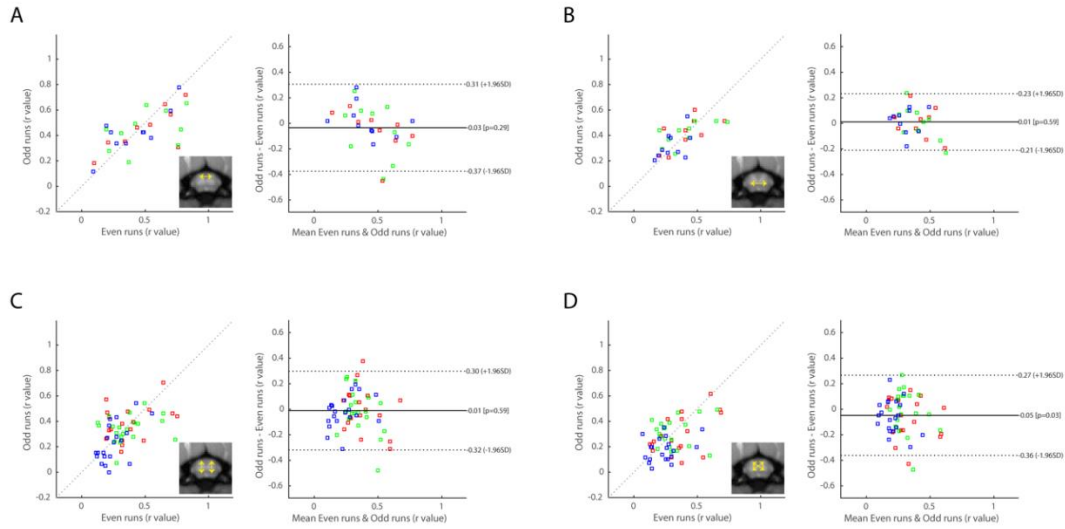


**Figure 28: The same analyses performed in Figure 25 were repeated without the use of bandpass filtering (0.01-0.16Hz).** (Left of each subplot) Correlation strengths in even runs were then plotted against those in odd runs. To quantitatively measure reproducibility, the cross correlation values (Pearson's coefficient,  $r$ ) are computed to be 0.66 ( $p=1.08 \times 10^{-4}$ ) for (A) dorsal-dorsal connectivity, 0.66 ( $p=8.45 \times 10^{-5}$ ) for (B) ventral-ventral connectivity, 0.30 ( $p=0.023$ ) for (C) ipsilateral dorsal-ventral connectivity, and 0.43 ( $p=8.80 \times 10^{-4}$ ) for (D) contralateral dorsal-ventral connectivity. (Right of each subplot) Bland-Altman plots of horn-to-horn connectivities. Solid lines represent the mean differences between the two subsets, while the dotted lines are 95% limits of agreement. Blue dots denote values from the inferior slice (C4/C5, slice04), green denotes values from the middle slice (C5/C6, slice03), and red dots denote values from the superior slice (C6/C7, slice02)

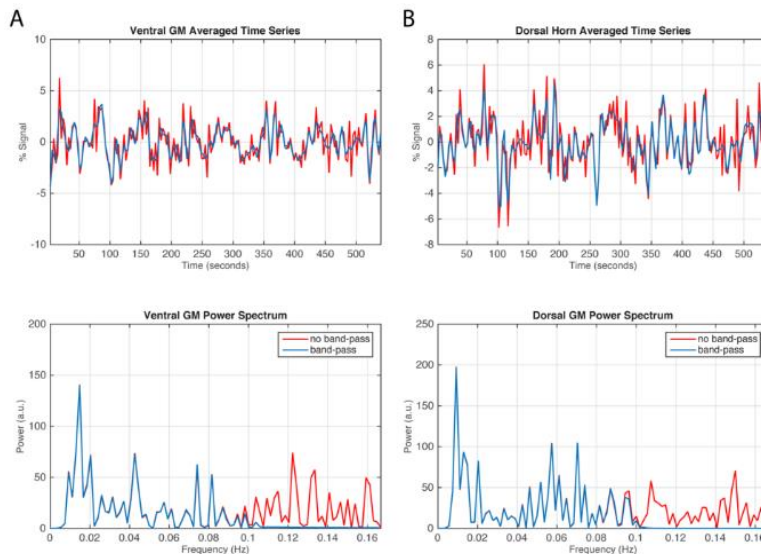


**Figure 29: Power spectra and time series for (A) ventral and (B) dorsal gray matter regions in Figure 22 before (red) and after (blue) band-pass filtering.** 69% and 62% of the signal power lies in the low frequency range ( $<0.1$ Hz) in dorsal and ventral horns respectively. While observation of the power spectra in dorsal and ventral horn also reveals that the original bandpass filter between 0.01 and 0.1Hz was a sound choice, power in higher frequency regions may still contain information relating to gray matter horn connectivities.

### 3.5. Discussion and conclusions

#### 3.5.1. Challenges in functional imaging of the rat cervical spinal cord

Imaging the rat cervical spinal cord poses multiple challenges. The small cross-sectional area demands high spatial resolution, while the presence of a relatively thick layer of tissue on the animal's back affects sensitivity. With a 2 cm surface coil at ultra-high field of 9.4T, functional imaging at  $0.33 \times 0.33 \text{ mm}^2$  in plane resolution provided adequate resolution with reasonable sensitivity. High contrast-to-noise ratio anatomical MTC weighted images allowed us to make precise image alignments and reproduce results within each animal.

The selection of MRI sequence and BOLD image processing steps were key to providing a sensitive protocol for the detection of resting-state networks in the cervical spinal cord. Zhao et al. previously demonstrated the highest sensitivity of fMRI signals to pain stimulus was achieved using GE-blood volume (BV) weighted images, followed by GE BOLD and spin-echo (SE) BOLD in the cervical rat spinal cord (Zhao et al., 2009a). Here, a GE-BOLD sequence was selected which avoids the use of a contrast agent. A set of refined image analysis steps was used that was built upon what had been successful in our previous human and NHP studies (Barry et al., 2015; Chen et al., 2015). An independent study evaluated similar key pre-processing steps and was successful at reproducing our previous data, which led to that study's conclusion that spinal cord resting-state connectivity is reliably measurable (Eippert et al., 2016b). Our findings support these previous studies as reflected in the robust detection of resting-state functional connectivity in rodents.

A potential major challenge to imaging of the cervical spinal cord compared to the brain is the presence of more pronounced physiological noise caused by respiration and cardiac pulsations. The spinal cord is close to large organs such as the lungs which may cause motion, and may result in shifts in the EPI images in the phase encoding direction and changes in  $B_0$  that can significantly degrade the quality of functional images (Raj et al., 2001). In addition, artifacts due to systematic signal changes through inflow effects may also be induced. In order to minimize such effects, previous studies have used model-based as well as data driven approaches for physiological corrections (Eippert et al., 2016a). Harita and Stroman recently reported that 14% and 2.6% of signal variances in rsfMRI of the human spinal cord can be attributed to cardiac and respiratory sources respectively (Shreyas Harita and Stroman, 2017). While model-based methods such as RETROICOR have been shown to improve the specificity of detection in humans (Glover et al.,

2000), our experiences in imaging the spinal cord in well-restrained and mechanically ventilated animals under anesthesia at 9.4T have shown such corrections have minimal effects when included in the pre-processing steps (Figure 30 and Table#2). The non-instantaneous slice acquisition of BOLD fMRI data across multiple shots may also render the unsuitability of applying RETROICOR. Specifically, the necessary cardiac and respiratory phases for RETROICOR's Fourier modeling cannot be generated uniquely. Thus, the animals' physiological traces were not recorded in this study to allow such corrections but instead, we 1) synchronized ventilation rate to the acquisition interval, 2) used a data-driven approach for physiological noise correction, CompCor method (Behzadi et al., 2007), that derives noise regressors from regions that are unlikely to contain neural signals, and 3) securely positioned the animals in a supine position on a customized holder and bed along with administration of paralytic agent. In Figure 23, we see the majority of the connectivity patterns are focally concentrated in the gray matter horns and not in adjacent white matter. We have also included muscle signals as control regions and regressed them out of the time series of gray matter horns. We therefore conclude that gray matter correlations are unlikely to be driven by spatially correlated physiological noise. Conclusions drawn on the relative importance of physiological correction techniques in fMRI studies should also take into account of the suitability of the applied methods.

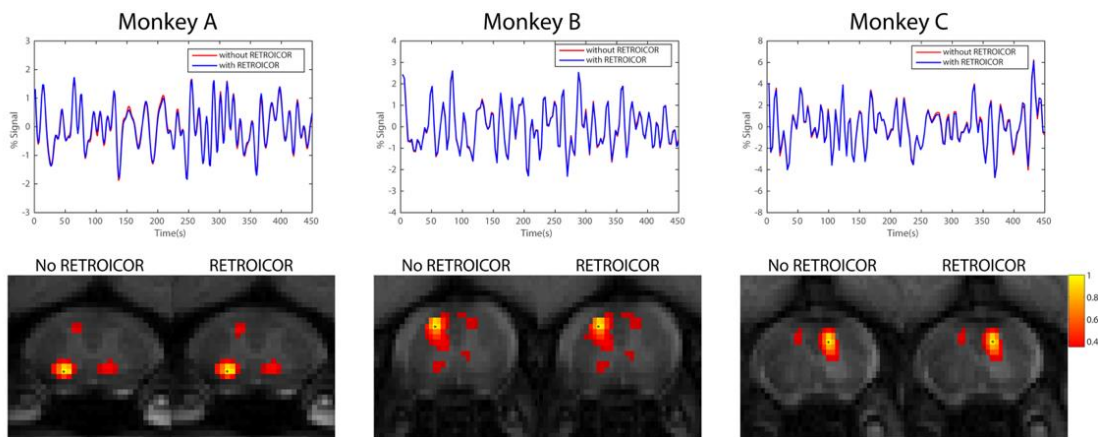


**Figure 30: Effects of RETROICOR on rsfMRI in the cervical spinal cord of anesthetized and mechanically ventilated non-human primates.** (Top row) Time series before (red) and after (blue) applying RETROICOR in the pre-processing pipeline; data acquisition and pre-processing steps can be found at Chen et al., 2015 (Chen et al., 2015). Corresponding within-slice functional connectivity map in each of the three monkeys. Correlation maps were thresholded (Pearson's correlation coefficient,  $r > 0.35$ ) and the yellow voxels with asterisks indicate seed voxels.

**Table#2: Percent signal change of averaged time series in gray matter spinal cord horns with the application of RETROICOR in non-human primates.** Multiple imaging runs across three squirrel monkeys were used; left dorsal horn (LDH), left ventral horn (LVH), right dorsal horn (RDH), and right ventral horn (RVH).

	<b>RVH</b>	<b>LVH</b>	<b>RDH</b>	<b>LDH</b>
Monkey A	0.07±0.01	0.06±0.02	0.06±0.01	0.07±0.01
Monkey B	0.05±0.02	0.06±0.03	0.06±0.02	0.08±0.03
Monkey C	0.10±0.03	0.10±0.05	0.09±0.07	0.23±0.14

### 3.5.2. Physiological noise

Artificially ventilated animals have a constant ventilation rate and shape, and present physiological frequencies that are more narrow and predictable within and across animals. Specifically, we modified the ventilator to allow a precise digital input of the respiration rate. We set the ventilation rate to 60 breaths per minute in order to synchronize with a volume acquisition time of 3 seconds, which ensures minimal aliasing into the frequency band of interest. The effectiveness of this technique has been successfully demonstrated in Zhao et al. (Zhao et al., 2009a). Kalthoff and colleagues, who investigated the impact of physiological noise in rat rsfMRI brain networks at 11.7T (Kalthoff et al., 2011), also pointed this out. In fact, they found a minor role of cardiac traces, and the regression of respiratory waveforms only marginally contributed to the explained variance; standard motion correction was capable of removing much of the respiratory noise from their data (Kalthoff et al., 2011). While we realize Kalthoff’s study focused on rat brains which are less prone to physiological artifacts, the investigation of how physiological noise plays out in rodents at ultra-high field sheds light into how rsfMRI data in well-controlled anesthetized animal studies should be handled, and confirms our experience that the benefits of various corrections found useful in human studies do not necessarily translate to studies in rats at high field.

Motion parameters, muscle and CSF signals were regressed out before correlations were analyzed, which further reduced the likelihood of artificially increasing correlation values due to physiological noise. This approach was shown to be successful in our previous human and animal spinal cord studies (Barry et al., 2015; Chen et al., 2015), and has further been noted to outperform RETROICOR-based denoising in the brain (Behzadi et al., 2007). It is important to note, however,

that we do not dismiss the merits of RETROICOR or other modeling-based approaches, but rather we believe that our experimental setup and pre-processing steps mitigate its effects.

### **3.5.3. Functional relevance of resting-state connectivity in the spinal cord**

It has been widely shown that different brain regions engaged in processing specific external stimuli exhibit strong resting-state functional connectivity (Chen et al., 2015; Cohen-Adad et al., 2010; Fox and Greicius, 2010; Fox and Raichle, 2007; Vincent et al., 2007). For example, our previous study of the SI cortex shows regions that represent different distal finger pads are highly correlated in a resting state in both time and space with underlying synchronized electrophysiological activity and anatomical connections between them (Wang et al., 2013). This observation was further extended to the spinal cord in NHPs where correlation between stimulus-driven activation patterns and resting-state functional connectivity was observed (Chen et al., 2017, 2015). Similarly in rats, forepaw pain stimuli have been shown in previous publications to be reliably located in the dorsal horns (Malisza and Stroman, 2002; Zhao et al., 2009a). Our finding that dorsal horns of the spinal cord are highly correlated supports these findings and further indicates baseline functional connectivity between gray matter horns of the spinal cord may be an organizational feature of the central nervous system.

### **3.5.4. Reliability and reproducibility**

Our current analysis suggests a moderate reproducibility of bilateral sensory and motor networks in the spinal cord, while dorsal-ventral functional connections appear to be less robust. Similarly in humans, Barry et al. (2015) reported moderate reproducibility in dorsal-dorsal and ventral-ventral connections (intraclass correlation coefficient (ICC) values: 0.53 to 0.58), while dorsal-ventral networks presented weaker reliability (ICC values: 0.35 to 0.46). In bilateral motor and unilateral sensory networks revealed with ICA, Kong et al. (2014) also found fair reliability in more than half the voxels (ICCs > 0.4), and a quarter of the voxels showed good reliability (ICCs > 0.6). In a pain stimulus evoked study of the rat cervical spinal cord, reproducibility reached up to a cross correlation value of 0.81 ( $p=1.1 \times 10^{-9}$ ) (Zhao et al., 2009a). Despite a greater mean correlation strength in the dorsal-dorsal connection, we observed a higher reproducibility in the ventral-ventral network. This observation is consistent with a recent investigation that explored the robustness of spinal cord rsfMRI signals against variations in the analysis pipeline: the study

reported excellent robustness in ventral horn connectivity while dorsal horn connectivity was less robust (Eippert et al., 2016b). While ventral-ventral connectivity presented high reproducibility in our study, which may be attributed to the reduced inter-subject variability of rats and imaging at a high field, care must still be taken to interpret these findings. As Barry et al. pointed out, these measurements of reliability are dependent on specific experimental details such as imaging protocols and pre-processing pipelines (Barry et al., 2014). While a direct comparison of these reproducibility measures across different studies cannot be accurately made, our study found a moderate level of reproducibility in bilateral sensory and motor networks.

### **3.5.5. Spinal cord white matter**

While regressing out “nuisance” signals in the pre-processing has been shown to improve the tSNR, the use of white matter as a regressor raises an intriguing question. White matter BOLD signals have conventionally been disregarded due to its sparse vasculature compared to gray matter. However, recent reports have shown reliable BOLD detections of white matter in parts of the brain (Gawryluk et al., 2014). In the spinal cord, Conrad et al. has also recently found an increase in BOLD signal in both gray and white matter when human volunteers were subjected to a hypercapnia gas paradigm (Conrad et al., 2017). Similarly, Ding et al. has previously shown that a seed placed in the corpus callosum of both hemispheres presented high correlations to other white matter voxels that extend over long distances (Ding et al., 2016, 2013). The connectivity strengths between seeds placed in white matter regions in this study (last column of Figure 24) are relatively weaker than for gray matter but the correlation values seem high to be attributed simply to noise. Negative correlations between white matter and horn regions are also observed, consistent with what we have previously found in humans (Barry et al., 2014). Several reports have found the regression of white matter signals to have minimal effects on resting-state correlations in gray matter spinal cord. Thus, we re-computed functional connectivity strengths between the horns and control regions, just as in Figure 24, and the same general trends of greater dorsal-dorsal and ventral-ventral connectivities were preserved (Figure 31). In addition, a stronger statistical difference between horns and white matter control was observed reaching a p-value of 0.05 (Bonferroni corrected) with white matter-to-white matter correlation strength significantly decreased, as expected. Clearly, the nature and origins of spinal cord white matter signals require further investigations.

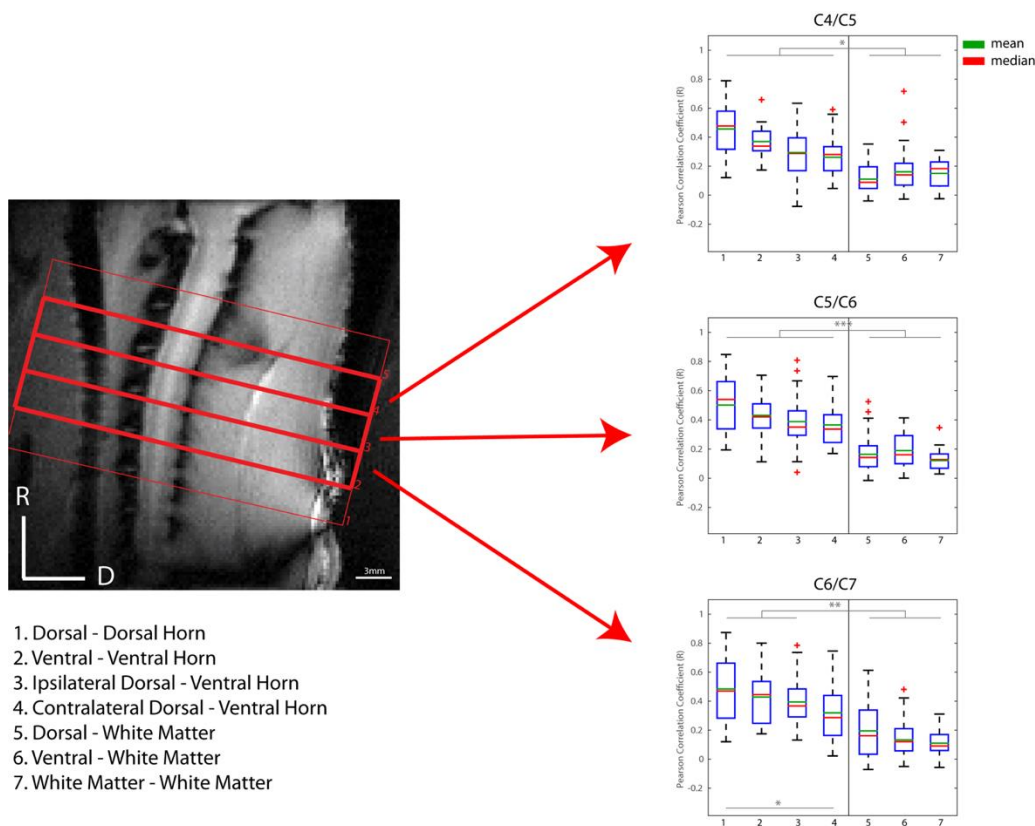


**Figure 31: Group analysis of functional connectivity between spinal cord gray matter horns and “control” white matter regions with white matter signal regression.** (Left) Sagittal MTC image of the rat cervical spinal cord. (Right) Boxplots of correlation strengths between seven ROI pairs in C4/C5 (top), C5/C6 (middle) and C6/C7 (bottom) of the spinal cord. Corresponding slices of each cervical spinal region are indicated by red arrows. \* $p < 0.05$ , \*\* $p < 0.01$ , \*\*\* $p < 1 \times 10^{-4}$  (non-parametric Mann-Whitney test, Bonferroni corrected). The red crosses represent outlier data points.

### 3.5.6. Effects of bandpass filtering

The basis of resting-state functional connectivity lies in correlations between spontaneous low frequency fluctuations, typically between 0.01-0.1Hz, of BOLD signals, in both humans and NHPs. This range of frequency in BOLD signals has been shown to robustly identify resting-state networks and validated with electrophysiology in animal studies (He et al., 2008; Niessing et al., 2005; Nir et al., 2008; Shi et al., 2017; Wang et al., 2012; Wilson et al., 2016). However, emerging evidence has begun to reveal additional information beyond this conventional cutoff in the brain and possibly in the spinal cord (Barry et al., 2015; Boubela et al., 2013; Boyacioglu et al., 2013; Chen and Glover, 2015; Eippert et al., 2017; Gohel and Biswal, 2015; Lee et al., 2013; Niazy et al., 2011; Wu et al., 2008). Specifically, studies have examined possible meaningful correlations at up to 0.5Hz (Chen and Glover, 2015), 0.75Hz (Gohel and Biswal, 2015) and even beyond 0.8Hz

(Boubela et al., 2013; Lee et al., 2013). In the spinal cord, Eippert and colleagues reported increases in significant ventral and dorsal connectivity after removing the band-pass filter (Eippert et al., 2017). Furthermore, the use of band-pass filtering outside the general linear model must be handled with care as it may artificially inflate false-positive rates (Brooks, 2014). We also reported an increase in reproducibility with a higher frequency bandwidth ( $<0.13\text{Hz}$ ) in humans at 7 Tesla (Barry et al., 2015). Similarly in this current study, trends between connectivity values were unaffected after the removal of the low-pass filter (Figure 28), with ventral-dorsal connectivity remaining notably low. However, we observed increases in reproducibility in three out of four ROI pairs with corresponding narrower limits of agreement. Observation of the power spectra in dorsal and ventral horns (Figure 29) also reveals that the original bandpass filter between 0.01 and 0.1Hz was a sound choice, although power in higher frequency regions may still contain information relating to gray matter horn connectivities. As Barry et al. and Eippert et al. pointed out, the acquisition of functional data at faster sampling rates are needed to provide a more complete picture of the frequency dependencies of signals and physiological noises in the spinal cord (Barry et al., 2015, 2014; Eippert et al., 2016b).

### **3.5.7. Inter-species differences**

Spinal cord gray matter horns in rats were observed to be highly correlated in this current study, especially between dorsal-dorsal and ventral-ventral horns. These strongly correlated bilateral motor and sensory networks are consistent with what were observed in recent studies of non-human primates and awake humans (Barry et al., 2015; Chen et al., 2015). Specifically, we observed the correlation between dorsal horns to be stronger than between ventral horns, although no statistical differences were found between them. This finding is consistent with healthy NHP controls while human studies have reported mixed results. Barry et al. found a greater ventral-to-ventral connectivity and attributed this to the narrower structure of the dorsal horns – thus, more susceptible to partial volume effects and registration inaccuracies – as well as the presence of larger signal dropout in a few slices. The automated isolation of different laminae within dorsal horns was another possibility (Barry et al., 2014). A more recent human study of the spinal cord, however, did not observe significant differences between the two pairs (Eippert et al., 2016b), similar to what we have found here. As shown in the functional images and tSNR maps (Figure 21 and Table#1), dorsal horns in rats are relatively wide, and signal dropout is minimal. Our manual

selection of the dorsal horns also allows for consistent sampling in the laminae regions of the dorsal horns, and thus the presence of such bias is mitigated. From group analysis boxplots of different studies, specific horn-to-horn functional connectivity patterns within segments appears to vary across different species. For example, the functional connectivity between ventral and dorsal horns has been observed in squirrel monkeys while such connections are still speculative in humans (Barry et al., 2015; Eippert et al., 2016b). Similarly, in rats, ipsilateral dorsal and ventral connectivity was observed to have a weaker correlation strength but remains significant when compared to control regions. This within hemi-cord connectivity may be associated with sensorimotor functions such as reflexes that may be more pronounced in rodents than in humans. As Chen et al. pointed out, these differences can be associated with the functional organizations of different species (Chen et al., 2015). The use of more coordinated bilateral behaviors in rats and non-human primates may account for the differences in functional connectivity with humans. The use of anesthesia could also affect the differences with awake human studies. Rodent studies have demonstrated a loss of specificity in cortical regions with elevated anesthesia levels (Liu et al., 2013, 2011). However, this appears unlikely at the anesthesia level used in our current study (0.9-1.1%), and reports have shown early cortical regions are less affected by anesthesia. Thus, this effect would most likely be reduced in the downstream spinal cord.

### **3.5.8. Functional connectivity along the cervical spinal cord**

The segmental organization of the spinal cord allows for spatial somatotopic encoding of peripheral information. Our previous study found a bell-shaped spatial correlation profile across five slices that spanned from C4-C7 in ventral horns of NHPs: correlation values dropped from  $\sim r=0.85$  to  $\sim r=0.4$  and  $\sim r=0.3$  as we moved one and two slices away from the ROI seed slice respectively. Overall, functional connectivity across segments was constrained spatially within 2 spinal segments in NHPs (Chen et al., 2015). Our findings in rodents here indicate a similar trend between ventral-ventral or dorsal-dorsal horns, although larger decreases in correlation values were observed across slices in rodents. A possible explanation is that segments of the rodent spinal cord are thinner than those in NHPs so that a slice thickness of 3 mm may span 1-2 segments in rodents (Zhao et al., 2009a) but only 1 segment in NHPs (Chen et al., 2015; Florence et al., 1991; Qi et al., 2013). In humans, Kong et al. have also looked into correlations between segmental levels using an ICA approach, although no correlations between resting-state networks were reported

between slices (Kong et al., 2014). More recently, Liu and colleagues have also reported the presence of significant functional connectivity between vertebral levels and slices in the cervical spinal cord, although the majority of them were still located within vertebral levels as well as within slices. Moreover, amongst the ROI pairs that displayed significant correlations across spinal segments, most of them were also located within 1 segment away from the ROI, similar to what we have found in animal studies (Liu et al., 2016).

### **3.5.9. Improvements and future implications**

Although we have found robust connectivity between horns of the spinal cord, we can identify several limitations of this study and improvements that could be made. Firstly, our current study has focused mainly on within slice resting-state correlations. While Chen et al. have shown in monkeys the existence of such correlations and how they change before and after injuries, correlation strengths across slices appear to be weaker, consistent with what we have found here in rodents (Figure 26-27). Similarly, Kong et al. have also investigated correlation between segmental levels using an ICA approach, although no positive nor weak negative correlations were reported between resting-state networks at different spinal cord levels (Kong et al., 2014). This may be partly the result of the specific pre-processing protocol that was applied on a slice-by-slice basis (i.e. motion correction and regressions) that could reduce correlations between slices but also because correlations fall off between segments. Second, the smoothing with linear interpolation used in this study may have affected these correlations. However, the likely significance of this appears low as the amount of smoothing introduced was less than a voxel. Care was also taken when selecting ROIs of the horns of the spinal cord (Figure 32), and correlation maps in Figure 23 present strong correlations between distant voxels. Third, it is important to acknowledge that despite using a refined protocol for imaging the spinal cord, signal drop and distortions in BOLD images are still present especially on slices towards the edge (Figure 21) when compared to anatomical images. Fourth, the use of a 2-cm surface coil limits our field-of-view of the spinal cord. Ideally, measuring how resting-state functional connectivity varies along the entire length of the spinal cord could paint a more complete picture of ascending and descending features with rsfMRI. The use of a coil with greater coverage could be informative but might also introduce increased noise as well as motion artifacts related to respiratory movements. Thus, future

developments of imaging techniques would provide us with greater insights into the spinal functional architecture.

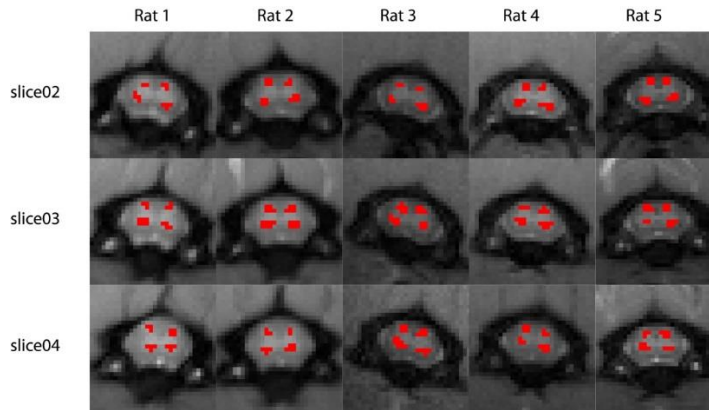


**Figure 32: Manual ROI selections (red) of gray matter spinal cord horns across the five rats.**

Rodents remain to be well suited for preliminary spinal cord injury studies (Cheriyana et al., 2014), so the use of rsfMRI may be valuable for monitoring their longitudinal recoveries from different manipulations. For example, cervical contusion models in rats have been studied and trends of how they recover behaviorally are well-documented (Pearse et al., 2005). Furthermore, current and investigational drugs as well as regenerative therapy (stem cells) can be introduced to test their effects on the central nervous system and recovery from injury. Another future study will be to extend these techniques to the lumbar spinal cord. Overall, the establishment of rsfMRI in spinal cord in rats may provide us with a robust and cost-effective model to evaluate and develop an effective biomarker for clinical diagnosis, drug development and quantitative monitoring of injuries.

### **3.5.10. Acknowledgements**

The author gratefully acknowledges Dr. Yue Zhou and Fuxue Xin for their assistance on animal preparation and Ken Wilkens for fine tuning the ventilator, as well as Dr. Robert L. Barry, Dr. Baxter Rogers and Benjamin Conrad for advices on analysis of spinal functional data. This specific study was supported by NIH grants NS078680 and NS092961.

### 3.6. References

- Bandettini, P.A., Wong, E.C., Hinks, R.S., Tikofsky, R.S., Hyde, J.S., 1992. Time course EPI of human brain function during task activation. *Magn. Reson. Med.* 25, 390–397.  
doi:10.1002/mrm.1910250220
- Barry, R.L., Rogers, B.P., Smith, S.A., Gore, J.C., 2015. Reproducibility of resting state spinal cord networks at 7 Tesla 23, 3708. doi:10.1016/j.neuroimage.2016.02.058
- Barry, R.L., Smith, S.A., Dula, A.N., Gore, J.C., 2014. Resting state functional connectivity in the human spinal cord. *Elife* 2014, 1–15. doi:10.7554/eLife.02812
- Behzadi, Y., Restom, K., Liau, J., Liu, T.T., 2007. A component based noise correction method (CompCor) for BOLD and perfusion based fMRI. *Neuroimage* 37, 90–101.  
doi:10.1016/j.neuroimage.2007.04.042
- Biswal, B., FZ, Y., VM, H., JS, H., 1995. - Functional connectivity in the motor cortex of resting human brain using. *Magn Reson Med* 34, 537–541. doi:10.1002/mrm.1910340409
- Boubela, R.N., Kalcher, K., Huf, W., Kronnerwetter, C., Filzmoser, P., Moser, E., 2013. Beyond Noise: Using Temporal ICA to Extract Meaningful Information from High-Frequency fMRI Signal Fluctuations during Rest. *Front. Hum. Neurosci.* 7, 168. doi:10.3389/fnhum.2013.00168
- Boyacioglu, R., Beckmann, C.F., Barth, M., 2013. An Investigation of RSN Frequency Spectra Using Ultra-Fast Generalized Inverse Imaging. *Front. Hum. Neurosci.* 7, 156.  
doi:10.3389/fnhum.2013.00156
- Brooks, J.C.W., 2014. Physiological noise modeling and analysis of spinal cord fMRI, in: Cohen-Adad, J., Wheeler-Kingshott, C. a. (Eds.), *Quantitative MRI of the Spinal Cord*. Academic Press, pp. 240–257.
- Chen, J.E., Glover, G.H., 2015. BOLD fractional contribution to resting-state functional connectivity above 0.1Hz. *Neuroimage* 107, 207–218. doi:10.1016/j.neuroimage.2014.12.012
- Chen, L.M., Mishra, A., Yang, P.-F., Wang, F., Gore, J.C., 2015. Injury alters intrinsic functional connectivity within the primate spinal cord. *Proc. Natl. Acad. Sci. U. S. A.* 112, 5991–6.  
doi:10.1073/pnas.1424106112
- Chen, L.M., Yang, P.-F., Wang, F., Mishra, A., Shi, Z., Wu, R., Wu, T.-L., Wilson III, G.H., Ding, Z., Gore, J.C., 2017. Biophysical and neural basis of resting state functional connectivity: Evidence from non-human primates. *Magn. Reson. Imaging* 39, 71–81. doi:10.1016/j.mri.2017.01.020
- Cheriyian, T., Ryan, D.J., Weinreb, J.H., Cheriyian, J., Paul, J.C., Lafage, V., Kirsch, T., Errico, T.J., 2014. Spinal cord injury models: a review. *Spinal Cord* 52, 588–595. doi:10.1038/sc.2014.91
- Coghill, R.C., Price, D.D., Hayes, R.L., Mayer, D.J., 1991. Spatial distribution of nociceptive processing in the rat spinal cord. *J. Neurophysiol.* 65, 133–140.

- Cohen-Adad, J., Gauthier, C.J., Brooks, J.C.W., Slessarev, M., Han, J., Fisher, J.A., Rossignol, S., Hoge, R.D., 2010. BOLD signal responses to controlled hypercapnia in human spinal cord. *Neuroimage* 50, 1074–1084. doi:10.1016/j.neuroimage.2009.12.122
- Conrad, B.N., Maki, S., Watchmaker, J.M., Box, B.A., Barry, R.L., Smith, A.S., Gore, J.C., 2017. BOLD signal changes in spinal cord with hypercapnia, in: *International Society for Magnetic Resonance in Medicine*.
- Ding, Z., Newton, A.T., Xu, R., Anderson, A.W., Morgan, V.L., Gore, J.C., 2013. Spatio-temporal correlation tensors reveal functional structure in human brain. *PLoS One* 8. doi:10.1371/journal.pone.0082107
- Ding, Z., Xu, R., Bailey, S.K., Wu, T.-L., Morgan, V.L., Cutting, L.E., Anderson, A.W., Gore, J.C., 2016. Visualizing functional pathways in the human brain using correlation tensors and magnetic resonance imaging. *Magn. Reson. Imaging* 34, 8–17. doi:10.1016/j.mri.2015.10.003
- Eippert, F., Kong, Y., Jenkinson, M., Tracey, I., Brooks, J.C.W., 2016a. Denoising spinal cord fMRI data: Approaches to acquisition and analysis. *Neuroimage*. doi:10.1016/j.neuroimage.2016.09.065
- Eippert, F., Kong, Y., Winkler, A.M., Andersson, J.L., Finsterbusch, J., Buchel, C., Brooks, J.C., Tracey, I., 2016b. Investigating resting-state functional connectivity in the cervical spinal cord at 3T. *bioRxiv* 1–30. doi:10.1101/073569
- Eippert, F., Kong, Y., Winkler, A.M., Andersson, J.L., Finsterbusch, J., Büchel, C., Brooks, J.C.W., Tracey, I., 2017. Investigating resting-state functional connectivity in the cervical spinal cord at 3 T. *Neuroimage* 147, 589–601. doi:10.1016/j.neuroimage.2016.12.072
- Florence, S.L., Wall, J.T., Kaas, J.H., 1991. Central projections from the skin of the hand in squirrel monkeys. *J. Comp. Neurol.* 311, 563–578. doi:10.1002/cne.903110410
- Fox, M.D., Greicius, M., 2010. Clinical applications of resting state functional connectivity. *Front. Syst. Neurosci.* 4, 19. doi:10.3389/fnsys.2010.00019
- Fox, M.D., Raichle, M.E., 2007. Spontaneous fluctuations in brain activity observed with functional magnetic resonance imaging. *Nat Rev Neurosci* 8, 700–711. doi:10.1038/nrn2201
- Gawryluk, J.R., Mazerolle, E.L., D’Arcy, R.C.N., 2014. Does functional MRI detect activation in white matter? A review of emerging evidence, issues, and future directions. *Front. Neurosci.* doi:10.3389/fnins.2014.00239
- Glover, G.H., Li, T.Q., Ress, D., 2000. Image-based method for retrospective correction of physiological motion effects in fMRI: RETROICOR. *Magn. Reson. Med.* 44, 162–167. doi:10.1002/1522-2594(200007)44:1<162::AID-MRM23>3.0.CO;2-E
- Gohel, S.R., Biswal, B.B., 2015. Functional integration between brain regions at rest occurs in multiple-frequency bands. *Brain Connect.* 5, 23–34. doi:10.1089/brain.2013.0210

- He, B.J., Snyder, A.Z., Zempel, J.M., Smyth, M.D., Raichle, M.E., 2008. Electrophysiological correlates of the brain ' s intrinsic large-scale functional architecture. *October* 105, 16039–16044.  
doi:10.1073/pnas.0807010105
- Hutchison, R.M., Everling, S., 2012. Monkey in the middle: why non-human primates are needed to bridge the gap in resting-state investigations. *Front. Neuroanat.* 6, 29. doi:10.3389/fnana.2012.00029
- Kalthoff, D., Seehafer, J.U., Po, C., Wiedermann, D., Hoehn, M., 2011. Functional connectivity in the rat at 11.7T: Impact of physiological noise in resting state fMRI. *Neuroimage* 54, 2828–2839.  
doi:10.1016/j.neuroimage.2010.10.053
- Kong, Y., Eippert, F., Beckmann, C.F., Andersson, J., Finsterbusch, J., Buchel, C., Tracey, I., Brooks, J.C., 2014. Intrinsically organized resting state networks in the human spinal cord. *Proc Natl Acad Sci U S A* 111, 18067–18072. doi:10.1073/pnas.1414293111
- Kornelsen, J., Stroman, P.W., 2007. Detection of the neuronal activity occurring caudal to the site of spinal cord injury that is elicited during lower limb movement tasks. *Spinal cord Off. J. Int. Med. Soc. Paraplegia* 45, 485–490. doi:10.1038/sj.sc.3102019
- Kwong, K.K., Belliveau, J.W., Chesler, D.A., Goldberg, I.E., Weisskoff, R.M., Poncelet, B.P., Kennedy, D.N., Hoppel, B.E., Cohen, M.S., Turner, R., 1992. Dynamic magnetic resonance imaging of human brain activity during primary sensory stimulation. *Proc. Natl. Acad. Sci. U. S. A.* 89, 5675–5679.  
doi:10.1073/pnas.89.12.5675
- Lawrence, J., Stroman, P.W., Bascaramurty, S., Jordan, L.M., Malisza, K.L., 2004. Correlation of functional activation in the rat spinal cord with neuronal activation detected by immunohistochemistry. *Neuroimage* 22, 1802–1807. doi:10.1016/j.neuroimage.2004.04.001
- Lee, H.L., Zahneisen, B., Hugger, T., LeVan, P., Hennig, J., 2013. Tracking dynamic resting-state networks at higher frequencies using MR-encephalography. *Neuroimage* 65, 216–222.  
doi:10.1016/j.neuroimage.2012.10.015
- Liu, X., Zhou, F., Li, X., Qian, W., Cui, J., Zhou, I.Y., Luk, K.D.K., Wu, E.X., Hu, Y., 2016. Organization of the intrinsic functional network in the cervical spinal cord: A resting state functional MRI study. *Neuroscience* 336, 30–38. doi:10.1016/j.neuroscience.2016.08.042
- Liu, X., Zhu, X.H., Zhang, Y., Chen, W., 2013. The change of functional connectivity specificity in rats under various anesthesia levels and its neural origin. *Brain Topogr.* 26, 363–377.  
doi:10.1007/s10548-012-0267-5
- Liu, X., Zhu, X.H., Zhang, Y., Chen, W., 2011. Neural origin of spontaneous hemodynamic fluctuations in rats under burst-suppression anesthesia condition. *Cereb. Cortex* 21, 374–384.  
doi:10.1093/cercor/bhq105
- Logothetis, N.K., Pauls, J., Augath, M., Trinath, T., Oeltermann, a, 2001. Neurophysiological

- investigation of the basis of the fMRI signal. *Nature* 412, 150–7. doi:10.1038/35084005
- Malisza, K.L., Jones, C., Gruwel, M.L.H., Foreman, D., Fernyhough, P., Calcutt, N.A., 2009. Functional magnetic resonance imaging of the spinal cord during sensory stimulation in diabetic rats. *J. Magn. Reson. Imaging* 30, 271–276. doi:10.1002/jmri.21856
- Malisza, K.L., Stroman, P.W., 2002. Functional imaging of the rat cervical spinal cord. *J. Magn. Reson. Imaging* 16, 553–558. doi:10.1002/jmri.10185
- Malisza, K.L., Stroman, P.W., Turner, A., Gregorash, L., Foniok, T., Wright, A., 2003. Functional MRI of the rat lumbar spinal cord involving painful stimulation and the effect of peripheral joint mobilization, in: *Journal of Magnetic Resonance Imaging*. pp. 152–159. doi:10.1002/jmri.10339
- Morel, P., 2016. *Gramm: grammar of graphics plotting for Matlab [Data set]*. Zenodo. doi:10.5281/zenodo.59786
- Niazy, R.K., Xie, J., Miller, K., Beckmann, C.F., Smith, S.M., 2011. Spectral characteristics of resting state networks. *Prog. Brain Res.* 193, 259–276. doi:10.1016/B978-0-444-53839-0.00017-X
- Niessing, J., Ebisch, B., Schmidt, K.E., Niessing, M., Singer, W., Galuske, R. a W., 2005. Hemodynamic signals correlate tightly with synchronized gamma oscillations. *Science* 309, 948–951. doi:10.1126/science.1110948
- Nir, Y., Mukamel, R., Dinstein, I., Privman, E., Harel, M., Fisch, L., Gelbard-Sagiv, H., Kipervasser, S., Andelman, F., Neufeld, M.Y., Kramer, U., Arieli, A., Fried, I., Malach, R., 2008. Interhemispheric correlations of slow spontaneous neuronal fluctuations revealed in human sensory cortex. *Nat. Neurosci.* 11, 1100–1108. doi:10.1038/nn.2177
- Ogawa, S., Lee, T., Kay, A., Tank, D., 1990. Brain magnetic resonance imaging with contrast dependent on blood oxygenation. *Proc. Natl. Acad. Sci. U. S. A.* 87, 9868–9872. doi:10.1073/pnas.87.24.9868
- Ogawa, S., Tank, D.W., Menon, R., Ellermann, J.M., Kim, S.G., Merkle, H., Ugurbil, K., 1992. Intrinsic signal changes accompanying sensory stimulation: functional brain mapping with magnetic resonance imaging. *Proc Natl Acad Sci U S A* 89, 5951–5955. doi:10.1073/pnas.89.13.5951
- Pearse, D.D., Lo, T.P., Cho, K.S., Lynch, M.P., Garg, M.S., Marcillo, a E., Sanchez, a R., Cruz, Y., Dietrich, W.D., 2005. Histopathological and behavioral characterization of a novel cervical spinal cord displacement contusion injury in the rat. *J. Neurotrauma* 22, 680–702. doi:10.1089/neu.2005.22.680
- Porszasz, R., Beckmann, N., Bruttel, K., Urban, L., Rudin, M., 1997. Signal changes in the spinal cord of the rat after injection of formalin into the hindpaw: characterization using functional magnetic resonance imaging. *Proc Natl Acad Sci U S A* 94, 5034–5039.
- Price, D.D., 1988. *Psychological and neural mechanisms of pain*. Raven Press, New York.
- Qi, H.X., Gharbawie, O.A., Wynne, K.W., Kaas, J.H., 2013. Impairment and recovery of hand use after

- unilateral section of the dorsal columns of the spinal cord in squirrel monkeys. *Behav. Brain Res.* 252, 363–376. doi:10.1016/j.bbr.2013.05.058
- Raj, D., Anderson, A.W., Gore, J.C., 2001. Respiratory effects in human functional magnetic resonance imaging due to bulk susceptibility changes. *Phys. Med. Biol.* 46, 3331–40.
- San Emeterio Nateras, O., Yu, F., Muir, E.R., Bazan, C., Franklin, C.G., Li, W., Li, J., Lancaster, J.L., Duong, T.Q., 2016. Intrinsic Resting-State Functional Connectivity in the Human Spinal Cord at 3.0 T. *Radiology* 279, 262–8. doi:10.1148/radiol.2015150768
- Shi, Z., Wu, R., Yang, P.-F., Wang, F., Wu, T.-L., Mishra, A., Chen, L.M., Gore, J.C., 2017. High spatial correspondence at a columnar level between activation and resting state fMRI signals and local field potentials. *Proc. Natl. Acad. Sci.* 201620520. doi:10.1073/pnas.1620520114
- Shreyas Harita, Stroman, P.W., 2017. Confirmation of resting-state BOLD fluctuations in the human brainstem and spinal cord after identification and removal of physiological noise. *Magn. Reson. Med.* doi:10.1002/mrm.26606
- Stroman, P.W., Bosma, R.L., Tsyben, A., 2012. Somatotopic arrangement of thermal sensory regions in the healthy human spinal cord determined by means of spinal cord functional MRI. *Magn. Reson. Med.* 68, 923–931. doi:10.1002/mrm.23292
- Stroman, P.W., Ryner, L.N., 2001. Functional MRI of motor and sensory activation in the human spinal cord. *Magn. Reson. Imaging* 19, 27–32. doi:10.1016/S0730-725X(01)00226-0
- Stroman, P.W.W., Wheeler-Kingshott, C. a., Bacon, M., Schwab, J.M.M., Bosma, R., Brooks, J., Cadotte, D.W., Carlstedt, T., Ciccarelli, O., Cohen-Adad, J., Curt, A., Evangelou, N., Fehlings, M.G.G., Filippi, M., Kelley, B.J.J., Kollias, S., Mackay, A., Porro, C.A. a., Smith, S., Strittmatter, S.M.M., Summers, P., Tracey, I., Stroman, P.W.W., Schwab, J.M.M., Bacon, M., Bosma, R., Brooks, J., Cadotte, D.W., Carlstedt, T., Ciccarelli, O., Cohen-Adad, J., Curt, A., Fehlings, N.E.M.G., Filippi, M., Kelley, B.J.J., Kollias, S., Mackay, A., Porro, C.A. a., Smith, S., Strittmatter, S.M.M., Summers, P., Thompson, A.J., Tracey, I., Evangelou, N., Fehlings, M.G.G., Filippi, M., Kelley, B.J.J., Kollias, S., Mackay, A., Porro, C.A. a., Smith, S., Strittmatter, S.M.M., Summers, P., Thompson, A.J., Tracey, I., Wheeler-Kingshott, C. a., Bacon, M., Schwab, J.M.M., Bosma, R., Brooks, J., Cadotte, D.W., Carlstedt, T., Ciccarelli, O., Cohen-Adad, J., Curt, A., Evangelou, N., Fehlings, M.G.G., Filippi, M., Kelley, B.J.J., Kollias, S., Mackay, A., Porro, C.A. a., Smith, S., Strittmatter, S.M.M., Summers, P., Tracey, I., Stroman, P.W.W., Schwab, J.M.M., Bacon, M., Bosma, R., Brooks, J., Cadotte, D.W., Carlstedt, T., Ciccarelli, O., Cohen-Adad, J., Curt, A., Fehlings, N.E.M.G., Filippi, M., Kelley, B.J.J., Kollias, S., Mackay, A., Porro, C.A. a., Smith, S., Strittmatter, S.M.M., Summers, P., Thompson, A.J., Tracey, I., 2014. The current state-of-the-art of spinal cord imaging: Applications. *Neuroimage* 84, 1082–1093. doi:10.1016/j.neuroimage.2013.04.124

- Vincent, J.L., Patel, G.H., Fox, M.D., Snyder, A.Z., Baker, J.T., Van Essen, D.C., Zempel, J.M., Snyder, L.H., Corbetta, M., Raichle, M.E., 2007. Intrinsic functional architecture in the anaesthetized monkey brain. *Nature* 447, 83–86. doi:10.1038/nature05758
- Wang, L., Saalmann, Y.B., Pinsk, M.A., Arcaro, M.J., Kastner, S., 2012. Electrophysiological Low-Frequency Coherence and Cross-Frequency Coupling Contribute to BOLD Connectivity. *Neuron* 76, 1010–1020. doi:10.1016/j.neuron.2012.09.033
- Wang, Z., Chen, L., Négyessy, L., Friedman, R., Mishra, A., Gore, J., Roe, A., 2013. The Relationship of Anatomical and Functional Connectivity to Resting-State Connectivity in Primate Somatosensory Cortex. *Neuron* 78, 1116–1126. doi:10.1016/j.neuron.2013.04.023
- Wei, P., Li, J., Gao, F., Ye, D., Zhong, Q., Liu, S., 2010. Resting state networks in human cervical spinal cord observed with fMRI. *Eur J Appl Physiol* 108, 265–271. doi:10.1007/s00421-009-1205-4
- Wilson, G.H., Yang, P.F., Gore, J.C., Chen, L.M., 2016. Correlated inter-regional variations in low frequency local field potentials and resting state BOLD signals within S1 cortex of monkeys. *Hum. Brain Mapp.* 37, 2755–2766. doi:10.1002/hbm.23207
- Wu, C.W., Gu, H., Lu, H., Stein, E.A., Chen, J.H., Yang, Y., 2008. Frequency specificity of functional connectivity in brain networks. *Neuroimage* 42, 1047–1055. doi:10.1016/j.neuroimage.2008.05.035
- Yang, P.-F., Wang, F., Chen, L.M., 2015. Differential fMRI Activation Patterns to Noxious Heat and Tactile Stimuli in the Primate Spinal Cord. *J. Neurosci.* 35, 10493–10502. doi:10.1523/JNEUROSCI.0583-15.2015
- Zhao, F., Williams, M., Meng, X., Welsh, D.C., Coimbra, A., Crown, E.D., Cook, J.J., Urban, M.O., Hargreaves, R., Williams, D.S., 2008. BOLD and blood volume-weighted fMRI of rat lumbar spinal cord during non-noxious and noxious electrical hindpaw stimulation. *Neuroimage* 40, 133–147. doi:10.1016/j.neuroimage.2007.11.010
- Zhao, F., Williams, M., Meng, X., Welsh, D.C., Grachev, I.D., Hargreaves, R., Williams, D.S., 2009a. Pain fMRI in rat cervical spinal cord: An echo planar imaging evaluation of sensitivity of BOLD and blood volume-weighted fMRI. *Neuroimage* 44, 349–362. doi:10.1016/j.neuroimage.2008.09.001
- Zhao, F., Williams, M., Welsh, D.C., Meng, X., Ritter, A., Abbadie, C., Cook, J.J., Reicin, A.S., Hargreaves, R., Williams, D.S., 2009b. fMRI investigation of the effect of local and systemic lidocaine on noxious electrical stimulation-induced activation in spinal cord. *Pain* 145, 110–119. doi:10.1016/j.pain.2009.05.026

## **Chapter 4: LONGITUDINAL ASSESSMENT OF SPINAL CORD INJURY WITH MULTIPARAMETRIC QUANTITATIVE MRI**

### **4.1. Abstract**

Spinal cord injuries (SCIs) are a leading cause of disability and can severely impact the quality of life for individuals. However, to date, the process of spontaneous repair of damaged spinal remains incompletely understood partly due to a lack of appropriate longitudinal tracking methods. Non-invasive, multi-parametric MRI provides potential biomarkers for comprehensive evaluation of the spontaneous repair of SCI. In this study, a clinically relevant contusion injury model was introduced at the lumbar level in rodents. In parallel, quantitative MRI measures in rodents at baseline and those inflicted with SCI were acquired. Specifically, the progression of injury in white matter tracts within two weeks were tracked longitudinally using pool-size ratio (PSR) derived from quantitative magnetization transfer (qMT) methods along with diffusion metrics, while functional integrity of spinal gray matter was assessed using rsfMRI at 24-hours post SCI. We found (1) a progressive decrease in PSR values within two weeks post-SCI, which was validated with histology, (2) PSR correlated closely with fractional anisotropy and transverse relaxation of the free water pool but interestingly showed insignificant correlations with behavioral recoveries, (3) SCI induced an increase and decrease in functional connectivity above and below the injury site respectively, and (4) within-slice patterns of functional connectivity between ROIs were similar regardless of position relative to the injury site. Findings from this study not only confirm the value of qMT methods for assessing the myelination state of injured spinal cord, but may also have further implications on whether therapies targeted towards remyelination, which remain contentious, may be appropriate. Additionally, better understanding of functional organization of the healthy lumbar spinal cord as well as changes after injury provides valuable information for innovative ideas of interventions, and for directing the use of fMRI in clinical prognosis.

### **4.2. Introduction – DTI, qMT, FMRI**

Spinal cord injuries (SCIs) are a leading cause of disability and can lead to devastating physiological consequences for patients. To date, complete restorative therapies for SCIs have yet

to be devised, and the development of spontaneous repair of damaged spinal cord remains poorly understood partly due to a lack of appropriate longitudinal monitoring methods. It is generally accepted that SCI induces an initial phase of primary injury, during which spinal tissues are lost while conduction along white matter tracts and gray matter functions are disrupted (Ju et al., 2014). Consequently, this triggers a cascade of pathological events, termed secondary injury, which typically involves the formation of glial scars made up of reactive astrocytes (Fawcett and Asher, 1999), loss of oligodendrocytes (Casha et al., 2001; Kim et al., 2003), as well as inflammatory responses mediated by microglia and macrophages (Chan, 2008; Hawthorne and Popovich, 2011). Given its complex dynamics, the development of viable biomarkers that are sensitive to the spinal cord's spontaneous recovery process could be critical for determining the optimal time window, targets and effectiveness of therapeutic interventions.

Quantitative MRI presents an attractive technique for revealing microstructural integrity non-invasively beyond conventional methods at the spinal level. Notably, diffusion tensor imaging (DTI) exploits anisotropy of water motion in white matter fibers (Horsfield and Jones, 2002; Stejskal and Tanner, 1965), and has previously been used to deduce fiber organization in both the brain and spinal cord. Specifically, variations in indices such as axial (IADC) and radial (tADC) diffusivity values have previously been shown to reflect axonal damage and demyelination respectively. Similarly, fractional anisotropy (FA) and apparent diffusion coefficient (ADC) encompass broader information on microstructure including cell density, axonal density, fiber coherence and myelination (Vedantam et al., 2014). Importantly, studies have also demonstrated that DTI can successfully predict various grades of injury severity at different time points (Li et al., 2015; Loy et al., 2007).

Another attractive quantitative MR method capable of tracking SCI repair is magnetization transfer (MT) imaging. Specifically, the MT effect exploits communications between macromolecular and free water protons – chemical exchange or dipole-dipole interactions – to indirectly measure immobile macromolecular content (Wolff and Balaban, 1989). As an indirect marker for myelination, the MT effect has been shown in several studies to reveal demyelination under different pathological conditions, which has been confirmed with histology (Deloire-Grassin et al., 2000; Schmierer et al., 2004). In general, the contrast detected in MT is often characterized with two different metrics: MT ratio (MTR) and quantitative MT (qMT). While MTR is more widely used, it is also sensitive to various non-MT effects (Henkelman et al., 1993). Hence, more

specific qMT methods have been developed to tease out intrinsic MT parameters for isolating pool size ratio (PSR) from relaxation and exchange rates (Gochberg and Gore, 2003; Henkelman et al., 1993).

While DTI and qMT convey information about white matter microstructure, functional integrity of spinal gray matter circuits can be evaluated non-invasively with functional MRI (fMRI). fMRI detects blood oxygenation level dependent (BOLD) contrast and has been extensively applied in the brain to study functional connectivity under both stimulus-evoked and resting-state conditions (Gore, 2003; van den Heuvel and Hulshoff Pol, 2010). Recently, resting-state fMRI appears to reveal robust connectivity between spinal horns in awake humans (Barry et al., 2014) and in anesthetized animals (Chen et al., 2015). The translation of rsfMRI to monitoring the spinal cord after SCI would provide complementary information to DTI and qMT methods.

In this study, multi-parametric MRI acquisitions (DTI, qMT and fMRI) were acquired in healthy control rats as well as in rats that have underwent a moderate contusion injury at the lumbar level. Specifically, progression and recovery of the injury in white matter tracts were tracked longitudinally with DTI and qMT, while quantitative behavioral assessments and histological sections with myelin stain were collected in parallel. Moreover, functional integrity of spinal gray matter was also assessed by first translating rsfMRI to healthy lumbar spinal cord, and then assessing functional connectivity changes within segments of spine above and below the injury site 24 hours (hrs) post injury. In the context of recent developments, a better understanding of the spontaneous repair processes and baseline states of spinal cord structure and function can be instrumental for designing effective therapeutic interventions and for evaluating treatment outcomes.

### **4.3. Methods**

#### **4.3.1. Animal surgical procedures**

A total of 19 male Sprague Dawley rats were included in this study. A subset of the rats (13 rats) underwent SCI, and were initially anesthetized with 3% isoflurane before a midline sagittal incision of about 5-6 cm was made over the lumbar vertebrae. Muscle and connective tissues were subsequently removed to expose the underlying vertebral spinal column segments.

Dorsal laminectomy was then performed using a fine tipped rongeur for removing vertebral processes. A typical opening measured up to 3 mm of the spinal cord, larger than the 2.5 mm diameter of an impactor tip. The Infinite Horizon Impactor – a device designed for the application of standard force injuries to the spinal cord of rodents – was used in this study. With the exposed spinal cord, two Adson forceps were used to clamp and rigidly secure the vertebral spinal column. This was done by securing the transverse processes of the vertebral spinal column approximately 1 mm rostral and caudal to the laminectomy. The impact was initiated at a moderate injury level (160 kDynes) at the L2 segment. Postoperative wound closure was completed by apposing and suturing the dissected muscle. Post-operative care included the administration of analgesics (5-15 mg/kg carprofen) and manual expression of bladder whenever necessary.

#### **4.3.2. Animal Preparation**

Before MRI scans, animals were first anesthetized with 3% isoflurane and underwent endotracheal intubation followed by mechanical ventilation. Ventilation rate was initially set between 70-75 breaths/min before being gradually lowered as the animal stabilized. Vital signs of the animals were continuously monitored throughout each session, which included respiratory pattern using a pneumatic pillow, rectal temperature and end tidal CO<sub>2</sub>. Respiratory traces were also recorded and saved in order to correct their effects on BOLD signals. Animals were then placed on a customized bed in the supine position with an elastic strap tightened around the animal and coil. At least an hour was allocated for each animal to stabilize physiologically, during which shimming (automatic global shimming followed by local shimming over the spinal cord) was performed before power calibration on a single coronal slice covering the dorsal column. Subsequently, anatomical, DTI and qMT images were acquired before fMRI acquisitions, during which animals' anesthesia level were gradually lowered to between 0.9-1.1% with ventilation rate set at 60 breaths/min. All experimental procedures were approved by Vanderbilt University's Institutional Animal Care and Use Committee.

#### **4.3.3. Image Acquisition**

All MR images were acquired on a 9.4T Varian magnet with a 2-cm diameter transmit-receive radio frequency coil. Anatomical images were acquired with MT contrast using a gradient echo sequence that incorporates a Gaussian radio frequency saturation pulse offset at 5000Hz and

flip angle of  $820^\circ$  from water (TR/TE=200/3ms, matrix size=128x128, FOV=32x32 mm<sup>2</sup>, slice thickness = 3 mm (axial), 0.50 mm (coronal) and 0.75 mm (sagittal), flip angle=35°). These high resolution images were referenced for slice selection that captured the dorsal column at the site of the lesion for subsequent quantitative MRI.

Diffusion weighted images were acquired using a respiratory-gated pulsed gradient spin-echo EPI imaging sequence with the following acquisition parameters: TR/TE=2000/27.61ms, number of excitations (NEX)=8, 333x333x700 $\mu\text{m}^3$ , 12 directions, b-values of 0 and 1000 s/mm<sup>2</sup>, diffusion gradient amplitude=28.13 G/cm, duration=4.00ms, separation=12ms. Five coronal slices were collected with the second slice covering the posterior position of the spinal cord with the dorsal column and dorsal horns.

qMT images were acquired with the following parameters: TR/TE=28/2.97ms, NEX=32, 250x250x700  $\mu\text{m}^3$  with the same acquisition plane as the second slice of DTI. Slice-selective Gaussian-shaped saturation pulses at two different powers were applied (flip angle=220° and 820°) with eight different frequency offsets ranging from 1000 Hz to 80000 Hz at constant logarithmic interval with an additional data point acquired at 6000 Hz. While previous brain imaging has suggested minimal RF offsets (Cercignani and Alexander, 2006; Ramani et al., 2002; Wang et al., 2015), pronounced motion artifacts in the spinal cord may require additional data points especially for accurate pixel-by-pixel fitting. T<sub>1</sub> maps were also acquired to obtain averaged observed relaxation rate  $R_{1\text{obs}}$  in healthy controls using an inversion recovery sequence (Figure 33).

fMRI in the lumbar spinal cord was acquired using a similar protocol as our previous publication (Wu et al., 2017): TR/TE=500/6.70ms, 6 shots, resolution=0.33x0.33x3 mm<sup>3</sup>, 180 volumes. A relatively short echo time was selected to reduce distortions and signal losses caused by field inhomogeneities. Five transverse slices were acquired with the center slice placed at the epicenter of the injury.

Longitudinally, DTI and qMT scans were performed at 6 hrs, 24 hrs, week-1 and week-2 post-SCI. In order to image the same region across sessions, local fiducial landmarks including nerve bundles, and gray and white matter were used as reference points.

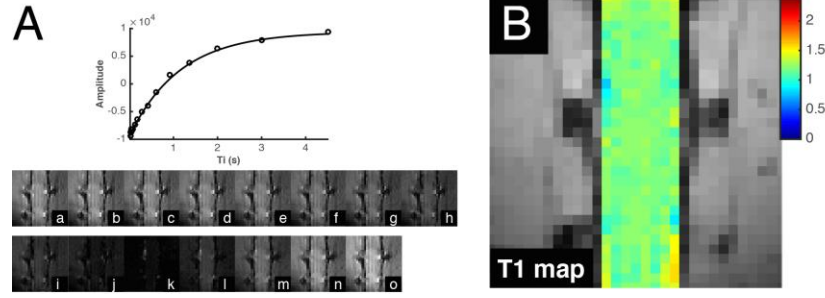


**Figure 33: T1 measurement of the rat spinal cord.** (A, top) Inversion recovery profile with fitted curve of the rat lumbar spinal cord as a function of multiple inversion times ( $T_i$ ) in a representative voxel. (A, bottom) Raw images of the spinal cord at multiple  $T_i$ 's with a-o subplots corresponding to 0.017, 0.0253, 0.0377, 0.0562, 0.0837, 0.125, 0.186, 0.277, 0.420, 0.614, 0.914, 1.36, 2, 3, and 4.5 seconds respectively. (B) T1 map obtained from one representative rat overlaid on anatomical image. Averaged T1 across three rats were computed to be  $1.28 \pm 0.02$ s (mean  $\pm$  standard error of mean). Inversion recovery images were acquired with a spin-echo EPI pulse sequence: TR/TE=5000/10.89ms, 4 averages, 64x64 matrix size, 32x32mm<sup>2</sup> field of view.

#### 4.3.4. MRI data analyses

MRI data analyses were performed using MATLAB 2015a. Similar to our previous publication (Wang et al., 2015), qMT data were fit using the Henkelman-Ramani model (Ramani et al., 2002). Using a two-pool model, MT-weighted MR signals collected were expressed as a function of irradiation amplitudes of continuous wave power equivalent ( $\omega_{CWPE}$ ), which is proportional to the square of the flip angles ( $\theta_{sat}$ ) of the saturation pulse, and at multiple frequency offsets ( $\Delta f$ ) using:

$$S(\omega_{CWPE}, \Delta f) = \frac{M_0 \left( R_{1b} \left[ \frac{RM_{0b}}{R_{1a}} \right] + R_{RFB}(\omega_{1CWPE}, \Delta f, T_{2b}) + R_{1b} + \frac{RM_{0b}}{F} \right)}{\left[ \frac{RM_{0b}}{R_{1a}} \right] (R_{1b} + R_{RFB}(\omega_{1CWPE}, \Delta f, T_{2b})) + \left( 1 + \left[ \frac{\omega_{CWPE}}{2\pi\Delta f} \right]^2 \left[ \frac{1}{T_{2a}R_{1a}} \right] \right) (R_{RFB}(\omega_{1CWPE}, \Delta f, T_{2b}) + R_{1b} + \frac{RM_{0b}}{F})} \quad (34)$$

Subscripts  $a$  and  $b$  in Equation 34 denote free water and macromolecular protons respectively.  $F$ , also known as the pool size ratio (PSR), represents the ratio of free water and macromolecular pool ( $M_{0b}/M_{0a}$ ) and has been linked to indirectly indicate myelin content;  $M_{0a}$  and  $M_{0b}$  represent the fully relaxed values of magnetization in their respective pools. In addition,  $M_0$  is the magnetization signal without MT contrast while  $R_{RFB}$  is the rate of saturation of the macromolecular pool and is dependent on  $\omega_{CWPE}$ ,  $\Delta f$ , and transverse relaxation  $T_{2b}$ . Conventional notations of  $R_{1a}$  ( $1/T_{1a}$ ) and  $R_{1b}$  ( $1/T_{1b}$ ) are the longitudinal relaxation rates for protons in the respective proton pools.  $R_b$  was also set as a constant at  $1s^{-1}$  while  $R_{1a}$  is dependent on the observed longitudinal relaxation rate ( $R_{1obs}$ ) and was included in model as:

$$R_{1a} = R_{1obs} - \frac{RM_{0b}(R_{1b}-R_{1obs})}{R_{1b}-R_{1obs} + \frac{RM_{0b}}{F}} \quad (35)$$

With qMT data fitted to the above model, five parameters were estimated for each pixel:  $M_0$ ,  $F$ ,  $RM_{0b}$ ,  $T_{2A}$  and  $T_{2b}$ . Figure 34F presents an example of the fitted model to normalized signals obtained from a selected white matter voxel in the spinal cord at two saturation powers and multiple frequency offsets. Performance of the model fitting was also estimated by assessing squared 2-norm of the residuals.

Pearson's correlation coefficients were also computed between PSR maps and (1) other fitted PSR parameters –  $R_{2a}$ ,  $R_{2b}$  and  $RM_{0b}$ , (2) diffusion metrics, (3) behavioral assessments, and (4) histological myelin stains. Statistical comparisons between PSR values at different time points were also performed using non-parametric Wilcoxon rank sum tests corrected for multiple comparisons.

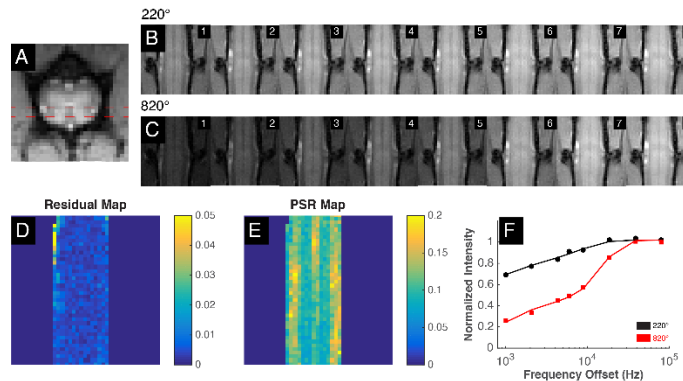


**Figure 34: QMT acquisition and analysis for healthy lumbar spinal cord.** (A) High resolution axial MTC image with red dashed lines indicating coronal acquisition plan covering dorsal horns and the dorsal column. (B-C) Cropped raw qMT data collected at eight different frequency offsets and at two flip angles of 220° and 820° respectively. (D-E) Square 2-norm of residuals and PSR map from qMT model fitting. (F) Curves of normalized intensity in selected white matter voxel with fitted model curves for 220° and 820° represented as black and red colors respectively.

#### 4.3.5. Histological Staining

At different time points after the injury, rats were euthanized with an overdose of isoflurane. Perfusion was subsequently performed with PBS/saline solution followed by 10% paraformaldehyde fixation. Rat spinal cords were excised and soaked in paraformaldehyde. Histological stain with Luxol Fast Blue (LFB) of post-mortem tissue was then performed to

evaluate the extent of demyelination due to the contusion lesion. Specifically, sections 10  $\mu\text{m}$  thick were first sliced in the coronal orientation, and were de-waxed and cleared in 95% ethanol. Slides were subsequently stained in LFB solution overnight between 56 to 58 degrees Celsius. Sections were then rinsed in 95% alcohol for removing excess stain before rinsing with distilled water. Differentiation was then performed by immersing the slides in lithium carbonate solution for 10 seconds followed by placing them in 70% ethanol until gray matter and white matter were distinguishable. Optical intensity changes on myelin stains at the regions of interest were quantitatively evaluated where the degree of de-myelination and afferent disruption were assessed by the percentage decrease of the regional intensity relative to control regions similar to procedures described in Janve et al. (Janve et al., 2013).

#### **4.3.6. Behavioral assessments**

Behavioral deficits after SCIs were quantified with locomotor measurements, Von Frey tests and hot plate response latencies. Before performance of any behavioral tests, rats were first habituated for at least 45 minutes. For locomotor activity assessments, each rat was transferred to an individual open field chamber for 30 minutes. Any movements in the chamber would result in breaking of invisible infrared beams, which were recorded as measurements of activity. Vertical activity levels such as rearing behaviors, however, were not recorded.

Manual Von Frey assessments were performed to evaluate mechanical allodynia in rats. Specifically, each rat was placed individually in a clear cage with penetrable mesh wired floor. Monofilaments of various strengths (2g, 4g, 6g, 8g, 10g and 15g) were applied perpendicular to the hind paw 10 times. A positive response was recorded if the rat withdrew, licked or shook their paw either during the application or after withdrawal of the filament. For rats that had undergone SCIs, filament strength up to 26g was also applied and if unresponsive, three times the filament strength at 78g was recorded as the filament threshold. Due to paralysis and dragging motion of the hindlimbs, Von Frey tests were performed in the animals' own home cages without a mesh wire bottom. Both locomotor and Von Frey tests were performed at baseline, 24 hrs, week-1 and week-2 time points.

Finally, hot plate tests were carried out by placing an unrestrained rat onto a metal surface at a constant temperature of 55 degrees Celsius. Hind paw withdrawal or licking were indicative of a response, and the time to elicit such responses was recorded. Because analgesics were

administered post-SCI injury, hot plate tests were performed only at baseline, week-1 and week-2 time points.

## 4.4. Results

### 4.4.1. PSR and FA Revealed Changes at the Injury Site in the Lumbar Spinal Cord

In healthy control rats, MT saturated images revealed reasonable contrast between white and gray matter of the spinal cord. Specifically, gray matter appears to have greater signal intensity than that of white matter (Figure 34). PSR maps also reveal greater values in white matter ( $0.124 \pm 0.007$ ) than that of gray matter ( $0.087 \pm 0.004$ ). These spinal qMT *in vivo* measurements are the first to have been recorded at the lumbar level in rodents and are comparable in range to those obtained in white matter and gray matter of the brain (Cercignani and Alexander, 2006; Cercignani and Barker, 2008) and in the cervical spinal cord of NHPs (Wang et al., 2015). In all SCI animals, PSR and FA maps revealed lesion related changes. QMT spectra obtained at two flip angles, which were normalized to signal intensities at 80 kHz, are displayed in Figure 35C. Compared to healthy control PSR maps, post-lesion PSR maps identified a low PSR region (indicated by the red arrows) which were reflected in parallel in the FA maps. Specifically, PSR and FA values reduced to 40% and 31% of controls at the injury site 24-hours post-SCI as shown in Figures 35A-B.

### 4.4.2. Longitudinal PSR changes with injury and correlations with other MR metrics

Dynamic changes of PSR and FA at different time points of the injury averaged over multiple runs at each time point are shown in Figure 36. The PSR at the epicenter of the injury was low beyond 24 hours ( $p < 0.05$ , corrected) and continued to diminish over time, presenting an overall decreasing trend. Similarly, FA measurements decreased within 24 hours. However, signs of recovery were evident at week-1 and week-2 with increased FA values, although care must be taken with such interpretation given the gradual clearance of edema and inflammation after the first week (see *Limitations and Improvements* in Section 4.5). In order to understand the relationship between PSR and other MR metrics sensitive to demyelination and macromolecular content, Pearson's correlations were computed between them for both control and SCI rats.

Specifically, MT parameters including relaxation rates of both pools and exchange rate were plotted against PSR in Figure 37. DTI derived metrics – FA, ADC, IADC, and tADC – were also plotted as a function of PSR. While some overlaps exist between control and SCI rats, distinct clusters are noticeable between controls and injured groups. Quantitatively, FA ( $r=0.59$ ,  $p=2.25 \times 10^{-4}$ ) and  $R_{2a}$  ( $r=0.67$ ,  $p=9.28 \times 10^{-6}$ ) presented significant positive correlations while ADC ( $r=-0.08$ ,  $p=0.65$ ) and axial diffusivity ( $r=0.12$ ,  $p=0.50$ ) were most weakly coupled with PSR.

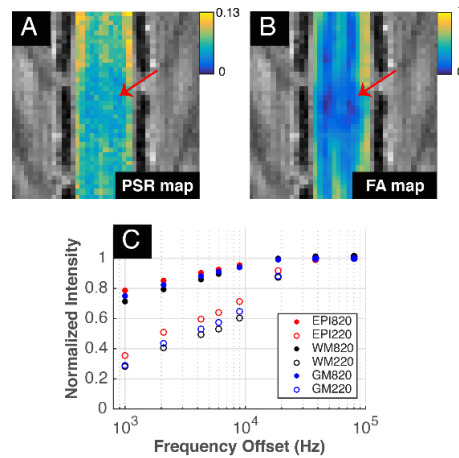


**Figure 35: PSR and FA maps with MT curve post-SCI.** (A) PSR and (B) FA maps 24 hours post-SCI. Red arrows indicate epicenter of the injury. (C) ROIs were drawn at the epicenter (red) as well as at unaffected gray (blue) and white (black) matter. MT spectra of these ROIs at flip angles  $220^\circ$  (unfilled) and  $820^\circ$  (filled) are displayed.

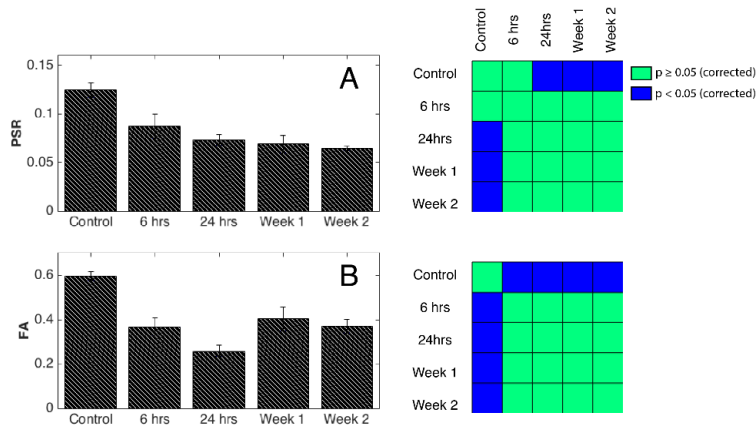


**Figure 36: Longitudinal assessments of the injury.** (A, left) Averaged PSR values for controls and different time points of the injury at 6 hours, 24 hours, week 1 and week 2 with  $n=5, 7, 9, 7, 5$  observations respectively. (A, right) Non-parametric Wilcoxon rank sum tests between different time points of the injury. Blue and green voxels represent injury. Blue and green voxels represent corrected p-values greater than or equal to 0.05 and less than 0.05 respectively. Likewise, (B, left) averaged FA values along with (B, right) statistical comparisons were computed from runs at different time points of the injury.

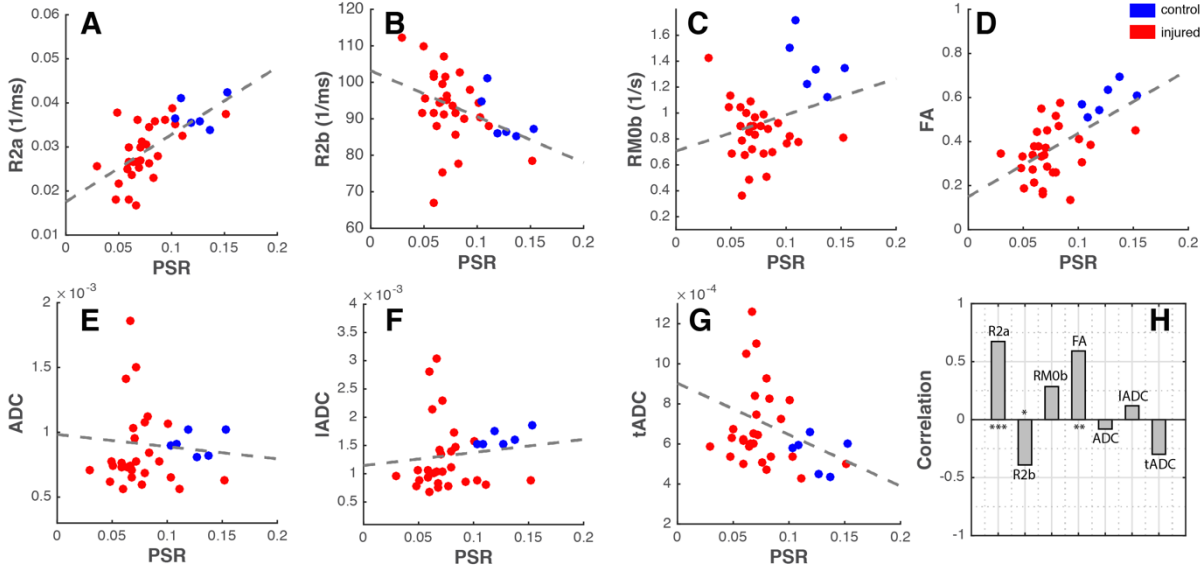


**Figure 37: Comparisons of PSR and other MRI parameters.** (A-G) Plots of R<sub>2a</sub>, R<sub>2b</sub>, RM<sub>0b</sub>, FA, ADC, IADC and tADC as a function of PSR. Dotted lines indicate linear fits for each plot while blue and red dots represent pre- and post-SCI respectively. (H) Correlation between PSR and respective MRI parameters. \*\*\*p<0.00005, \*\*p<0.0005, and \*p<0.05.

#### 4.4.3. Relationship between PSR, FA and behavioral assessments

Longitudinal changes of PSR were also correlated with behavioral assessments (Figure 38). For both Von Frey and locomotor activity evaluations, the greatest deficits were observed at 24 hours post-SCI. Specifically, Von Frey tests showed rats were largely unresponsive to filament strengths up to 26g while open-field tests showed 37% drop in locomotor activity. At weeks 1 and 2, however, diminishing mechanical withdrawal thresholds as well as increasing locomotor activities suggest progressive functional recoveries, which is further supported by weaker statistical comparisons when compared to controls as a function of time. Similarly, hot plate assay showed impairments to pain detection at week-1 with a greater latency response time, but recovery was evident at week-2. Comparisons of behavioral measurements with the decreasing PSR trend, however, showed insignificant correlations:  $r_{\text{vonfrey-PSR}} = -0.69$  (p=0.31),  $r_{\text{locomotor-PSR}} = 0.79$  (p=0.21), and  $r_{\text{hotplate-PSR}} = -0.49$  (p=0.68). On the other hand, correspondences between FA and behavioral measurements demonstrated greater correlations as signs of recovery or increased FA were present at week-1 and week-2:  $r_{\text{vonfrey-FA}} = -0.89$  (p=0.11),  $r_{\text{locomotor-FA}} = 0.92$  (p=0.08), and  $r_{\text{hot plate-FA}} = -0.42$  (p=0.72).

#### 4.4.4. Validation of PSR and FA with histology

LFB was used to stain for myelin and validate measurements obtained from PSR maps. Figure 39 presents LFB stained sections at the dorsal column from rats obtained at baseline, 24-hours, week-1 and week-2 post-SCI. Distinct white and gray matter contrast is evident with stains mostly restricted to white matter (yellow and purple arrows). At 24 hours, LFB staining was reduced with more granular staining visible (reduced to  $36.68 \pm 0.05\%$  of controls). Consistent with the PSR trend, little of the tissue at the epicenter with positive stains for LFB was evident at week-2 post SCI (reduced to  $17.50 \pm 0.01\%$  of controls). Moreover, correlation of LFB measurements with PSR ( $r=0.9956$ ,  $p=0.004$ ) was significantly greater than that with FA ( $r=0.7961$ ,  $p=0.2039$ ) as expected.

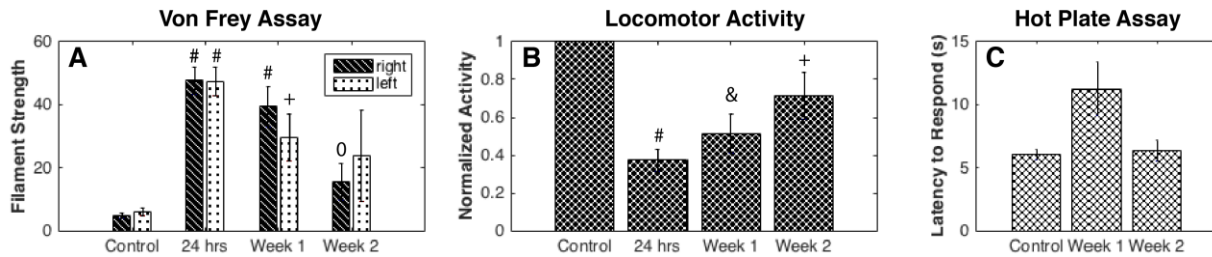


**Figure 38: Behavioral assessments post-SCI.** (A) Threshold filament forces that caused positive responses through either withdrawing or licking with the Von Frey test are displayed at different time points post-SCI. (B) Normalized locomotor activity assessed with the number of beam breaks in an open field chamber. (C) Latency to respond on a hot plate assay at 55 degrees Celsius were recorded. Non-parametric Wilcoxon-rank sum test were performed relative to their respective baselines. <sup>#</sup> $p < 0.0005$ , <sup>&</sup> $p < 0.005$ , <sup>+</sup> $p < 0.01$ , and <sup>0</sup> $p < 0.05$ .

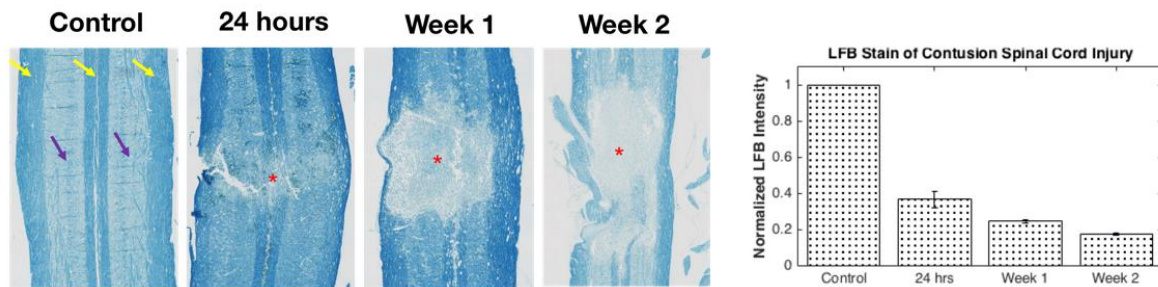


**Figure 39: LFB stains of the spinal cord at different time points post SCI.** (Left) Controls, 24-hours, Week-1 and Week-2 time points of the spinal cord were stained for myelin using Luxol Fast Blue. Yellow and purple arrows point to gray and white matter regions that are indicated by weaker and more intense stains respectively. Red asterisks indicate epicenter of the injury with de-myelination are present. (Right) Histogram of normalized LFB intensity of the injury site relative to control regions unaffected by the injury.

#### 4.4.5. RsfMRI patterns in the lumbar spinal cord

Evaluations of resting-state BOLD images and time series at the lumbar level were first performed in healthy control rats. Figure 40 presents acquisition planes of a representative rat lumbar spinal cord with MTC and corresponding BOLD images. Functional images at the lumbar level provided adequate contrast to distinguish between gray and white matter tissues. In addition, BOLD and anatomical images appear to be well-aligned, indicated by a red cross hair pointing to the right dorsal horn on both images at the same position. Figure 41 presents averaged time series of the four horns with signal fluctuations similar to those found at the cervical level in humans, NHPs and rats. Furthermore, resting-state functional connectivity maps reveal intrinsic functional connectivity patterns between the spinal horns. Specifically, seed voxels placed in the dorsal horns resulted in relatively strong correlations to the corresponding contralateral dorsal horn (Figure 42). Likewise, placing seeds in the ventral horns produced a similar result. This functional connectivity pattern was indeed consistent across animals, and similar to the ones found at the cervical level and in other species as well.

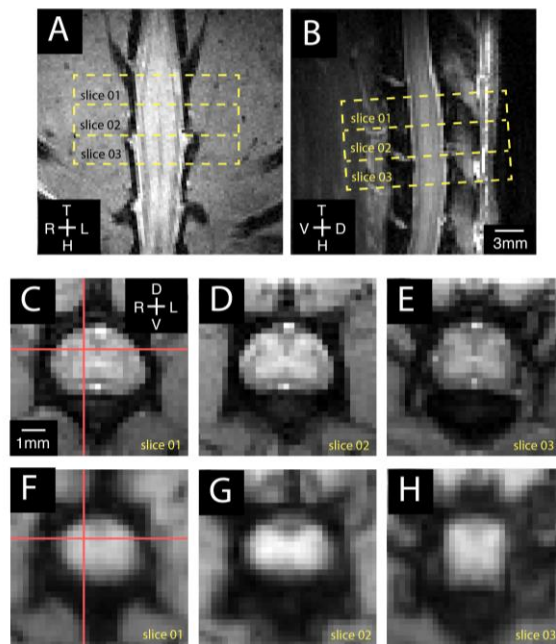


**Figure 40: MTC weighted anatomical images in three different views and axial functional BOLD images.** A gradient echo acquisition that incorporated a Gaussian radio frequency saturation pulse was used to obtain (A) coronal, and (B) sagittal views of the rat lumbar spinal cord with in-plane resolution of  $0.25 \times 0.25 \text{ mm}^2$  and slice thicknesses of 0.5mm and 0.75mm respectively. Yellow dashed borders and numbers on the images represent axial slice selections for anatomical (C-E) and BOLD (F-H) images for functional studies. D, dorsal; V, ventral; T, tail; H, head; L, left; R, right.

#### 4.4.6. Quantitative changes in functional connectivity post-SCI

With rsfMRI connectivity patterns established between horns of healthy lumbar spinal cords, a contusion injury lesion was introduced to evaluate if and how functional connectivity was modified (Figure 43). In order to quantitatively evaluate changes after injury, within-slice resting-state correlation strengths between different seed horn pairs were quantified at the group level (Figure 44). In healthy spinal cords, robust correlations were observed between left and right dorsal horns as well as between left and right ventral horns: mean correlation values of 0.61 and 0.50 were computed for dorsal-dorsal and ventral-ventral connections respectively. Weaker ipsilateral and contralateral dorsal and ventral horn connectivity measurements were also observed with 0.50 and 0.46 respectively.

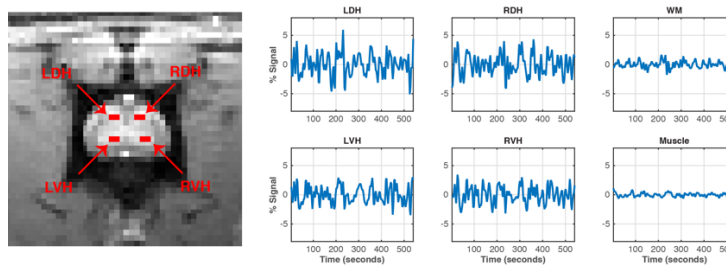


**Figure 41: Horns of the lumbar spinal cord, and averaged time series.** (Left) Anatomical MTC image of the rat lumbar spinal cord. Red regions indicate the four horns of the spinal cord (LDH, left dorsal horn; LVH, left ventral horn; RDH, right dorsal horn; RVH, right ventral horn). (Right) Averaged BOLD time series of the LDH, RDH, LVH, RVH, and WM of the spinal cord, white matter and muscle signal that have been regressed.

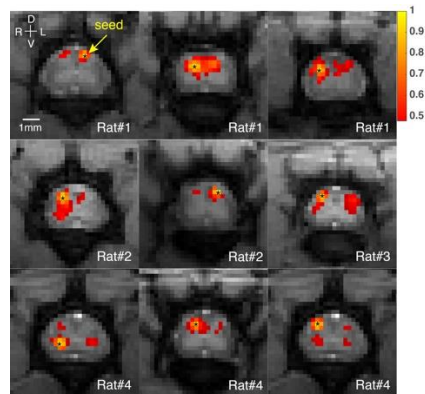


**Figure 42: Examples of within-slice resting-state correlation maps.** Averaged multiple runs within the same animal in the lumbar spinal cord across all control animals are displayed. Correlation maps were thresholded (Pearson's correlation coefficient,  $r > 0.50$ ) and the yellow voxels with asterisks indicate seed voxels. A minimum cluster threshold of 2 voxels was also used to prevent any spurious correlations.

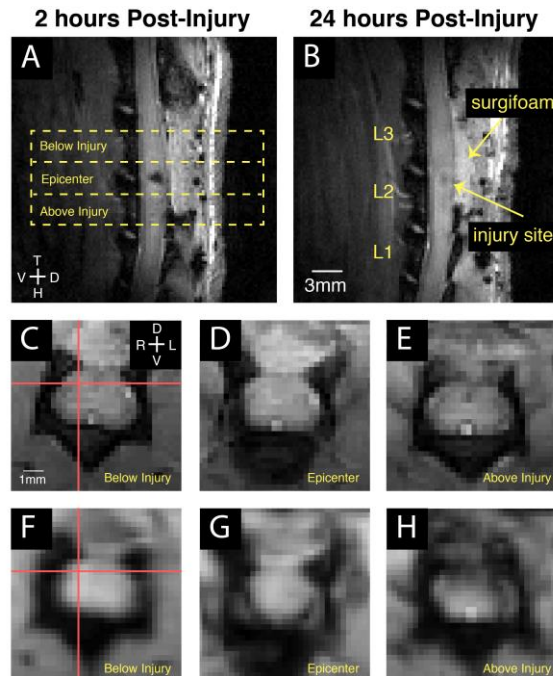


**Figure 43: MTC weighted anatomical images and axial BOLD images after injury.** Sagittal and axial views of the rat lumbar spinal cord with  $0.25 \times 0.25 \text{ mm}^2$  resolution with slice thickness of 0.75mm and 3mm respectively at (A) 2 hours and (B) 24 hours post-injury. Yellow dashed borders and numbers on the images represent axial slice selections for anatomical (C-E) images below, center of and above the injury. (F-H) Corresponding BOLD images for functional studies. D, dorsal; V, ventral; T, tail; H, head; L, left; R, right.

After the introduction of the injury, changes were found above (Figure 44, green background) and below injury (Figure 44, red background) with statistical comparisons made between each boxplot (Figure 45). Notably, an overall decrease and increase in correlation values was observed below and above the injury site respectively. In particular, averaged dorsal-dorsal connectivity strengths decreased by 0.12 and increased by 0.07 at segments below and above the injury respectively. A similar trend was also observed between ventral horns but to a lesser extent. Distributions of correlations for the three conditions are displayed for each ROI pair in Figure 44B. Notably, dorsal-dorsal connectivity histograms appear to be most distinguishable between below and above the injury ( $p < 0.005$  corrected) while below injury values presented only a subtle difference with controls ( $p = 0.08$  corrected). T-test of the correlation difference between above and below the injury within the same animals was also computed to be significant with  $p < 0.0005$ . Fractional amplitude of low-frequency fluctuation measurements as well as Wilcoxon-rank sum tests between individual boxplots were also performed that showed no statistical differences between the three regions of interest (Figure 46). Despite the presence of a lesion, dorsal-dorsal

connectivity interestingly also remains to be largely significant within each condition. Additionally, the reproducibility of spinal cord connectivity under the three conditions was quantified with correspondences between odd and even runs from each animal as shown in Figure 43. Qualitatively, data points in correlation plots appear to lie predominantly on the diagonal line (slope=1) with a correlation value of 0.66 ( $p=2.12 \times 10^{-12}$ ). Bland Altman plots further reveal connectivity measurements were within limits that are similar to ranges found in those at the cervical level, suggesting a similar general agreement between measurements between the two regions of the spine.

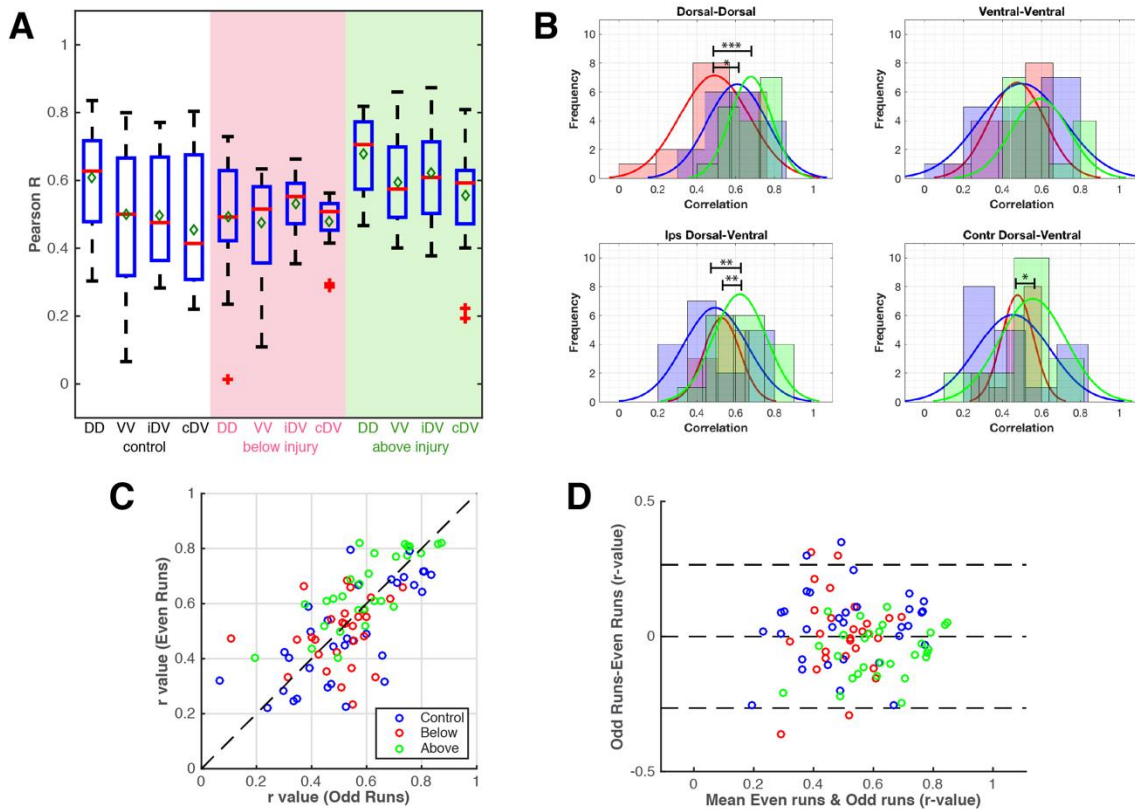


**Figure 44: Group analysis of functional connectivity between spinal cord gray matter horns.** (A) Boxplots between each spinal horn in controls (white background), below (red background) and above (green background) the contusion lesion. Each boxplot contains 18 runs for controls and 17 runs for injured animals. Red lines and green diamonds represent medians and means of each boxplot respectively. (B) Histograms of correlations values with a Gaussian fit for controls, above and below the injury site for four different ROI pairs. Non-parametric Wilcoxon rank sum tests were performed with corrected p-values  $*p<0.1$ ,  $**p<0.05$ , and  $***p<0.005$ . (C) Reproducibility and agreement of within-slice horn-to-horn functional connectivity. Functional connectivity measurements were divided into two subgroups consisting of even and odd runs for each animal. (D) Bland-Altman plots of horn-to-horn connectivity with black dotted lines are 95% limits of agreement.

## 4.5. Discussion and conclusions

### 4.5.1. PSR as a biomarker for demyelination

In this study, we observed a decreasing trend of PSR within two weeks post-SCI, which was later validated with histological results. Indeed, evidences from animal models (Blight, 1985; Powers et al., 2012; Totoiu and Keirstead, 2005) and human specimens (Bunge et al., 1997; Guest et al., 2005; Norenberg et al., 2004) corroborate the observation that demyelination occurs after SCI, particularly during the acute phase (Plemel et al., 2014). For example, one of the earliest studies found using electron microscopy that demyelination occurred by 21 hours and continued to worsen within the first week post injury (Gledhill et al., 1973). More recently, Ek et al. have also studied pathological changes in white matter following a contusion injury using immunohistochemistry and LFB stains. They reported that the number of myelinated axons decreased to approximately 24% of controls 24 hours post-SCI and by week 1, only 13% remained (Ek et al., 2012). These results are largely consistent with PSR measurements in this study, suggesting qMT parameters may be capable of reflecting specific information about the molecular changes and the progression of demyelination produced at acute stages of SCI.

### 4.5.2. Functional relevance of myelination

The battery of behavioral assessments performed in this study revealed insignificant correlations with longitudinal PSR measurements. Specifically, the decreasing trend in PSR measurements over two weeks corresponded with locomotor and sensory recoveries after either the first or second week post-SCI. Re-myelination has been shown to be a spontaneous process where oligodendrocytes and Schwann cells regenerate damaged or lost myelin in the absence of any therapeutic intervention (Sellers et al., 2009; Tripathi and McTigue, 2007), and its functional relevance remains unclear.

Previous studies have found correlations between spinal re-myelination with improvements in locomotion after chemical demyelination and irradiated diet (Duncan et al., 2009; Jeffery and Blakemore, 1997). The transplantation of cells that promote the formation of new oligodendrocyte (Keirstead et al., 2005) or Schwann cells (Keirstead and Blakemore, 1997) have also demonstrated functional improvements. That being said, conduction has also been shown possible through short segments of demyelination *in vivo*. Specifically, de-myelinated spinal cord

axons have been shown to be capable of conducting through lengths of at least 2.5mm (Felts et al., 1997). With demyelination of spared axons largely focal to the lesion epicenter following SCI (Powers et al., 2012), re-myelination may not be a necessity to activating residual local spinal circuits. In fact, a recent study found hindlimb motor functions in rodents recovered spontaneously after inhibition of myelin regeneration through the deletion of *myel* regulator factor in rodents, raising doubts for whether demyelination is a valid therapeutic target for moderate spinal contusion injuries (Duncan et al., 2018). In our study, we found an un-correlated trend between PSR and behavioral measurements, and this could be because the extent of demyelination at a moderate injury level may not contribute to detectable functional deficits. Short distance demyelination, like the ones in our moderate contusion SCI model, may also not be functionally relevant. Additionally, this may also imply that PSR methods described here may not be sensitive enough to detecting potential subtle recovery changes at a moderate injury level or that specific behavioral assessments performed did not reflect deficits that continued to worsen. Overall, therapies geared towards SCI re-myelination continue to be important but also warrant further investigation.

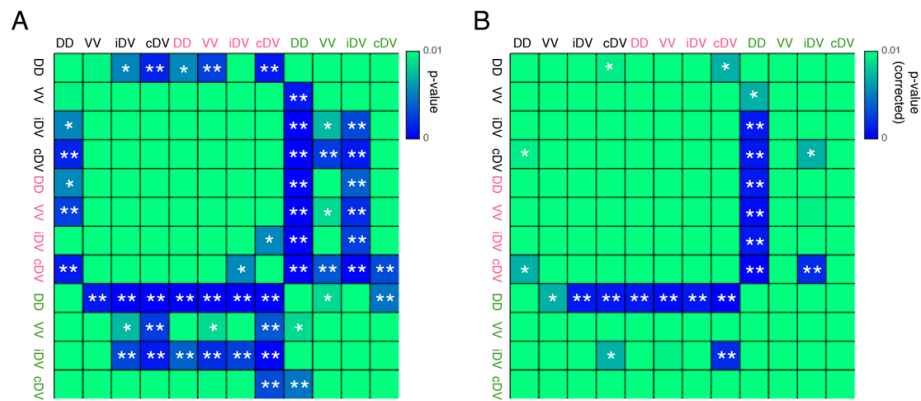


**Figure 45: Matrix of nonparametric Mann-Whitney tests between each boxplot in Figure 44.** P-values of differences between boxplots are displayed without (A) and with (B) correction for multiple comparisons. White asterisks indicate \* $p < 0.1$  and \*\* $p < 0.05$  corrected.

#### 4.5.3. PSR and other MRI parameters

Different MRI parameters are sensitive to different tissue abnormalities post-SCI, and the combination of them provides valuable information from various aspects in deciphering specific changes post-SCI. With PSR being sensitive to myelin content, radial and axial diffusivities have previously been indicated as potential *in vivo* surrogate biomarkers for demyelination and axonal

damage respectively (Janve et al., 2013; Ou and Gochberg, 2008; Song et al., 2005). Specifically, an increase in radial diffusivity has been associated with a decrease in myelin content, while axonal damage has been correlated with diminished axial diffusivity. With PSR and radial diffusivity both sensitive to myelin, a greater correlation was observed between PSR and radial diffusivity than with axial diffusivity as expected. ADC values encompass diffusivity both along and perpendicular to axons, and have been shown to reflect axon size and possibly the thickness of the myelin sheath. The negative but insignificant correlation with PSR may correspond to a decrease in myelin and cell density but also a reduced sensitivity to SCI relative to other metrics. Similarly in a recent study, ADC also did not show significant changes at acute phases of the injury that were reflected in FA measurements (Li et al., 2015). In both our previous study (Wang et al., 2015) of a dorsal column lesion model and in this study, a high correspondence between FA and PSR was observed. Various factors including axonal density, fiber coherence and myelination can contribute to FA and thus, the high correlation coefficient between mean FA and PSR time courses suggests axonal damage may be associated with demyelination. While correlations between PSR and FA have been less apparent in the brain (Underhill et al., 2009) possibly due to orientation dispersions, the ordered and unidirectional microstructure of the spinal cord could explain highly coupled trends between the two observed metrics.

Additionally, other parameters used to describe the MT effect were correlated with PSR values. Consistent with our previous SCI study (Wang et al., 2015), we found positive correlations with  $R_{2A}$  and  $RM_{0b}$  and a negative correlation with  $R_{2b}$  when compared to PSR measurements. Concentrations of macromolecules generally affect relaxation rates, and thus a decrease in  $R_{2a}$  with decreased PSR is expected which further indicates the presence of de-myelination post SCI.  $R_{2b}$ , on the other hand, is more stable across conditions (Smith et al., 2009), but have also been reported to be sensitive to white matter fiber orientation (Cercignani et al., 2018).

#### **4.5.4. Spinal rsfMRI as a biomarker for pathology**

Given that spinal rsfMRI is a recently detected phenomenon, there have been only two publications to date that have examined its use as a surrogate biomarker in pathological conditions: in a NHP dorsal column lesion (Chen et al., 2015) and multiple sclerosis human patients (Conrad et al., 2018). Similar to our findings here, the introduction of a dorsal column lesion in NHPs induced a reduction in correlation values below the injury site, while functional connectivity

between horns above the lesion appear to be comparable to those of controls (Chen et al., 2015). Interestingly, patterns of functional connectivity between ROIs were found to be similar regardless of position relative to the injury site, a finding also consistent to ours here where dorsal-dorsal connectivity remains greatest above and below the injury, which is suggestive of a local functional circuit at the segmental level. In multiple sclerosis patients, functional networks in the spinal cord appear to be intact at 7T although local alterations of connectivity patterns were observed (Conrad et al., 2018). Specifically, dorsal-dorsal and ventral-ventral connectivities were reduced both above and below lesions although no statistical differences were observed in average connectivity or power of low frequency fluctuations in patients compared to controls. While direct comparisons between these studies may not be appropriate due to variabilities in species and injury models, findings from these studies suggest the presence of altered connectivity strengths to some degree between horns of the spinal after a disruption to the cord. In light of these findings, our results here adds to the potential of spinal rsfMRI as a biomarker for assessing of the spinal cord's circuitry.

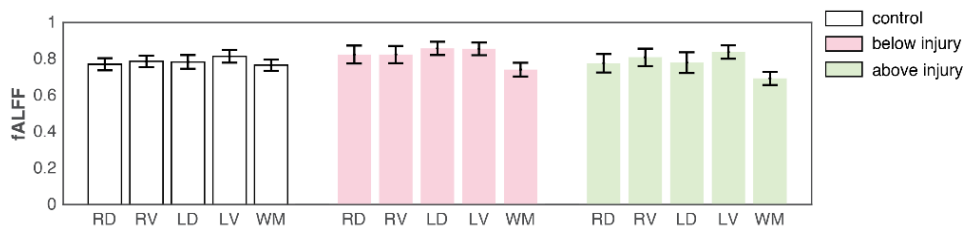


**Figure 46: Averaged fALFF for the four horns of the high-pass filtered 0.01Hz raw spinal cord data.** fALFF was calculated between 0.01-0.08Hz from spinal slices of control rat (white bars), below (red bars) and above injury slices (green bars). RD, right dorsal horn; LD, left dorsal horn; RV, right ventral horn; LV, left ventral horn; WM, white matter.

#### 4.5.5. Limitations and improvements

The degree of demyelination after SCI is dependent on the type as well as the the severity of the injury inflicted. While we have observed a progressive decrease in PSR over two weeks of monitoring which was verified with histology, the sensitivity of qMT to modulations in different SCI models still warrants further investigation. In particular, to what extent qMT is capable of predicting different grades of injuries would provide further insights on its sensitivity limits. Additionally, longitudinal myelin changes at chronic stages as well as whether qMT is able to pick

up subtle re-myelination therapeutic changes are further questions of interest. In this study, a contusion model was selected due to its clinical relevance. However, in order to answer some of the above questions, a more controlled injury that produces less subtle changes, such as a transection injury, may be more suitable in evaluating its novel application in SCIs.

Inflammation occurs during acute stages of a contusion injury and can confound interpretations of both PSR and radial diffusivity as markers for myelination. At the molecular level, reduced intra-axonal water diffusivity along with infiltrating cells may result in dissociation of their coupled relationship. Moreover, the presence of inflammation has also been shown to affect qMT measurements due to the increase of extra-myelin water protons and pH changes. Notably, Stanisiz et al. found that PSR may not be the best indicator of myelination in the presence of inflammation (Stanisiz et al., 2004), while Odrobina et al. noted the difficulty of separating inflammatory effects from demyelination by qMT (Odrobina et al., 2005).

Due to technical limitations, rsfMRI data were analyzed only at the 24-hour time point. Specifically, prevalent motion artifacts were observed for BOLD data at week-1 and week-2. One possible explanation is the resistance to isoflurane that was developed by animals after successive sessions of isoflurane exposure during the acute phase of the injury. With isoflurane maintained between 0.9-1.1% for functional scans, small movements from the rat can not only cause  $B_0$  changes but also shifts in EPI images from the movement itself (Hu and Kim, 1994; Pfeuffer et al., 2002; Zhao et al., 2008), especially with the cord's small physical size. Indeed, rats were exposed to isoflurane on the day of the surgery, during multi-parametric MRI sessions at 6 hours and 24 hours post-SCI, and during subsequent days when manual bladder expressions were necessary (usually 2 additional days) before the week-1 timepoint scan. One possible solution is the administration of reversible neuromuscular blockers during fMRI sessions. As Chen et al. have previously demonstrated in NHPs, functional connectivity recovered over time (Chen et al., 2015) and it would be valuable to evaluate whether such a trend is evident in rodents after a more clinically applicable contusion injury. Additionally, validation of rsfMRI findings reported here with electrophysiology will also be significant for evaluating to what extent neural activity is reflected in the BOLD signal.

Nevertheless, this is the first study to our knowledge to have applied multi-parametric MRI methods along with behavioral and histological assessments for monitoring of a lumbar contusion SCI model. Moreover, technical developments and translations of baseline qMT and rsfMRI at the

lumbar level are also novel and will inform future studies of organization of the cord under different conditions. Overall, the use of non-invasive multi-parametric MRI allows for examining and monitoring spontaneous repair of the injured spinal cord in comprehensive detail. Specifically, the combination of longitudinal *in vivo* qMT imaging and DTI along with behavioral, histological and functional assessments provide complementary information about the pathophysiological basis of the progression and recovery from SCIs.

#### **4.5.6. Acknowledgements**

This study is supported by NIH grant NS092961. The author gratefully acknowledges Dr. Zou Yue and Chaohui Tang for their assistance with surgical procedures and perfusion of animals, as well as Frances Shook from the Translational Pathology Shared Resource lab for her help with histology.

#### 4.6. References

- Barry, R.L., Smith, S.A., Dula, A.N., Gore, J.C., 2014. Resting state functional connectivity in the human spinal cord. *Elife* 2014, 1–15. doi:10.7554/eLife.02812
- Blight, a R., 1985. Delayed demyelination and macrophage invasion: a candidate for secondary cell damage in spinal cord injury. *Cent. Nerv. Syst. Trauma* 2, 299–315. doi:10.1089/cns.1985.2.299
- Bunge, R.P., Puckett, W., Hiester, E.D., 1997. Observations on the pathology of several types of human spinal cord injury, with emphasis on the astrocyte response to penetrating injuries. *Adv. Neurol.* 72, 305–315.
- Casha, S., Yu, W.R., Fehlings, M.G., 2001. Oligodendroglial apoptosis occurs along degenerating axons and is associated with FAS and p75 expression following spinal cord injury in the rat. *Neuroscience* 103, 203–218. doi:10.1016/S0306-4522(00)00538-8
- Cercignani, M., Alexander, D.C., 2006. Optimal acquisition schemes for in vivo quantitative magnetization transfer MRI. *Magn. Reson. Med.* 56, 803–810. doi:10.1002/mrm.21003
- Cercignani, M., Barker, G.J., 2008. A comparison between equations describing in vivo MT: The effects of noise and sequence parameters. *J. Magn. Reson.* 191, 171–183. doi:10.1016/j.jmr.2007.12.012
- Cercignani, M., Dowell, N.G., Tofts, P.S., 2018. *Quantitative MRI of the Brain: Principles of Physical Measurement, Second edition (Series in Medical Physics and Biomedical Engineering) 2nd Edition.* CRC Press.
- Chan, C.C.M., 2008. Inflammation: beneficial or detrimental after spinal cord injury? *Recent Pat. CNS Drug Discov.* 3, 189–199. doi:10.2174/157488908786242434
- Chen, L.M., Mishra, A., Yang, P.-F., Wang, F., Gore, J.C., 2015. Injury alters intrinsic functional connectivity within the primate spinal cord. *Proc. Natl. Acad. Sci. U. S. A.* 112, 5991–6. doi:10.1073/pnas.1424106112
- Conrad, B.N., Barry, R.L., Rogers, B.P., Maki, S., Mishra, A., Thukral, S., Sriram, S., Bhatia, A., Pawate, S., Gore, J.C., Smith, S.A., 2018. Multiple sclerosis lesions affect intrinsic functional connectivity of the spinal cord. *Brain.* doi:10.1093/brain/awy083
- Deloire-Grassin, M.S., Brochet, B., Quesson, B., Delalande, C., Dousset, V., Canioni, P., Petry, K.G., 2000. In vivo evaluation of remyelination in rat brain by magnetization transfer imaging. *J. Neurol. Sci.* 178, 10–6.
- Duncan, G.J., Manesh, S.B., Hilton, B.J., Assinck, P., Liu, J., Moulson, A., Plemel, J.R., Tetzlaff, W., 2018. Locomotor recovery following contusive spinal cord injury does not require oligodendrocyte remyelination. *Nat. Commun.* 9. doi:10.1038/s41467-018-05473-1
- Duncan, I.D., Brower, A., Kondo, Y., Curlee, J.F., Schultz, R.D., 2009. Extensive remyelination of the CNS leads to functional recovery. *Proc. Natl. Acad. Sci.* 106, 6832–6836.

doi:10.1073/pnas.0812500106

- Ek, C.J., Habgood, M.D., Dennis, R., Dziegielewska, K.M., Mallard, C., Wheaton, B., Saunders, N.R., 2012. Pathological Changes in the White Matter after Spinal Contusion Injury in the Rat. *PLoS One* 7. doi:10.1371/journal.pone.0043484
- Fawcett, J.W., Asher, R.A., 1999. The glial scar and central nervous system repair. *Brain Res. Bull.* doi:10.1016/S0361-9230(99)00072-6
- Felts, P.A., Baker, T.A., Smith, K.J., 1997. Conduction in Segmentally Demyelinated Mammalian Central Axons. *J. Neurosci.* 17, 7267–7277. doi:97442496
- Gledhill, R.F., Harrison, B.M., McDonald, W.I., 1973. Demyelination and remyelination after acute spinal cord compression. *Exp. Neurol.* 38, 472–487. doi:10.1016/0014-4886(73)90169-6
- Gochberg, D.F., Gore, J.C., 2003. Quantitative imaging of magnetization transfer using an inversion recovery sequence. *Magn. Reson. Med.* 49, 501–505. doi:10.1002/mrm.10386
- Gore, J.C.J.C., 2003. Principles and practice of functional MRI of the human brain. *J. Clin. Invest.* 112, 4–9. doi:10.1172/JCI200319010.Conventional
- Guest, J.D., Hiester, E.D., Bunge, R.P., 2005. Demyelination and Schwann cell responses adjacent to injury epicenter cavities following chronic human spinal cord injury. *Exp. Neurol.* 192, 384–393. doi:10.1016/j.expneurol.2004.11.033
- Hawthorne, A.L., Popovich, P.G., 2011. Emerging Concepts in Myeloid Cell Biology after Spinal Cord Injury. *Neurotherapeutics* 8. doi:10.1007/s13311-011-0032-6
- Henkelman, R.M., Huang, X., Xiang, Q.-S.S., Stanisz, G.J., Swanson, S.D., Bronskill, M.J., 1993. Quantitative interpretation of magnetization transfer. *Magn Reson Med.* doi:10.1002/mrm.1910290607
- Horsfield, M.A., Jones, D.K., 2002. Applications of diffusion-weighted and diffusion tensor MRI to white matter diseases - A review. *NMR Biomed.* doi:10.1002/nbm.787
- Hu, X., Kim, S.G., 1994. Reduction of signal fluctuation in functional MRI using navigator echoes. *Magn. Reson. Med.* 31, 495–503. doi:10.1002/mrm.1910310505
- Janve, V.A., Zu, Z., Yao, S.Y., Li, K., Zhang, F.L., Wilson, K.J., Ou, X., Does, M.D., Subramaniam, S., Gochberg, D.F., 2013. The radial diffusivity and magnetization transfer pool size ratio are sensitive markers for demyelination in a rat model of type III multiple sclerosis (MS) lesions. *Neuroimage* 74, 298–305. doi:10.1016/j.neuroimage.2013.02.034
- Jeffery, N.D., Blakemore, W.F., 1997. Locomotor deficits induced by experimental spinal cord demyelination are abolished by spontaneous remyelination. *Brain* 120, 27–37. doi:10.1093/brain/120.1.27
- Ju, G., Wang, J., Wang, Y., Zhao, X., 2014. Spinal cord contusion. *Neural Regen. Res.* 9, 789–794.

doi:10.4103/1673-5374.131591

- Keirstead, H.S., Blakemore, W.F., 1997. Identification of post-mitotic oligodendrocytes incapable of remyelination within the demyelinated adult spinal cord. *J. Neuropathol. Exp. Neurol.* 56, 1191–1201. doi:10.1097/00005072-199711000-00003
- Keirstead, H.S., Nistor, G., Bernal, G., Totoiu, M., Cloutier, F., Sharp, K., Steward, O., 2005. Human Embryonic Stem Cell-Derived Oligodendrocyte Progenitor Cell Transplants Remyelinate and Restore Locomotion after Spinal Cord Injury. *J. Neurosci.* 25, 4694–4705. doi:10.1523/JNEUROSCI.0311-05.2005
- Kim, D.H., Vaccaro, A.R., Henderson, F.C., Benzel, E.C., 2003. Molecular biology of cervical myelopathy and spinal cord injury: role of oligodendrocyte apoptosis. *Spine J.* 3, 510–519. doi:10.1016/S1529-9430(03)00117-7
- Li, X.-H., Li, J.-B., He, X.-J., Wang, F., Huang, S.-L., Bai, Z.-L., 2015. Timing of diffusion tensor imaging in the acute spinal cord injury of rats. *Sci. Rep.* 5, 12639. doi:10.1038/srep12639
- Loy, D.N., Kim, J.H., Xie, M., Schmidt, R.E., Trinkaus, K., Song, S.-K., 2007. Diffusion Tensor Imaging Predicts Hyperacute Spinal Cord Injury Severity. *J. Neurotrauma* 24, 979–990. doi:10.1089/neu.2006.0253
- Norenberg, M.D., Smith, J., Marcillo, A., 2004. The Pathology of Human Spinal Cord Injury: Defining the Problems. *J. Neurotrauma* 21. doi:10.1089/089771504323004575
- Odrobina, E.E., Lam, T.Y.J., Pun, T., Midha, R., Stanisz, G.J., 2005. MR properties of excised neural tissue following experimentally induced demyelination. *NMR Biomed.* 18, 277–284. doi:10.1002/nbm.951
- Ou, X., Gochberg, D.F., 2008. MT effects and T1 quantification in single-slice spoiled gradient echo imaging. *Magn. Reson. Med.* 59, 835–845. doi:10.1002/mrm.21550
- Pfeuffer, J., Van Moortele, P.F. De, Ugurbil, K., Hu, X., Glover, G.H., 2002. Correction of physiologically induced global off-resonance effects in dynamic echo-planar and spiral functional imaging. *Magn. Reson. Med.* 47, 344–353. doi:10.1002/mrm.10065
- Plemel, J.R., Keough, M.B., Duncan, G.J., Sparling, J.S., Yong, V.W., Stys, P.K., Tetzlaff, W., 2014. Remyelination after spinal cord injury: Is it a target for repair? *Prog. Neurobiol.* doi:10.1016/j.pneurobio.2014.02.006
- Powers, B.E., Lasiene, J., Plemel, J.R., Shupe, L., Perlmutter, S.I., Tetzlaff, W., Horner, P.J., 2012. Axonal Thinning and Extensive Remyelination without Chronic Demyelination in Spinal Injured Rats. *J. Neurosci.* 32, 5120–5125. doi:10.1523/JNEUROSCI.0002-12.2012
- Ramani, A., Dalton, C., Miller, D.H., Tofts, P.S., Barker, G.J., 2002. Precise estimate of fundamental in-vivo MT parameters in human brain in clinically feasible times. *Magn. Reson. Imaging* 20, 721–

731. doi:10.1016/S0730-725X(02)00598-2

- Schmierer, K., Scaravilli, F., Altmann, D.R., Barker, G.J., Miller, D.H., 2004. Magnetization transfer ratio and myelin in postmortem multiple sclerosis brain. *Ann. Neurol.* doi:10.1002/ana.20202
- Sellers, D.L., Maris, D.O., Horner, P.J., 2009. Postinjury Niches Induce Temporal Shifts in Progenitor Fates to Direct Lesion Repair after Spinal Cord Injury. *J. Neurosci.* 29, 6722–6733. doi:10.1523/JNEUROSCI.4538-08.2009
- Smith, S. a, Golay, X., Fatemi, A., Mahmood, A., Raymond, G. V, Moser, H.W., van Zijl, P.C.M., Stanisz, G.J., 2009. Quantitative magnetization transfer characteristics of the human cervical spinal cord in vivo: application to adrenomyeloneuropathy. *Magn. Reson. Med.* 61, 22–7. doi:10.1002/mrm.21827
- Song, S.K., Yoshino, J., Le, T.Q., Lin, S.J., Sun, S.W., Cross, A.H., Armstrong, R.C., 2005. Demyelination increases radial diffusivity in corpus callosum of mouse brain. *Neuroimage* 26, 132–140. doi:10.1016/j.neuroimage.2005.01.028
- Stanisz, G.J., Webb, S., Munro, C., Pun, T., Midha, R., 2004. MR properties of excised neural tissue following experimentally induced inflammation. *Magn Reson Med* 51, 473–479.
- Stejskal, E.O., Tanner, J.E., 1965. Spin diffusion measurements: Spin echoes in the presence of a time-dependent field gradient. *J. Chem. Phys.* 42, 288–292. doi:10.1063/1.1695690
- Totoiu, M.O., Keirstead, H.S., 2005. Spinal cord injury is accompanied by chronic progressive demyelination. *J. Comp. Neurol.* 486, 373–383. doi:10.1002/cne.20517
- Tripathi, R., McTigue, D.M., 2007. Prominent oligodendrocyte genesis along the border of spinal contusion lesions. *Glia* 55, 698–711. doi:10.1002/glia.20491
- Underhill, H., Yuan, C., Yarnykh, V., 2009. Direct Quantitative Comparison between Cross-Relaxation Imaging and Diffusion Tensor Imaging of the Human Brain, in: *Proceedings 17th Scientific Meeting, International Society for Magnetic Resonance in Medicine.* p. 2749.
- van den Heuvel, M.P., Hulshoff Pol, H.E., 2010. Exploring the brain network: A review on resting-state fMRI functional connectivity. *Eur. Neuropsychopharmacol.* doi:10.1016/j.euroneuro.2010.03.008
- Vedantam, A., Jirjis, M.B., Schmit, B.D., Wang, M.C., Ulmer, J.L., Kurpad, S.N., 2014. Diffusion tensor imaging of the spinal cord: Insights from animal and human studies. *Neurosurgery.* doi:10.1227/NEU.0000000000000171
- Wang, F., Li, K., Mishra, A., Gochberg, D., Min Chen, L., Gore, J.C., 2015. Longitudinal assessment of spinal cord injuries in nonhuman primates with quantitative magnetization transfer. *Magn. Reson. Med.* 1696, 1685–1696. doi:10.1002/mrm.25725
- Wolff, S.D., Balaban, R.S., 1989. Magnetization transfer contrast (MTC) and tissue water proton relaxation in vivo. *Magn. Reson. Med.* doi:10.1002/mrm.1910100113

Wu, T.-L., Wang, F., Mishra, A., Wilson, G.H., Byun, N., Chen, L.M., Gore, J.C., 2017. Resting-state functional connectivity in the rat cervical spinal cord at 9.4 T. *Magn. Reson. Med.*

doi:10.1002/mrm.26905

Zhao, F., Williams, M., Meng, X., Welsh, D.C., Coimbra, A., Crown, E.D., Cook, J.J., Urban, M.O., Hargreaves, R., Williams, D.S., 2008. BOLD and blood volume-weighted fMRI of rat lumbar spinal cord during non-noxious and noxious electrical hindpaw stimulation. *Neuroimage* 40, 133–147.

doi:10.1016/j.neuroimage.2007.11.010

## **Chapter 5: SUMMARY, SIGNIFICANCES AND FUTURE STUDIES**

### **5.1. Summary and significances**

As a relay station between the brain and the rest of the body, it is indisputable that the spinal cord plays a critical role in our central nervous system. Not only does the spinal cord serve as a conduit for motor outputs from the brain and peripheral inputs to the brain, but it is also a center for mediating and coordinating certain reflexes. Given the spinal cord's functional importance, traumatic damage to it disrupts neural pathways that leads to sensory impairment as well as motor deficits that can severely impact quality of life and even life expectancy. Thus, a better understanding of baseline and spontaneous repair processes of spinal cord structure and function becomes critical for the design and assessment of therapeutic interventions.

In light of recent developments of rsfMRI in the spinal cord (Barry et al., 2018), the interpretation of findings from fMRI studies relies on understanding the relationship of BOLD effects with underlying neurophysiology. However, to date, this information has been quite limited and studies that have explored the relationship of BOLD signals with electrophysiological activity in the brain (under rest and task conditions) have remained controversial and inconsistent. Chapter 2 of this thesis provides the first piece of evidence to fill this knowledge gap at the spinal level as the relationship between electrophysiology and fMRI signals was investigated. Specifically, results demonstrated a high concordance between LFP and fMRI metrics and that there was an intrinsic functional architecture within gray matter of a single spinal segment. Overall, findings reported in Chapter 2 suggest that low frequency electrophysiological activity may underlie fMRI BOLD signals acquired at high field in the spinal cord both in a resting state and during processing of an external stimulus, and that resting-state functional connectivity measured with rsfMRI signals can be reliably used as a biomarker of neural connectivity.

Given rodents allow more reliable contusion lesions to be induced for longitudinal studies, the translation of spinal resting-state functional studies to them at baseline states in Chapter 3 becomes equally important. Despite a smaller spinal cord in rodents than in NHPs and humans, functional images acquired at 9.4T were of sufficiently high quality to provide adequate contrast between gray and white matter. Consistent with human and NHP studies (Barry et al., 2014; Chen et al., 2015), functional connectivity between gray matter horns presented significant correlations when compared to control regions. Specifically, dorsal-dorsal and ventral-ventral connectivity

measurements were observed to be most prominent and reproducible. With fMRI protocols implemented in rodents and baseline functional connectivity established, Chapter 3 presents the foundation for rsfMRI as one of the metrics to exploring changes after a contusion injury in Chapter 4.

Spontaneous recovery of damaged spinal cords remains incompletely understood mainly because an appropriate longitudinal tracking technique has yet to exist. In Chapter 4, a clinically relevant contusion injury model was applied to rodents. Progression of the injury during the first two weeks in white matter tracts was tracked longitudinally with DTI and qMT, while behavioral assessments and histological myelin stains were collected in parallel. Results showed a decrease of myelin content in the two weeks, which interestingly did not correlate with behavioral recovery. Implications of this finding could cast further doubts on remedies and interventions targeted towards remyelination, although this may also imply MR methods reported here must be improved with greater sensitivity for detecting subtle recovery changes. Moreover, functional integrity of spinal gray matter was assessed using fMRI, which revealed subtle decreases and increases in correlations below and above the injury respectively, an observation largely consistent with the effects of a dorsal column lesion in NHPs (Chen et al., 2015).

In summary, this thesis measured inter-regional correlations in a resting state within the spinal cords of animals, validated their neuronal bases, and provided characterization of changes in structure and function of the cord after injury. Recent developments have shown therapeutic regeneration of the disrupted neural pathway (Thuret et al., 2006) and functional electrical stimulations that assist the recovery process (Bamford and Mushahwar, 2011). As extensive research efforts continue to promote SCI patient recovery, the application of quantitative MRI may contribute to the design of effective therapeutic interventions as well as the evaluation of treatment outcomes.

## **5.2. Future studies**

### **5.2.1. Z-spectra of the spinal cord after injury**

In addition to the battery of quantitative imaging methods used in this thesis to monitor a spinal contusion injury, the study of Z-spectra around the lesion site after spinal cord injury can

further reveal changes in the cellular and molecular compositions of spinal tissue. Specifically, chemical exchange saturation transfer (CEST) from metabolites and nuclear overhauser enhancements (NOE) from mobile aliphatic macromolecules from immobile proteins can be quantified and compared both regionally and longitudinally around the lesion site of spinal cord injuries. CEST imaging is a relatively novel technique that have previously been shown to detect tumor regions, and is also capable of separating tumor progression from radiation necrosis (Zhou et al., 2011). When applied to a unilateral dorsal column lesion model in NHPs, Z-spectra revealed increased amide, amine and hydroxyl CEST effects while semisolid MT and NOE effects weakened in cyst regions relative to those of normal gray matter. As the injury recovered, the cyst shrank in parallel with a reduction of CEST effects and an increase in semisolid MT and NOE around the lesion site (Wang et al., 2018, 2014). In order to validate these CEST quantifications, direct metabolite measurements are made possible with intraparenchymal microdialysis in SCI models, which has previously been shown to detect changes of energy-related substrates (glucose, lactate and pyruvate) and markers of excitotoxicity (glutamate) within hours post-SCI (Okon et al., 2013; Streijger et al., 2017).

In the context of a contusion spinal cord injury model presented in this thesis, an excessive release of glutamate after the injury occurs within and around the injury site (McAdoo et al., 1999). The elevated level of glutamate produces direct damage to the spinal cord as well as indirect damage from the production of reactive oxygen and nitrogen species. Specifically, the influx of calcium ions, due to glutamate binding of receptor proteins, causes a widespread excitotoxic cell death (Xu et al., 2005). In fact, neurons and oligiondendrocytes are particularly vulnerable to such effects as they express a full complement of glutamate receptors. Therefore, the application of CEST imaging in the acute phase can be significant in both understanding metabolic consequences and evaluating therapies in mitigating secondary pathophysiologic processes. For example, there has been much effort in developing drugs that inhibit glutamate receptors for preventing excess ions from entering and subsequently damaging the neuron (Lea and Faden, 2003), and indeed CEST imaging could be a valuable surrogate marker for tracking therapeutic changes non-invasively around the lesion at the spinal level. Overall, CEST imaging presents another attractive biomarker that can be developed in a contusion injury model as it provides *in vivo* information about the cellular and molecular signatures of the lesion by detecting specific exchangeable protons from metabolites.

### 5.2.2. Longitudinal electrophysiology studies

The research study reported in Chapter 2 of this thesis is the first to demonstrate resting-state electrophysiology in the spinal cord, and will open up additional experiments to provide more conclusive understanding on the information flow between different spinal horns. For example, electrophysiology obtained at different time points during the time course of injury recovery is valuable as Chen et al. have previously reported a trend of functional connectivity recovery between bilateral dorsal horns with increasing correlation values (Chen et al., 2015). Validation of this rsfMRI finding with longitudinal electrophysiological measurements will provide further insight in understanding the neuronal basis of impaired spinal gray matter function. Additionally, examining what aspects of accessible electrophysiological signals (neuronal spiking and LFPs) and at what frequency bands correlate most closely with inter-regional low frequency MRI correlations longitudinally can also be critical for proper interpretation of MRI findings.

In order to further depict local spinal circuits, anatomical tracers can also be used to investigate whether regions that exhibit highly correlated resting-state functional connectivity are also anatomically connected. In regard to the robust connectivity observed between spinal horns, early anatomical evidences have shown primary afferents cross over to the contralateral dorsal horn (Culberson et al., 1979; Light and Perl, 1979) while electrophysiological studies suggested the existence of an interneuronal network between them (Fitzgerald, 1983, 1982). Further supporting this notion, recent evidences have also identified the presence of dorsal commissural interneuron populations (Bannatyne, 2006; Petkó and Antal, 2000). Taking a step further, resting-state functional connectivity strengths measured with electrophysiology at different timepoints post-SCI can be correlated with anatomical connectivity identified with stains such as biotinylated dextran amine stained fibers on high resolution micrographs. While the absence of direct connection does not preclude the possibility of functional connectivity between two regions due to the possibility of indirect connections, the investigation of spontaneous repair of injured spinal cord by assessing changes in micro-structural integrity and anatomical fiber connectivity in relation to functional connectivity can further elucidate the neurobiological underpinnings of detected functional connectivity patterns.

Lastly, the correlation of functional connectivity measures to the severity of behavioral deficits and recovery can provide assessment of whether functional connectivity measurements are reliable prognostic indicators of specific behavioral impairments. Specifically, behavioral tasks

that are sensitive to spinal deafferentation, reorganization as well as the extent of the injury in squirrel monkeys have successfully been implemented here at Vanderbilt University (Qi et al., 2014). Notably, food reaching and grasping tasks of food pellets from wells of different depths allow for quantitative evaluations of success rates and the number of digit flexes. This specific assessment also often requires the use of high-speed video recording that captures the motion of hand use performances. Thus by correlating such behavioral measurements with rsfMRI and electrophysiological signals, we can further examine to what extent these functional connectivity measurements are sensitive to predicting specific task deficit outcomes.

### **5.2.3. Ventral horn sampling in electrophysiology studies**

As pointed out in Chapter 2, the restricted sampling field-of-view prevented ventral horns to be fully sampled in spinal electrophysiology experiments. Ventral-ventral connectivity has been shown to be most robust and reproducible in both humans and animals (Barry et al., 2018, 2014; Wu et al., 2017). In support of this finding, a number of studies have also reported the presence of commissural interneuron connections between ventral horns (Bannatyne et al., 2003; Jankowska, 2008). Thus, the recording of electrophysiological signals in the ventral horns would serve as gold-standard measurements to validate and examine to what extent these rsfMRI findings reflect underlying neural activity; similar to what was performed between dorsal horns in Chapter 2. In addition, the observation of hemi-cord dorsal-ventral connectivity has been less consistent. Eippert et al. reported that the ROI selection process appears to be a driving factor for dorsal-ventral connectivity observed, which is suggestive of time course mixing due to the proximity of dorsal and ventral horns in humans. Given the involvement of sensorimotor systems in mediating reflexes in the spinal cord, it remains unclear why dorsal-ventral connections have not been reliably detectable. One possible explanation is that the spinal cord does not cycle through its full network of connections at rest (Eippert et al., 2017). Nevertheless, to fully examine the functional relationship between dorsal and ventral horns, sampling of both regions simultaneously in electrophysiology experiments will permit more comprehensive comparisons with fMRI and would also require further customizations in electrode configurations.

#### **5.2.4. Application of machine learning methods to spinal rsfMRI data**

Recently, there has been a growing interest in applying machine learning, in particular deep learning, methods to functional neuroimaging for advancing our understanding of the brain's functional architecture. Conventional fMRI statistical analyses typically involve the GLM which is inevitably limited by the model itself, while machine learning methods provide greater flexibility with a model-free data-driven approach. A promising technique that has been commonly exploited for investigating fMRI data is multi-voxel pattern analysis (Mahmoudi et al., 2012). The algorithm involves the search and classification of common spatial patterns of activity in fMRI data under different experimental conditions. Similarly, unsupervised clustering methods such as k-means clustering and self-organizing maps have also been applied for parcellations based on rsfMRI connectivity patterns in cortical gray matter regions (Liao et al., 2008; Venkataraman et al., 2009) and even in white matter of the brain (Peer et al., 2017). More recently, there has also been a growing emergence of deep learning methods that use fMRI data for identifying different pathological conditions such as Autism Spectrum Disorder (Vigneshwaran et al., 2015), Schizophrenia (Patel et al., 2016) and Mild Cognitive Impairment (Meszlényi et al., 2017).

Given recent advances of machine learning methods, it may be valuable to apply them to spinal rsfMRI data to further understand how the spinal cord is functionally organized beyond the four horns commonly identified in ROI-based analyses. Indeed, of all spinal rsfMRI studies to date, there have only been a limited number that has used a model-free data-driven approach – independent component analysis (Kong et al., 2014; Wei et al., 2010). Interestingly, Kong et al. found very similar results to ours and others that have used a ROI-based approach, in which the spinal cord was found to be organized in pairs of dorsal resting-state networks and bilateral ventral resting-state networks. In general, seed-based approaches allow regions to be selected based on hypothesis derived from stimulus-driven data as well as previous fMRI studies in humans and animals. On the other hand, merits of machine learning methods come into play when there is less confidence in the hypotheses used to define seed regions. In particular, when attempting to tease out unknown spinal local circuitries at a high resolution beyond the four horns, pre-defining seeds can be a challenge and more subjective. Nevertheless, the application of recent machine learning methods can provide insight from another perspective of how the spinal cord is functionally organized.

### 5.3. References

- Bamford, J.A., Mushahwar, V.K., 2011. Intraspinal microstimulation for the recovery of function following spinal cord injury. *Prog. Brain Res.* 194, 227–239. doi:10.1016/B978-0-444-53815-4.00004-2
- Bannatyne, B.A., 2006. Differential Projections of Excitatory and Inhibitory Dorsal Horn Interneurons Relaying Information from Group II Muscle Afferents in the Cat Spinal Cord. *J. Neurosci.* 26, 2871–2880. doi:10.1523/JNEUROSCI.5172-05.2006
- Bannatyne, B.A., Edgley, S.A., Hammar, I., Jankowska, E., Maxwell, D.J., 2003. Networks of inhibitory and excitatory commissural interneurons mediating crossed reticulospinal actions. *Eur. J. Neurosci.* 18, 2273–2284. doi:10.1046/j.1460-9568.2003.02973.x
- Barry, R.L., Smith, S.A., Dula, A.N., Gore, J.C., 2014. Resting state functional connectivity in the human spinal cord. *Elife* 2014, 1–15. doi:10.7554/eLife.02812
- Barry, R.L., Vannesjo, S.J., By, S., Gore, J.C., Smith, S.A., 2018. Spinal cord MRI at 7T. *Neuroimage* 168, 437–451. doi:10.1016/j.neuroimage.2017.07.003
- Chen, L.M., Mishra, A., Yang, P.-F., Wang, F., Gore, J.C., 2015. Injury alters intrinsic functional connectivity within the primate spinal cord. *Proc. Natl. Acad. Sci. U. S. A.* 112, 5991–6. doi:10.1073/pnas.1424106112
- Culberson, J.L., Haines, D.E., Kimmel, D.L., Brown, P.B., 1979. Contralateral projection of primary afferent fibers to mammalian spinal cord. *Exp. Neurol.* 64, 83–97. doi:10.1016/0014-4886(79)90007-4
- Eippert, F., Kong, Y., Winkler, A.M., Andersson, J.L., Finsterbusch, J., Büchel, C., Brooks, J.C.W., Tracey, I., 2017. Investigating resting-state functional connectivity in the cervical spinal cord at 3 T. *Neuroimage* 147, 589–601. doi:10.1016/j.neuroimage.2016.12.072
- Fitzgerald, M., 1983. Influences of contralateral nerve and skin stimulation on neurones in the substantia gelatinosa of the rat spinal cord. *Neurosci. Lett.* 36, 139–143. doi:10.1016/0304-3940(83)90255-0
- Fitzgerald, M., 1982. The contralateral input to the dorsal horn of the spinal cord in the decerebrate spinal rat. *Brain Res.* 236, 275–287. doi:10.1016/0006-8993(82)90714-4
- Jankowska, E., 2008. Spinal interneuronal networks in the cat: Elementary components. *Brain Res. Rev.* doi:10.1016/j.brainresrev.2007.06.022
- Kong, Y., Eippert, F., Beckmann, C.F., Andersson, J., Finsterbusch, J., Büchel, C., Tracey, I., Brooks, J.C., 2014. Intrinsically organized resting state networks in the human spinal cord. *Proc Natl Acad Sci U S A* 111, 18067–18072. doi:10.1073/pnas.1414293111
- Lea, P.M., Faden, A.I., 2003. Modulation of metabotropic glutamate receptors as potential treatment for acute and chronic neurodegenerative disorders. *Drug News Perspect.* 16, 513–522.

doi:10.1358/dnp.2003.16.8.829350

- Liao, W., Chen, H., Yang, Q., Lei, X., 2008. Analysis of fMRI data using improved self-organizing mapping and spatio-temporal metric hierarchical clustering. *IEEE Trans. Med. Imaging* 27, 1472–1483. doi:10.1109/TMI.2008.923987
- Light, A.R., Perl, E.R., 1979. Reexamination of the dorsal root projection to the spinal dorsal horn including observations on the differential termination of coarse and fine fibers. *J. Comp. Neurol.* 186, 117–131. doi:10.1002/cne.901860202
- Mahmoudi, A., Takerkart, S., Regragui, F., Boussaoud, D., Brovelli, A., 2012. Multivoxel pattern analysis for fMRI data: A review. *Comput. Math. Methods Med.* doi:10.1155/2012/961257
- McAdoo, D.J., Xu, G.Y., Robak, G., Hughes, M.G., 1999. Changes in amino acid concentrations over time and space around an impact injury and their diffusion through the rat spinal cord. *Exp. Neurol.* 159, 538–544. doi:10.1006/exnr.1999.7166
- Meszlyenyi, R.J., Buza, K., Vidnyánszky, Z., 2017. Resting state fMRI functional connectivity-based classification using a convolutional neural network architecture. *Front. Neuroinform.* 11. doi:10.3389/fninf.2017.00061
- Okon, E.B., Streijger, F., Lee, J.H.T., Anderson, L.M., Russell, A.K., Kwon, B.K., 2013. Intraparenchymal Microdialysis after Acute Spinal Cord Injury Reveals Differential Metabolic Responses to Contusive versus Compressive Mechanisms of Injury. *J. Neurotrauma* 30, 1564–1576. doi:10.1089/neu.2013.2956
- Patel, P., Aggarwal, P., Gupta, A., 2016. Classification of schizophrenia versus normal subjects using deep learning, in: *ACM International Conference Proceeding Series*. doi:10.1145/3009977.3010050
- Peer, M., Nitzan, M., Bick, A.S., Levin, N., Arzy, S., 2017. Evidence for Functional Networks within the Human Brain's White Matter. *J. Neurosci.* 37, 6394–6407. doi:10.1523/JNEUROSCI.3872-16.2017
- Petkó, M., Antal, M., 2000. Propriospinal afferent and efferent connections of the lateral and medial areas of the dorsal horn (Laminae I-IV) in the rat lumbar spinal cord. *J. Comp. Neurol.* 422, 312–325. doi:10.1002/(SICI)1096-9861(20000626)422:2<312::AID-CNE11>3.0.CO;2-A
- Qi, H.-X., Kaas, J.H., Reed, J.L., 2014. The reactivation of somatosensory cortex and behavioral recovery after sensory loss in mature primates. *Front. Syst. Neurosci.* 8. doi:10.3389/fnsys.2014.00084
- Streijger, F., So, K., Manouchehri, N., Tigchelaar, S., Lee, J.H.T., Okon, E.B., Shortt, K., Kim, S.-E., McInnes, K., Crompton, P., Kwon, B.K., 2017. Changes in Pressure, Hemodynamics, and Metabolism within the Spinal Cord during the First 7 Days after Injury Using a Porcine Model. *J. Neurotrauma* neu.2017.5034. doi:10.1089/neu.2017.5034
- Thuret, S., Moon, L.D.F., Gage, F.H., 2006. Therapeutic interventions after spinal cord injury. *Nat. Rev. Neurosci.* 7, 628–43. doi:10.1038/nrn1955

- Venkataraman, A., Van Dijk, K.R.A., Buckner, R.L., Golland, P., 2009. Exploring functional connectivity in fMRI via clustering, in: 2009 IEEE International Conference on Acoustics, Speech and Signal Processing. pp. 441–444. doi:10.1038/nbt.3121.ChIP-nexus
- Vigneshwaran, S., Mahanand, B.S., Suresh, S., Sundararajan, N., 2015. Using regional homogeneity from functional MRI for diagnosis of ASD among males, in: 2015 International Joint Conference on Neural Networks (IJCNN). pp. 1–8. doi:10.1109/IJCNN.2015.7280562
- Wang, F., Qi, H.-X., Zu, Z., Mishra, A., Tang, C., Gore, J.C., Chen, L.M., 2014. Multiparametric MRI reveals dynamic changes in molecular signatures of injured spinal cord in monkeys. *Magn. Reson. Med.* 0, 1–13. doi:10.1002/mrm.25488
- Wang, F., Zu, Z., Wu, R., Wu, T.-L., Gore, J.C., Chen, L.M., 2018. MRI evaluation of regional and longitudinal changes in Z-spectra of injured spinal cord of monkeys. *Magn. Reson. Med.* 79, 1070–1082. doi:10.1002/mrm.26756
- Wei, P., Li, J., Gao, F., Ye, D., Zhong, Q., Liu, S., 2010. Resting state networks in human cervical spinal cord observed with fMRI. *Eur. J. Appl. Physiol.* 108, 265–271. doi:10.1007/s00421-009-1205-4
- Wu, T.-L., Wang, F., Mishra, A., Wilson, G.H., Byun, N., Chen, L.M., Gore, J.C., 2017. Resting-state functional connectivity in the rat cervical spinal cord at 9.4 T. *Magn. Reson. Med.* doi:10.1002/mrm.26905
- Xu, W., Chi, L., Xu, R., Ke, Y., Luo, C., Cai, J., Qiu, M., Gozal, D., Liu, R., 2005. Increased production of reactive oxygen species contributes to motor neuron death in a compression mouse model of spinal cord injury. *Spinal Cord* 43, 204–213. doi:10.1038/sj.sc.3101674
- Zhou, J., Tryggestad, E., Wen, Z., Lal, B., Zhou, T., Grossman, R., Wang, S., Yan, K., Fu, D.X., Ford, E., Tyler, B., Blakeley, J., Laterra, J., Van Zijl, P.C.M., 2011. Differentiation between glioma and radiation necrosis using molecular magnetic resonance imaging of endogenous proteins and peptides. *Nat. Med.* 17, 130–134. doi:10.1038/nm.2268